

Development of solid electrolyte materials for solid-state lithium batteries

Zhijun Wu

Graduate School of Science and Technology

Hirosaki University

2020

ABSTRACT

Solid-state lithium batteries (SSLBs) with solid electrolytes (SEs) have attracted great attention for the replacement of traditional lithium batteries with liquid electrolytes due to their advantages such as high safety, excellent electrochemical cycling property and long-term stability. To date, the strategies to improve electrochemical performance especially ionic conductivity and stability of SEs have been widely studied. However, nowadays, SSLBs are still not commercialized and used in our daily life. The main purpose of this research is to develop high-performance SEs for SSLBs. In this study, the effects of various doping materials for solid sulfide electrolytes and solid polymer electrolytes on the performances were investigated, which focused on ionic conductivity, ion transference number, electrochemically stable, lithium stability, thermal stability, and charge-discharge stability. It is found that when loading material type and material support were adjusted, the electrochemical performances of SEs were changed significantly. The mechanisms and structures of SEs were proposed and discussed. It is expected to provide a guidance for the development of novel SEs with higher ionic conductivity and environmental stability for SSLBs. The main conclusions in this dissertation are summarized as follows:

Firstly, $\text{Li}_2\text{S}-\text{P}_2\text{S}_5$ (LPS) based glass-ceramic electrolytes doped with SeS_2 were prepared by a facile high-energy ball milling combined annealing way. The structures, ionic conductivities and electrochemical stabilities of the $70\text{Li}_2\text{S} \cdot (30-x)\text{P}_2\text{S}_5 \cdot x\text{SeS}_2$ ($x=0, 0.3, 0.5, 1, 3, 5$) glass-ceramic electrolytes were investigated. By combining X-ray powder diffraction (XRD) analysis-refinement and first-principle calculations, it is confirmed that a little amount of SeS_2 ($x \leq 1$) was successfully doped into the framework of LPS composite, and as such, the ionic conductivity was greatly enhanced by the substitution of a part of P_2S_5 with SeS_2 . In particular, the $70\text{Li}_2\text{S} \cdot 29\text{P}_2\text{S}_5 \cdot 1\text{SeS}_2$ glass-ceramic exhibited the highest conductivity of $5.28 \times 10^{-3} \text{ S} \cdot \text{cm}^{-1}$ at 20°C with a low activation energy of $24.7 \text{ kJ} \cdot \text{mol}^{-1}$, and higher

electrochemical stability than the original $70\text{Li}_2\text{S}\cdot 30\text{P}_2\text{S}_5$ glass–ceramic. Furthermore, SSLBs assembled based on $70\text{Li}_2\text{S}\cdot 29\text{P}_2\text{S}_5\cdot 1\text{SeS}_2$ electrolyte and sulfur-reduced graphene oxide (S-rGO) composite electrode showed excellent rate capability and cycling stability at low temperatures. Furthermore, electrochemical impedance spectroscopy (EIS) analyses and the cross-section observation by scanning electron microscope (SEM) of SSLBs revealed that addition of SeS_2 into the $\text{Li}_2\text{S}\text{-P}_2\text{S}_5$ electrolyte substrate decreased the interfacial resistance between the electrodes and solid electrolyte and reduced the production of lithium dendrites. These results indicated that $70\text{Li}_2\text{S}\cdot 29\text{P}_2\text{S}_5\cdot 1\text{SeS}_2$ electrolyte can be served as an effective solid electrolyte for the construction of high performance SSLBs.

Air and electrochemical stability, high interfacial resistance, and complex preparation process are significant problems which should be solved in sulfide-type solid electrolyte development. In air atmosphere, these sulfide solid electrolytes were easily decomposed in the reaction with the atmospheric water/hydrogen, resulting in the generation of H_2S . Recently, many researchers concentrated to develop polymer electrolytes with relatively reliable stability, low interfacial resistance, high flexibility, stretchable property, and low fabricating cost. In this study, a novel polyethylene oxide (PEO)-Lithium bis(trifluoromethylsulphonyl)imide (LiTFSI)-nanocomposite-based polymer electrolyte was also prepared by using nickel phosphate (VSB-5) nanorods as the filler. The ionic conductivity of the obtained PEO-LiTFSI-3% VSB-5 solid polymer electrolyte was found to be as high as $4.83\times 10^{-5} \text{ S}\cdot\text{cm}^{-1}$ at $30\text{ }^\circ\text{C}$ and electrochemically stable up to about 4.13 V versus Li/Li^+ . The enhanced ionic conductivity was attributed to the reduced crystallinity of the PEO and the interaction between VSB-5 and PEO-LiTFSI. In addition, the solid polymer electrolyte exhibited improved compatibility to the lithium metal anode with excellent suppression of lithium dendrites. The assembled $\text{LiFePO}_4/\text{Li}$ battery with the PEO-LiTFSI-3% VSB-5 solid polymer electrolyte showed better rate performance and higher cyclic stability than the PEO-LiTFSI electrolyte. It is

demonstrated that this new solid polymer hybrid should be a promising electrolyte applied in SSLBs with lithium metal electrode.

To elevate the conductivity of SPE, restrain lithium dendrite growth and increase the thermal stability, a flame-retardant filler, $\text{Zn}_2(\text{OH})\text{BO}_3$ with rod-like structure and relatively high dehydration temperature (about 415 °C), was also used for the improvement of the performance of SPE. In this work, a novel solid polymer composite electrolyte based on poly(ethylene oxide) (PEO) with rod-like $\text{Zn}_2(\text{OH})\text{BO}_3$ particles was prepared by a grinding process followed with a heating treatment process and a cold pressing process. The effect of the incorporation amount of rod-like $\text{Zn}_2(\text{OH})\text{BO}_3$ particles on the ionic conductivity was investigated systemically. It is found that 10 mol% of rod-like $\text{Zn}_2(\text{OH})\text{BO}_3$ particles addition resulted in the highest ionic conductivity of 2.78×10^{-5} at 30 °C and the improved ionic conductivity was considered to be caused by the reducing of PEO crystallinity and the increasing of Li ion migrating pathway on the interface between the $\text{Zn}_2(\text{OH})\text{BO}_3$ and PEO. In addition, the optimum composite electrolyte exhibited a high electrochemical stability window of 4.51 V (vs. Li/Li^+), good lithium stability and excellent thermal stability.

ACKNOWLEDGMENTS

First of all, I would like to express my sincere gratitude and appreciation to my supervisor, Professor Dr. Guoqing Guan for his great advices and guidelines for my research and the life in Japan.

I would like to thank Professor Dr. Abuliti Abudula, Graduate School of Science and Technology, Hirosaki University, for his advices and supports of my study.

I would like to thank Associate Professor Dr. Akihiro Yoshida, Laboratory of Energy Conversion Engineering, Institute of Regional Innovation (IRI), Hirosaki University, for his kind suggestions and helpful discussion.

I would like to thank Assistant Professor Dr. Tao Yu, Graduate School of Science and Technology, Hirosaki University, for his supports for my experiment.

I would like to thank Professor Dr. Xiaogang Hao and Professor Dr. Zhongde Wang, Department of Chemical Engineering, Tianyuan University of Technology, China, for their helps in characteristic and experiment.

I would like to thank all members in our group for their friendship and helpfulness.

I would like to thank my dear family and my girlfriend Jing Wang for all their support. Whenever I need help, they come over first to support me and encourage me. Thank my girlfriend, who always takes good care of me and helps me in daily life and my research. I wish they could always be happy and healthy.

Finally, I would like to acknowledge the Jiku Chemical Co. Ltd. and scholarship from the China Scholarship Council for full supports along my Ph.D. study.

Thank you all

Zhijun Wu

TABLE OF CONTENTS

ABSTRACT.....	i
ACKNOWLEDGMENTS	iv
TABLE OF CONTENTS.....	v
LIST OF TABLES.....	ix
LIST OF FIGURES	x
ABBREVIATIONS	xiv
Chapter 1 Introduction	1
1.1 General Introduction	1
1.2 The state-of-the-arts of various solid electrolytes.....	3
1.2.1 Solid oxide electrolytes.....	3
1.2.1.1 NASICON-type.....	3
1.2.1.2 Perovskite-type	5
1.2.1.3 Garnet-type	7
1.2.1.4 Amorphous/glass-type	8
1.2.2 Solid sulfide electrolytes.....	10
1.2.2.1 Li ₂ S-SiS ₂ based electrolytes.....	10
1.2.2.2 Li ₂ S-P ₂ S ₅ based electrolytes	11
1.2.3 Solid polymer electrolytes (SPEs)	14
1.2.3.1 PEO and PEO like-based SPEs.....	15
1.2.3.2 Non-polyether-based SPEs	16
1.2.3.3 Single lithium-ion conducting-based SPEs.....	18
1.2.4 Organic-inorganic hybrid electrolytes	19
1.3 Objective of this research.....	22
1.4 Scope of dissertation	23

References.....	25
Chapter 2 Experimental	54
2.1 Chemical reagents.....	54
2.2 Performance evaluation	56
2.3 Characterization	56
2.3.1 X-Ray Diffraction (XRD)	56
2.3.2 Scanning Electron Microscopy (SEM) and Energy Dispersive X-Ray Spectrometer (EDS)	57
2.3.3 Transmission Electron Microscopy (TEM)	57
2.3.4 Differential Scanning Calorimetry (DSC)	57
2.3.5 Thermogravimetric (TG)	57
2.3.6 Fourier transform infrared spectrum (FT-IR)	57
2.3.7 Raman	57
2.3.8 Electrochemical Measurement.....	57
2.3.9 Charge and Discharge Measurement	58
Chapter 3 Novel SeS ₂ doped Li ₂ S–P ₂ S ₅ solid electrolyte with high ionic conductivity for all- solid-state lithium sulfur batteries.....	59
3.1 Introduction.....	59
3.2 Experimental	61
3.2.1 Solid electrolyte synthesis.....	61
3.2.2 Cathode materials synthesis.....	61
3.2.3 Characterizations.....	62
3.2.4 Electrochemical performance measurements	62
3.2.5 All-solid-state Li-S batteries assembling and test.....	63
3.2.6 Computational details	64

3.3 Results and discussion	65
3.4 Conclusions.....	79
References.....	80
Chapter 4 Nickel phosphate nanorod-enhanced polyethylene oxide-based composite polymer electrolytes for solid-state lithium batteries	
4.1 Introduction.....	87
4.2 Experimental Section	89
4.2.1 Synthesis of VSB-5 nanorods	89
4.2.2 Fabrications of the cathode and solid polymer electrolyte	89
4.2.3 Characterizations.....	90
4.2.4 Electrochemical evaluation	91
4.3 Results and discussion	92
4.4 Conclusions.....	105
References.....	106
Chapter 5 Simultaneously enhancing the thermal stability and electrochemical performance of solid polymer electrolytes by incorporating rod-like $\text{Zn}_2(\text{OH})\text{BO}_3$ particles	
5.1 Introduction.....	115
5.2 Experimental Section	117
5.2.1 Synthesis of rod-like $\text{Zn}_2(\text{OH})\text{BO}_3$ paticles.....	117
5.2.2 Synthesis of solid polymer composite electrolytes	117
5.2.3 Characterizations.....	118
5.2.4 Electrochemical evaluation of solid polymer composite electrolyte	118
5.2.5 Electrochemical evaluation of solid-state battery	119
5.3 Results and discussion	120
5.4 Conclusions.....	133

References.....	134
Chapter 6 Conclusions and Prospect.....	143
6.1 Conclusions.....	143
6.2 Prospect.....	145
References.....	149
List of publications and presentations.....	150

LIST OF TABLES

Table 2.1 Chemical reagents used in this study.	54
Table 3.1 Refined unit cell dimensions and cell angles in Se doping $70\text{Li}_2\text{S} \cdot 30\text{P}_2\text{S}_5$	69
Table 5.1 Melting temperature T_m , melting enthalpy ΔH , and degree of crystallinity χ_c of PEO, PEO-LiTFSI and PEO-LiTFSI-10% $\text{Zn}_2(\text{OH})\text{BO}_3$	123

LIST OF FIGURES

Figure 1.1 3D NASICON-type structure of $\text{LiM}_2(\text{PO}_4)_3$	4
Figure 1.2 Structure schematic of perovskite-type electrolytes (ABO_3).	5
Figure 1.3 The crystal structure of 3D garnet-type $\text{Li}_3\text{B}_3\text{C}_2\text{O}_{12}$	8
Figure 1.4 Schematic 2D representation of tetrahedrally coordinated $\text{Li}_2\text{O}-\text{SiO}_2$ glass.	9
Figure 1.5 Crystal structure of $\text{Li}_{10}\text{GeP}_2\text{S}_{12}$ [108].	14
Figure 1.6 Membrane photos of PEO-LLZO (A), PEO-LAGP (B) and PEO-LGPS (C).....	21
Figure 3.1 Optical image of (A) the disassembling of battery equipment, (B) Li anode, (C) rGO-S-SE cathode, (D) the schematic diagram and (E) the side view of rGO-S/SE/Li battery, and (F) the whole of battery equipment.	64
Figure 3.2 Ion conductivity of $70\text{Li}_2\text{S}\cdot 30\text{-xP}_2\text{S}_5\cdot \text{xSeS}_2$ ($x=0, 0.3, 0.5, 1, 3, 5$) solid electrolyte systems.....	65
Figure 3.3 (A) Nyquist plots of $70\text{Li}_2\text{S}\cdot 30\text{P}_2\text{S}_5$ and $70\text{Li}_2\text{S}\cdot 29\text{P}_2\text{S}_5\cdot 1\text{SeS}_2$ glass-ceramics at 20°C , (B) Temperature dependence of conductivity for $70\text{Li}_2\text{S}\cdot 30\text{P}_2\text{S}_5$ and $70\text{Li}_2\text{S}\cdot 29\text{P}_2\text{S}_5\cdot 1\text{SeS}_2$ glass-ceramics from 30°C to 100°C	67
Figure 3.4 XRD patterns of the $70\text{Li}_2\text{S}\cdot 30\text{-xP}_2\text{S}_5\cdot \text{xSeS}_2$ ($x=0, 0.3, 0.5, 1, 3, 5$) glass-ceramics (A) in the 2θ range from 10° to 60° and (B) Magnified 2θ range from 15° to 30° and (C) 32.0° to 32.4°	68
Figure 3.5 (Color online.) Ball and stick diagrams of supercells of calculated optimum structures of (A): $70\text{Li}_2\text{S}\cdot 30\text{P}_2\text{S}_5$, (B): 1 Se doping $70\text{Li}_2\text{S}\cdot 30\text{P}_2\text{S}_5$, (C): 2 Se doping $70\text{Li}_2\text{S}\cdot 30\text{P}_2\text{S}_5$, (D): 3 Se doping $70\text{Li}_2\text{S}\cdot 30\text{P}_2\text{S}_5$, (E): 4 Se doping $70\text{Li}_2\text{S}\cdot 30\text{P}_2\text{S}_5$, and (F): 5 Se doping $70\text{Li}_2\text{S}\cdot 30\text{P}_2\text{S}_5$ electrolytes. Li, P, S, and Se are indicated with wathet blue, purple, yellow, and orange balls, respectively.	69
Figure 3.6 DSC curves of $70\text{Li}_2\text{S}\cdot 30\text{-xP}_2\text{S}_5\cdot \text{xSeS}_2$ ($x=0, 0.3, 0.5, 1, 3, 5$) glasses prepared by ball milling.	70

Figure 3.7 Raman spectra of $70\text{Li}_2\text{S}\cdot 30\text{-xP}_2\text{S}_5\cdot \text{xSeS}_2$ ($\text{x}=0, 0.3, 0.5, 1, 3, 5$) electrolytes.	71
Figure 3.8 Chronoamperometry test of $70\text{Li}_2\text{S}\cdot 30\text{P}_2\text{S}_5$ and $70\text{Li}_2\text{S}\cdot 29\text{P}_2\text{S}_5\cdot 1\text{SeS}_2$ solid electrolyte-based Li/solid electrolyte/Li symmetric batteries cycled at a constant voltage of 0.1 V at 30 °C.....	72
Figure 3.9 CV curves of (A) $70\text{Li}_2\text{S}\cdot 30\text{P}_2\text{S}_5$ and (B) $70\text{Li}_2\text{S}\cdot 29\text{P}_2\text{S}_5\cdot 1\text{SeS}_2$ glass-ceramics based Li/solid electrolyte/stainless steel batteries in the potential range from -0.5 V to 5 V (vs. Li/Li^+) at a scanning rate of $1\text{ mV}\cdot\text{s}^{-1}$ at 30 °C.	73
Figure 3.10 SEM images of the as-prepared (A) pure rGO and (B) S-rGO, EDS image of (C) S-rGO.....	74
Figure 3.11 CV measurements of ASSLSBs based on $70\text{Li}_2\text{S}\cdot 30\text{P}_2\text{S}_5$ and $70\text{Li}_2\text{S}\cdot 29\text{P}_2\text{S}_5\cdot 1\text{SeS}_2$ electrolytes respectively at 30 °C.	75
Figure 3.12 (A) The initial charge-discharge curves and (B) cycle performances of ASSLSBs based on $70\text{Li}_2\text{S}\cdot 30\text{P}_2\text{S}_5$ and $70\text{Li}_2\text{S}\cdot 29\text{P}_2\text{S}_5\cdot 1\text{SeS}_2$ electrolytes at a rate of $0.1\text{ mA}\cdot\text{cm}^{-2}$ at 30 °C.....	76
Figure 3.13 Nyquist plots of $\text{rGO}/70\text{Li}_2\text{S}\cdot 30\text{P}_2\text{S}_5/\text{Li}$, and $\text{rGO-S}/70\text{Li}_2\text{S}\cdot 29\text{P}_2\text{S}_5\cdot 1\text{SeS}_2/\text{Li}$ ASSLSBs at 30 °C. Measurements were conducted (A) before and (B) after 20 cycles at $0.1\text{ mA}\cdot\text{cm}^{-2}$	78
Figure 3.14 SEM images of the interface between the (A) $70\text{Li}_2\text{S}\cdot 30\text{P}_2\text{S}_5$; (B) $70\text{Li}_2\text{S}\cdot 29\text{P}_2\text{S}_5\cdot 1\text{SeS}_2$ and Li in $\text{rGO-S}/\text{solid electrolyte}/\text{Li}$ batteries at $0.1\text{ mA}\cdot\text{cm}^{-2}$ for 100 charge-discharge cycles.....	79
Figure 4.1 SEM images of VSB-5 (A) pH=7 (MR= 1:10:5) (B) pH=9 (MR= 1:10:5) (C) pH=7 (MR= 1:10:15) (D) pH=9 (MR= 1:10:15), MR: molar ratio of $\text{NiCl}_2\cdot 6\text{H}_2\text{O}:\text{HMT}:\text{NaH}_2\text{PO}_4$	93
Figure 4.2 EISs of $\text{PEO-LiTFSI-x}\%$ VSB-5 ($\text{x} = 0, 1, 3, 5$, and 10) at 30 °C. d: Thickness...	95
Figure 4.3 XRD (A) of the $\text{PEO-LiTFSI-x}\%$ VSB-5 ($\text{x} = 0, 1, 3, 5$, and 10) and high-resolution	

XRD (B) of VSB-5 and PEO-LiTFSI-3% VSB-5.	96
Figure 4.4 Schematic (A) of Li^+ migration in VSB-5 enhanced composite SPEs, FTIR (B) of the PEO-LiTFSI-x% VSB-5 ($x = 0, 1, 3, 5$, and 10) and the magnification (C) of FTIR in the wavenumber range of $1500\text{-}900\text{ cm}^{-1}$	98
Figure 4.5 DSC (A) of the PEO, PEO-LiTFSI and PEO-LiTFSI-3% VSB-5 and the EIS and chronoamperometry curves (B) of a Li/SPE/Li cell under a potential step of 10 mV	98
Figure 4.6 LSVs (A) of the PEO-LiTFSI and PEO-LiTFSI-3% VSB-5 SPEs under a scan rate of $1\text{ mV}\cdot\text{s}^{-1}$ and voltage-time profiles (B) of Li metal plating and stripping in Li/SPE/Li cells at 0.1 mA	100
Figure 4.7 TGA curves of the PEO-LiTFSI and PEO-LiTFSI-3% VSB-5 electrolytes.	101
Figure 4.8 SEM (A) and EDS mapping (B) of the PEO-LiTFSI-3% VSB-5 electrolyte.	102
Figure 4.9 SEM image of the PEO-VSB-5.	102
Figure 4.10 TEM images of PEO (A-B) and PEO-VSB-5 (C).	102
Figure 4.11 (A) Cycling performances of $\text{LiFePO}_4/\text{PEO-LiTFSI/Li}$ and $\text{LiFePO}_4/\text{PEO-LiTFSI-3\% VSB-5/Li}$ batteries at 0.2 C and $60\text{ }^\circ\text{C}$. (C) Rate performances of $\text{LiFePO}_4/\text{PEO-LiTFSI/Li}$ and $\text{LiFePO}_4/\text{PEO-LiTFSI-3\% VSB-5/Li}$ batteries at $60\text{ }^\circ\text{C}$	104
Figure 4.12 Cross-section and interface images of $\text{LiFePO}_4/\text{PEO-LiTFSI/Li}$ battery (A-B) and $\text{LiFePO}_4/\text{PEO-LiTFSI-3\% VSB-5/Li}$ battery (C-D) after the rate cycling test.	105
Figure 5.1 (A-B) The SEM images of the as-prepared $\text{Zn}_2(\text{OH})\text{BO}_3$ particles with different magnifications and (C) the crystal structures of $\text{Zn}_2(\text{OH})\text{BO}_3$	120
Figure 5.2 EISs (A) of $\text{PEO-LiTFSI-x\% Zn}_2(\text{OH})\text{BO}_3$ ($x = 0, 5, 10, 15$, and 20) at $30\text{ }^\circ\text{C}$, DSCs thermograms (B) and XRD patterns (C) of PEO, PEO-LiTFSI and PEO-LiTFSI- $10\%\text{ Zn}_2(\text{OH})\text{BO}_3$, d: Thickness.	122

Figure 5.3 (A) FT-IR spectra of PEO, $\text{Zn}_2(\text{OH})\text{BO}_3$, LiTFSI and PEO-LiTFSI- $x\%\text{Zn}_2(\text{OH})\text{BO}_3$ in the range of $400\text{-}4000\text{ cm}^{-1}$. Schematic showing the PEO-LiTFSI (B) and the increased conformational mobility of PEO-LiTFSI- $\text{Zn}_2(\text{OH})\text{BO}_3$ (C).....	125
Figure 5.4 (A) LSV curves of PEO-LiTFSI and PEO-LiTFSI- $10\%\text{Zn}_2(\text{OH})\text{BO}_3$ SPEs at a scanning rate of $1\text{ mV}\cdot\text{s}^{-1}$ and $60\text{ }^\circ\text{C}$, (B) TGA-DTG curves of PEO-LiTFSI and PEO-LiTFSI- $10\%\text{Zn}_2(\text{OH})\text{BO}_3$ SPEs, lithium deposition/stripping of Li/PEO-LiTFSI/Li (C) and Li/PEO-LiTFSI- $10\%\text{Zn}_2(\text{OH})\text{BO}_3$ /Li (D) symmetrical batteries at a current of 0.1 mA at $60\text{ }^\circ\text{C}$	127
Figure 5.5 Time-dependent response of DC polarization potential obtained on a Li/SPE/Li battery cell at $40\text{ }^\circ\text{C}$. Inset: impedance spectra before and after the polarization.	128
Figure 5.6 SEM image and EDS mappings of the PEO-LiTFSI- $10\%\text{Zn}_2(\text{OH})\text{BO}_3$	129
Figure 5.7 SEM images of the LiFePO_4 /PEO-LiTFSI- $10\%\text{Zn}_2(\text{OH})\text{BO}_3$ /Li battery. (A) Cross sectional images. (B-D) Element mapping of the LiFePO_4 /PEO-LiTFSI- $10\%\text{Zn}_2(\text{OH})\text{BO}_3$ /Li battery.	129
Figure 5.8 (A) EIS of the LiFePO_4 /PEO-LiTFSI- $10\%\text{Zn}_2(\text{OH})\text{BO}_3$ /Li and LiFePO_4 /PEO-LiTFSI/Li batteries at $60\text{ }^\circ\text{C}$; (B) Cycling performances of the LiFePO_4 /PEO-LiTFSI- $10\%\text{Zn}_2(\text{OH})\text{BO}_3$ /Li and LiFePO_4 /PEO-LiTFSI/Li batteries at 0.2 C ...	131
Figure 5.9 SEM images of the cross-sectional views of LiFePO_4 /PEO-LiTFSI/Li (A) and LiFePO_4 /PEO-LiTFSI- $10\%\text{Zn}_2(\text{OH})\text{BO}_3$ /Li (C) batteries, and the interface views of LiFePO_4 /PEO-LiTFSI/Li (B) and LiFePO_4 /PEO-LiTFSI- $10\%\text{Zn}_2(\text{OH})\text{BO}_3$ /Li (D) after the cycling performance tests.....	133

ABBREVIATIONS

Li, Lithium; SSLBs, Solid-state lithium batteries; SPEs, Solid polymer electrolytes; NASICON, Natrium superionic conductor; thio-LISICON, thio-Li super ionic conductor; 3D, Three dimensional; RT, Room temperature; LGPS, $\text{Li}_{10}\text{GeP}_2\text{S}_{12}$; PEO, Polyethylene oxide; LZP, $\text{LiZr}_2(\text{PO}_4)_3$; LYZP, $\text{Li}_{1+x}\text{Y}_x\text{Zr}_{2-x}(\text{PO}_4)_3$; LTP, $\text{LiTi}_2(\text{PO}_4)_3$; LATP, $\text{Li}_{1.3}\text{Al}_{0.3}\text{Ti}_{1.7}(\text{PO}_4)_3$; LAGP, $\text{Li}_{1+x}\text{Al}_x\text{Ge}_{2-x}(\text{PO}_4)_3$; S-MWCNT, sulfur-coated carbon nanotubes; LLTO, $\text{Li}_{3x}\text{La}_{2/3-x}\text{TiO}_3$; LSTZ, $\text{Li}_{3/8}\text{Sr}_{7/16}\text{Ta}_{3/4}\text{Zr}_{1/4}\text{O}_3$; LSHT, $\text{Li}_{3/8}\text{Sr}_{7/16}\text{Ta}_{3/4}\text{Hf}_{1/4}\text{O}_3$; LSNZ, $\text{Li}_{3/8}\text{Sr}_{7/16}\text{Nb}_{3/4}\text{Zr}_{1/4}\text{O}_3$; LLZO, $\text{Li}_7\text{La}_3\text{Zr}_2\text{O}_{12}$; LGLZO, $\text{Li}_{6.25}\text{Ga}_{0.25}\text{La}_3\text{Zr}_2\text{O}_{12}$; LiPON, $\text{Li}_x\text{PO}_y\text{N}_z$; ORNL, Oak Ridge National Laboratory; PLD, Pulsed laser deposition; PEO-PAN, Polyacrylonitrile-polyethylene oxide; MOFs, Metal organic frameworks; PEOMA, Poly(ethylene oxide) methyl ether methacrylate; MBL, α -methylene- γ -butyrolactone; PEOEC, Poly(ethylene oxide-co-ethylene carbonate); PEGDA, Poly(ethylene glycol) diacrylate; PEGDE, Poly(ethylene glycol) diglycidyl ether; PTMC, Poly(trimethylene carbonate); PEC, Poly(ethylene carbonate); PPC, Poly(propylene carbonate); CPPC, Cellulose-supported PPC; PMHS, Polymethylhydrosiloxane; ETPTA, Ethoxylated trimethylolpropane triacrylate; SLIC-SPEs, Single lithium-ion conducting-based SPEs; PEGM, Poly(ethylene glycol) methyl ether methacrylate; PEGDM, Poly(ethylene glycol) methyl ether dimethacrylate; PC, Propylene carbonate; PILs, Poly(ionic liquid)s; PDADMA TFSI, Poly(diallyldimethylammonium) bis(trifluoromethanesulfonyl)imide; $\text{P}_{111\text{i}4}\text{FSI}$, Trimethyl(isobutyl)phosphonium bis(fluorosulfonyl)imide; NCPE, Nanocomposite polymer electrolyte; MMT, Montmorillonite; DC, Direct current; LSV, Linear sweep voltammetry; CV, Cyclic voltammogram; XRD, X-Ray Diffraction; SEM, Scanning Electron Microscopy; EDS, Energy Dispersive X-Ray Spectrometer; TEM, Transmission Electron Microscopy; DSC, Differential Scanning Calorimetry; TG, Thermogravimetric; FT-IR, Fourier transform infrared spectrum; EIS, Electrochemical impedance spectroscopy; SSBs, Solid-state batteries; LPS, $\text{Li}_2\text{S-P}_2\text{S}_5$;

ASSLSBs, All-solid-state lithium sulfur batteries; GO, Graphene oxide; rGO, reduced Graphene oxides; CASTEP, Cambridge Serial Total Energy Package; GGA, Generalized gradient approximation; PBE, Perdew-Burke-Ernzerh; LIBs, Lithium batteries; VSB-5, Versailles-Santa Barbara-5; HMT, Hexamethylenetetramine; LiTFSI, Lithium bis(trifluoromethane)sulfonilimide; PVDF, Polyvinylidene fluoride; NMP, N-methyl-2-pyrrolidone; SS, Stainless steel foils; t_{Li}^+ , Li^+ transference number; σ , Ionic conductivity; PVC, Polyvinyl chloride; PAN, Polyacrylonitrile; PVDF-HFP, Poly(vinylidene fluoride-co-hexafluoropropylene); YSZ, Y_2O_3 -doped ZrO_2 ; PEG 300, Polyethylene glycol-300; DTG, Derivative thermogravimetric analysis; SEI, Solid electrolyte interface

Chapter 1 Introduction

1.1 General Introduction

Among currently available batteries, the Lithium (Li) battery is the most promising power storage device for various portable electronic machines because of its high energy density, high operating voltage and long cycle life [1]. However, the Li batteries with organic liquid electrolytes have safety concerns, high cost, and low power density [2]. To solve these issues, solid-state lithium batteries (SSLBs) with the solid-state electrolyte are proposed. Comparing with the flammable liquid electrolytes, the solid-state electrolytes always have (i) better electrochemical stability, (ii) higher safety and durability, and (iii) higher energy and power density and simpler battery design [3-6].

To date, four main solid electrolytes, i.e., solid oxide electrolyte, solid sulfide electrolyte, solid polymer electrolyte (SPE), and organic-inorganic hybrid electrolytes have been developed [7-9]. Among them, the solid oxide electrolyte is the most promising one due to its environmental stability against the ambient air, water and high temperature. However, it still has low ionic conductivity, poor ability to accommodate volume changes, poor wetting of the electrode particles, and high interfacial resistance [10]. In the past few decades, various solid oxide electrolytes with relatively high Li^+ conductivity, e.g., sodium superionic conductor (NASICON) type, perovskite type, garnet type, $\gamma\text{-Li}_3\text{PO}_4$ -type electrolytes, amorphous/glass group including $\text{Li}_2\text{O-MO}_x$ ($\text{M} = \text{Si, B, P, etc.}$) and LiPON-related materials, and some newly developing materials with some special structures, have been developed [11-16]. Especially, the solid oxide electrolyte with the NASICON structure always has fast ion transportation ability as well as long-term stability owing to its interconnected conduction pathways and weak interaction of Li^+

ions in its three-dimensional (3D) framework [17, 18]. Meanwhile, the solid sulfide electrolytes such as $\text{Li}_2\text{S-P}_2\text{S}_5$, $\text{Li}_2\text{S-SiS}_2$, thio-Li super ionic conductor (thio-LISICON) and $\text{Li}_{10}\text{GeP}_2\text{S}_{12}$ (LGPS) have been also considered as the promising candidates since they possess small grain boundary resistance, Li^+ ions conductivity as high as $(1-10)\times 10^{-3} \text{ S}\cdot\text{cm}^{-1}$ at room temperature (RT) and good electrochemical stability [8, 19]. It is reported that the $\text{Li}_2\text{S-P}_2\text{S}_5$ glass-ceramics system with $\text{Li}_7\text{P}_3\text{S}_{11}$ as the metastable phase exhibits a conductivity up to $3.2\times 10^{-3} \text{ S}\cdot\text{cm}^{-1}$ at RT [20], and especially LGPS has an ionic conductivity as high as $12\times 10^{-3} \text{ S}\cdot\text{cm}^{-1}$ [21]. However, these sulfide electrolytes are not stable in the air because they can react with the H_2O to form a toxic gas, H_2S , which causes the preparation of sulfide electrolytes harshly. Compared to the above solid oxide and sulfide electrolytes, the SPEs offer some excellent advantages including good processability, low flammability, good flexibility, safety and close contact with the electrodes [22]. The firstly reported SPE was polyethylene oxide (PEO) incorporated with Li salts [23], in which the Li^+ ion transportability is affected by the number of free Li^+ ions and their moving ability. However, such SPEs always have lower mechanical strength and narrow electrochemical window [24]. Recently, the organic-inorganic hybrid electrolytes by combining organic electrolytes such as the SPEs and inorganic electrolytes such as the solid oxide and sulfide electrolytes were extensively studied to solve the above issues [25-27].

In the following, the state-of-the-arts of various solid electrolyte including the oxide electrolytes, sulfide electrolytes, polymer electrolytes and organic-inorganic hybrid electrolytes are critically reviewed in details. Especially, the main challenges and the utmost limits of those developed solid electrolytes will be summarized, and the future prospects for the further development of novel solid electrolytes will be analyzed. In

addition, several approaches to form favorable interfaces between the electrode and solid electrolyte are reviewed. It is expected to provide a guidance for the development of novel solid electrolytes with higher ionic conductivity and more excellent environmental stability for the SSLBs, and give reasons why I did this research in this dissertation.

1.2 The state-of-the-arts of various solid electrolytes

The solid electrolyte is the critical component of SSLBs, which can enhance the safety greatly by replacing the highly flammable liquid electrolyte. Herein, four types of the developed solid electrolytes, i.e., the solid oxide electrolyte, the sulfide electrolyte, the polymer electrolyte and the organic-inorganic hybrid solid electrolyte, are critically reviewed and discussed at first.

1.2.1 Solid oxide electrolytes

1.2.1.1 NASICON-type

Various solid oxide electrolytes with the 3D NASICON framework have been extensively studied owing to their fast Li^+ ion conductivity as well as excellent structural stability [17, 31, 32]. The first solid oxide electrolyte with the 3D NASICON framework is $\text{Na}_{1+x}\text{Zr}_2\text{Si}_x\text{P}_{3-x}\text{O}_{12}$ reported by Hong and Goodenough [18]. Figure 1.1 shows the typical 3D NASICON structure, which is the framework of $\text{LiM}_2(\text{PO}_4)_3$. One can see that PO_4 tetrahedra and MO_6 octahedra in the $[\text{M}_2(\text{PO}_4)_3]^-$ 3D rigid framework share the corner O atoms with two kinds of sites for Li^+ ions, called Li-I site (octahedral vacancies) and Li-II site (tetrahedra vacancies), which connect together to form 3D channels for Li^+ ion diffusion [24].

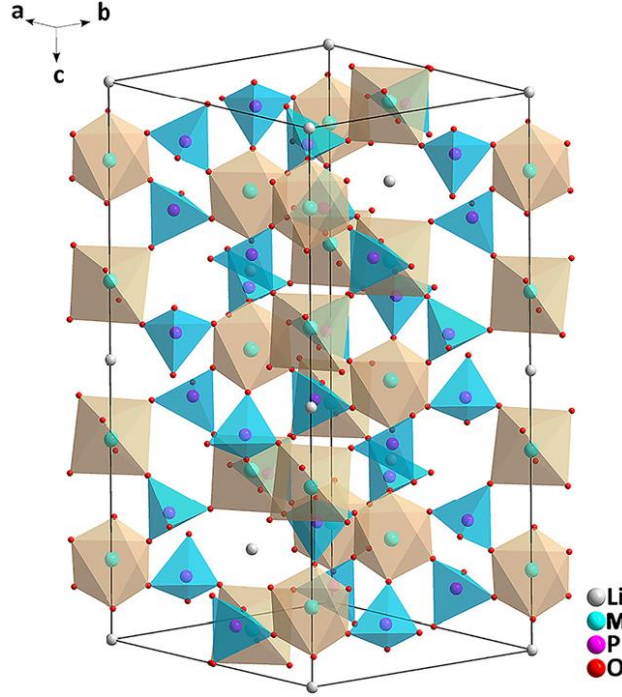


Figure 1.1 3D NASICON-type structure of $\text{LiM}_2(\text{PO}_4)_3$ [24].

In general, the high Li^+ ionic conductivity can be only achieved as the channel size of NASICON framework structure is comparable to the ion size [10]. For example, although $\text{LiZr}_2(\text{PO}_4)_3$ (LZP) has the NASICON structure, its conductivity is very low since the channel size is much larger than the Li^+ ion [33]. To improve its conductivity, other elements were doped on it to tune the interstitial channel size for Li^+ ion diffusion. It is found that the Li^+ ionic conductivity reached a range of 7×10^{-5} - $1.4 \times 10^{-4} \text{ S} \cdot \text{cm}^{-1}$ when Y^{3+} ions were doped in it to form $\text{Li}_{1+x}\text{Y}_x\text{Zr}_{2-x}(\text{PO}_4)_3$ (LYZP) ($0.1 \leq x \leq 0.2$) with a stable rhombohedral structure [34]. Similarly, Al^{3+} -substituted $\text{LiTi}_2(\text{PO}_4)_3$ (LTP), i.e., $\text{Li}_{1.3}\text{Al}_{0.3}\text{Ti}_{1.7}(\text{PO}_4)_3$ (LATP), exhibited a high total Li^+ ionic conductivity of $7 \times 10^{-4} \text{ S} \cdot \text{cm}^{-1}$ [35]. Moreover, doping Nb^{5+} in LATP can further improve the ionic conductivity [36]. The improved conductivity by element substitution is attributable to the increase of the sintered pellet density with the enhancement of the lithium concentration at the grain boundaries [37, 38]. Recently, a new solid oxide of $\text{Li}_{1+x}\text{Al}_x\text{Ge}_{2-x}(\text{PO}_4)_3$ (LAGP) with the

NASICON-type structure was reported to have high conductivity, high electrochemical stability, and wide electrochemical window [39-41]. Hao *et al.* fabricated a SSLB using it as the solid electrolyte, Li film as the anode and sulfur-coated carbon nanotubes (S-MWCNT) as the cathode, and found that the battery exhibited a high capacity of 1510 mAh·g⁻¹ in the first cycle and retained 1400 mAh·g⁻¹ after 30 cycles with the Coulombic efficiency of about 100% for each cycle [42]. To date, it has been proved that the substitution of Zr with the trivalent ion M³⁺ (M = Ge, Ti, V, Co, Hf, Fe, Al, Mn, Sn...) in LZO is an effective way to enhance the total ionic conductivity of this solid oxide electrolyte [33, 43-49]. However, the Li⁺ ionic conductivity and stability of this type solid oxide electrolyte are still desired to be improved more.

1.2.1.2 Perovskite-type

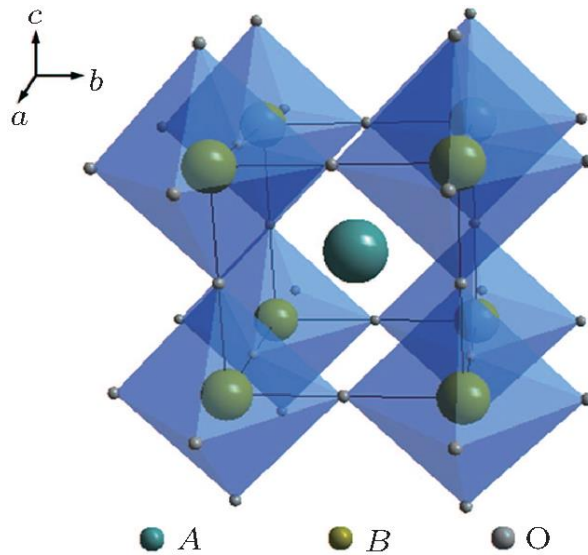


Figure 1.2 Structure schematic of perovskite-type electrolytes (ABO₃) [9].

The solid oxide electrolytes with Perovskite structure (ABO₃) were firstly reported by Latie *et al.* [50] and later by Belous *et al.* [51]. In such a structure, the transition metal element (B) occupies the centre of vertex-sharing BO₆ octahedra, and the high

conductivity is considered to be originated from the transport of Li^+ ions via the deficiencies among the A-sites in the ABO_3 (Figure 1.2). Especially, such a perovskite structure can tolerate the whole or partial replacements of the A and B cations by different ions with different valences to tune its structure and physical properties. $\text{Li}_{3x}\text{La}_{2/3-x}\text{TiO}_3$ (LLTO) is one of the representative perovskite-type electrolytes with high Li^+ ionic conductivity, in which Li and La occupy the A-sites. Since 1980s, Li^+ ionic conductivities of $\text{Li}_{3x}\text{La}_{2/3-x}\text{TiO}_3$ ($0.01 < x < 0.15$) have been widely studied [52-58]. Hiroo *et al.* found that the A-site deficient solid solution, i.e., $\text{Li}_{3x}\text{La}_{2/3-x}\text{TiO}_3$ ($x = 0.1$), is the best one with the Li^+ ionic conductivity as high as $1.1 \times 10^{-3} \text{ S} \cdot \text{cm}^{-1}$ [57]. However, it is found that LLTO is easily reduced by metallic Li anode due to the presence of Ti. Moreover, the grain boundary also results in a very high electrode/electrolyte interface resistance [59-61]. In order to solve these problems, Chen *et al.* investigated a highly conductive perovskite-type $\text{Li}_{3/8}\text{Sr}_{7/16}\text{Ta}_{3/4}\text{Zr}_{1/4}\text{O}_3$ (LSTZ) structure, in which the A and B cations of SrZrO_3 are partially substituted by Li and Ta, respectively, and found that it exhibited high stability above 1.0 V against Li, and a bulk Li^+ ionic conductivity of $2 \times 10^{-4} \text{ S} \cdot \text{cm}^{-1}$ at 30 °C [62]. Meanwhile, Huang *et al.* prepared a $\text{Li}_{3/8}\text{Sr}_{7/16}\text{Ta}_{3/4}\text{Hf}_{1/4}\text{O}_3$ (LSHT) perovskite-type electrolyte with an ionic conductivity of $3.8 \times 10^{-4} \text{ S} \cdot \text{cm}^{-1}$ at 25 °C and an activation energy of 0.36 eV [63]. However, it is necessary to replace the expensive Ta-containing raw materials for reducing the costs. Yu *et al.* substituted Ta by Nb and synthesized a perovskite-type $\text{Li}_{3/8}\text{Sr}_{7/16}\text{Nb}_{3/4}\text{Zr}_{1/4}\text{O}_3$ (LSNZ) solid electrolyte with a total ionic conductivity of $2 \times 10^{-5} \text{ S} \cdot \text{cm}^{-1}$ at 30 °C [64]. Herein, it is important to maintain the high ionic conductivity as well as stability after the substitution of Ta with other cheap materials.

1.2.1.3 Garnet-type

Recently, the solid oxide electrolytes with the Garnet-type structure have also received increasing attention owing to their high ionic conductivity and stability [65-68]. Figure 1.3 shows the typical crystal structure of garnet-type $\text{Li}_3\text{B}_3\text{C}_2\text{O}_{12}$ electrolyte with the cubic $Ia-3d$ framework containing three crystallographically distinct cation coordinations, where Li^+ is an eight-coordination cation, B a four-coordination cation, and C a six-coordination cation. Thangadurai *et al.* and Weppner *et al.* synthesized the garnet-type $\text{Li}_5\text{La}_3\text{M}_2\text{O}_{12}$ ($\text{M} = \text{Nb}, \text{Ta}$) and $\text{Li}_6\text{Ala}_2\text{Ta}_2\text{O}_{12}$ ($\text{A} = \text{Sr}, \text{Ba}$) with a fast Li^+ ionic conductivity, and found that the $\text{Li}_5\text{La}_3\text{M}_2\text{O}_{12}$ with either Nb or Ta exhibited the same order of magnitude of bulk conductivity ($\sim 10^{-6} \text{ S}\cdot\text{cm}^{-1}$ at 25°C) whereas $\text{Li}_6\text{BaLa}_2\text{Ta}_2\text{O}_{12}$ showed the highest ionic conductivity of $4 \times 10^{-5} \text{ S}\cdot\text{cm}^{-1}$ at 22°C [69-71]. Recently, $\text{Li}_7\text{La}_3\text{Zr}_2\text{O}_{12}$ (LLZO) was synthesized as a new garnet-like compound with a superior Li^+ ionic conductivity of $2 \times 10^{-4} \text{ S}\cdot\text{cm}^{-1}$ at RT, high thermal and chemical stability against Li metal, and a wide potential window [72], and used for the SSLBs [65]. Herein, LLZO has two crystallographic phases, i.e., cubic and tetragonal phases, and the LLZO with the cubic phase was found to have higher ionic conductivity than that with the tetragonal phase [12, 73]. However, preparation of the cubic LLZO solid electrolyte needs a high calcination temperature and the SSLB based on it always exhibits a bad performance due to the high electrode/electrolyte interfacial resistance. Fortunately, these problems could be solved by doping other species such as Y, Al, Ta, Nb, Si, Ga, and Te to the Li sublattices [74-81]. Especially, it is found that the dopants of Ga, Ta, and Te can make the electrolytes exhibit excellent total ionic conductivity over $10^{-3} \text{ S}\cdot\text{cm}^{-1}$. Lu *et al.* engineered a novel crystal structure of garnet-type $\text{Li}_{6.25}\text{Ga}_{0.25}\text{La}_3\text{Zr}_2\text{O}_{12}$ (LGLZO) so that the ionic conductivity was significantly increased from $5.43 \times 10^{-4} \text{ S}\cdot\text{cm}^{-1}$ to 1.28×10^{-3}

$\text{S}\cdot\text{cm}^{-1}$ at $25\text{ }^{\circ}\text{C}$ whereas the activation energy was reduced from 0.33 to 0.28 eV [16]. Meanwhile, the calcination temperature for the electrolyte preparation was also lowered. It is expected to develop other ways to improve the performance of the solid oxide electrolyte with the garnet-type structure so that it becomes a promising electrolyte for the SSLBs in the future.

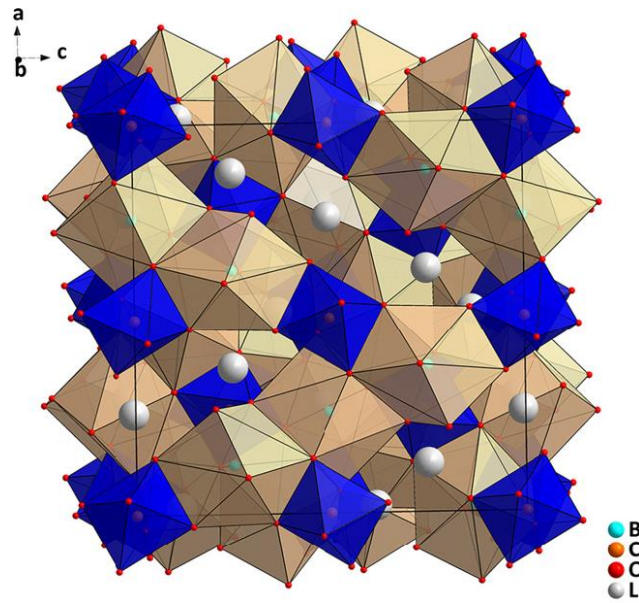


Figure 1.3 The crystal structure of 3D garnet-type $\text{Li}_3\text{B}_3\text{C}_2\text{O}_{12}$ [24].

1.2.1.4 Amorphous/glass-type

Since 1960s, amorphous/glassy oxide electrolytes, denoted as $\text{Li}_2\text{O}-\text{MO}_x$ ($\text{M} = \text{Si}, \text{B}, \text{P}, \text{Ge}, \text{etc.}$) [82-87], have attracted attention. Some of these electrolytes have disordered structures and some of them have network structures (Figure 1.4). In 1966, Otto found that the glass composition of $\text{Li}_2\text{O}-\text{SiO}_2-\text{B}_2\text{O}_3$ with disorder structure had a high ion conductivity ($>10^{-4} \text{ S}\cdot\text{cm}^{-1}$) at a very high temperature of about $350\text{ }^{\circ}\text{C}$ [88]. Thereafter, various attempts have been performed to increase the ionic conductivity at low temperatures by increasing Li_2O concentration, introducing lithium salts, or mixing of

them [89-94]. However, the maximum Li^+ ionic conductivity of such an electrolyte was only $2 \times 10^{-6} \text{ S} \cdot \text{cm}^{-1}$ at 25°C [93].

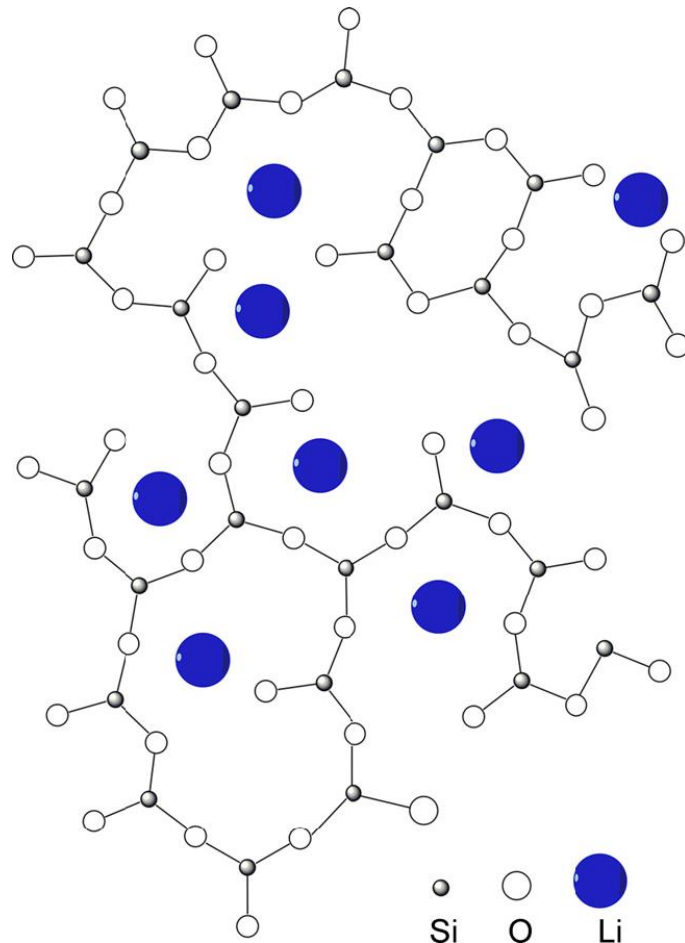


Figure 1.4 Schematic 2D representation of tetrahedrally coordinated $\text{Li}_2\text{O-SiO}_2$ glass [24].

Amorphous solid electrolyte films of $\text{Li}_x\text{PO}_y\text{N}_z$ (LiPON, $x=2y+3z-5$) were developed at Oak Ridge National Laboratory (ORNL) by RF-sputtering or thermal evaporation as the typical glass type solid lithium ion conductors [95-98]. Yu *et al.* studied the electrochemical properties of the LiPON thin films including stability window vs. lithium metal and the behavior of the Li/LiPON interface, and found that LiPON had an average conductivity of $2.3 (\pm 0.7) \times 10^{-6} \text{ S} \cdot \text{cm}^{-1}$ at 25°C with an average activation energy of $0.55 \pm 0.02 \text{ eV}$, high stability in contact with lithium metal, and wide electrochemical

window (0-5.5 V vs Li^+/Li) [99]. It is obvious that their Li^+ ionic conductivity is still too low and needed to be improved more.

1.2.2 Solid sulfide electrolytes

The solid sulfide electrolyte is another promising solid electrolyte, which always exhibits the electrical conductivity higher than $10^{-4} \text{ S}\cdot\text{cm}^{-1}$ at RT because the high polarizability of sulfide ion can weaken the interaction between the anion and Li^+ ion [59]. Importantly, unlike the solid oxide electrolyte, the grain boundary resistance of the solid sulfide electrolyte is much low and its powders can be cold pressed to form an electrolyte film [100]. Nowadays, $\text{Li}_2\text{S-SiS}_2$ and $\text{Li}_2\text{S-P}_2\text{S}_5$ based electrolytes, thio-LISICON family, and $\text{Li}_{4-x}\text{M}_{1-y}\text{M}'_y\text{S}_4$ ($\text{M} = \text{Si, Ge, M}' = \text{P, Al, Zn, Ga}$) are the representative sulfide-based electrolytes [101-109].

1.2.2.1 $\text{Li}_2\text{S-SiS}_2$ based electrolytes

Since Kennedy *et al.* firstly reported that the melt-quenched glass of $\text{Li}_2\text{S-SiS}_2$ exhibited a high Li^+ ionic conductivity of $10^{-4} \text{ S}\cdot\text{cm}^{-1}$ at RT, the electrochemical behaviors of $\text{Li}_2\text{S-SiS}_2$ based electrolytes have been investigated extensively [110]. Thereafter, to improve the ionic conductivity and electrochemical stability, various methods have been tried. The most effective way is doping of other chemicals to the $\text{Li}_2\text{S-SiS}_2$ glass. Kondo *et al.* firstly doped Li_3PO_4 in $\text{Li}_2\text{S-SiS}_2$ glass by a liquid nitrogen quenching method, and found that the obtained glass had improved ionic conductivity and electrochemical stability at RT [111]. Thereafter, Minami and Tatsumisago *et al.* doped various Li_xMO_y including Li_4SiO_4 , Li_3PO_4 , Li_2SO_4 , and Li_4GeO_4 in $\text{Li}_2\text{S-SiS}_2$ glass by combining the rapid quenching method and mechanical ball milling technique, and found that by

addition of a small amount of Li_xMO_y brought about higher ionic conductivity with a value in the range of 10^{-3} - $10^{-4} \text{ S}\cdot\text{cm}^{-1}$ at RT and higher stability against crystallization [112-122].

1.2.2.2 Li_2S - P_2S_5 based electrolytes

The Li_2S - P_2S_5 based electrolytes are also important solid sulfide electrolytes [123-133], which show not only promising electrochemical properties (high ionic conductivity (10^{-4} - $10^{-6} \text{ S}\cdot\text{cm}^{-1}$) and low activation energy) but also high chemical stability in contact with the Li metal. The Li_2S - P_2S_5 sulfide glasses are generally prepared via the melt quenching method, in which the melting must be conducted in a sealed quartz tube because of the high vapor pressure of P_2S_5 [134, 135]. Tatsumisago *et al.* successfully prepared Li_2S - P_2S_5 amorphous solid electrolytes by a mechanical milling method, and found that the obtained $75\text{Li}_2\text{S}$ - $25\text{P}_2\text{S}_5$ exhibited a higher conductivity ($2\times 10^{-4} \text{ S}\cdot\text{cm}^{-1}$ at RT) than that by the melt quenching method [136]. Furthermore, the conductivities of Li_2S - P_2S_5 amorphous solid electrolytes were improved until over $10^{-3} \text{ S}\cdot\text{cm}^{-1}$ by a heat treatment process to increase their crystallinity [20, 103, 137-140]. Herein, the enhanced Li^+ ionic conductivity is considered to be resulted from the precipitation of meta-stable crystalline phase [139]. It should be noted that such superionic metastable phases could not be formed by the solid phase reaction [20, 141]. For the crystallization of Li_2S - P_2S_5 glassy powder, various procedures such as the hot pressing and the dissolution-evaporation at different temperatures and different annealing time have been reported [137, 142-144].

However, the Li_2S - P_2S_5 based solid electrolytes still have some disadvantages such as low chemical stability and easy reaction with moisture to produce H_2S [145, 146].

Moreover, their ion conductivities are still needed to be improved more. Like $\text{Li}_2\text{S-SiS}_2$ based electrolytes, the elemental substitution is also an effective approach to improve Li^+ ionic conductivity as well as chemical stability [147]. Trevey *et al.* prepared $\text{Li}_{4-x}\text{Ge}_{1-x}\text{P}_x\text{S}_{2(1+x)}\text{Se}_{2(1-x)}$ glass-ceramic electrolytes (called $\text{Li}_2\text{S-GeSe}_2\text{-P}_2\text{S}_5$ glass-ceramic electrolyte) by a simple one-step ball milling process, and found that as $x = 0.95$, the obtained $\text{Li}_2\text{S-GeSe}_2\text{-P}_2\text{S}_5$ showed a Li^+ ionic conductivity as high as $1.4 \times 10^{-3} \text{ S} \cdot \text{cm}^{-1}$ since the inclusion of GeSe_2 resulted in the increasing of lattice dimension with the occurrence of new phase [148]. Meanwhile, they prepared another $x\text{Li}_2\text{S-(80-x)Li}_2\text{O-20P}_2\text{S}_5$ glass-ceramic electrolytes (called $\text{Li}_2\text{S-Li}_2\text{O-P}_2\text{S}_5$ glass-ceramic electrolyte) and found that the highest conductivity reached $6.5 \times 10^{-5} \text{ S} \cdot \text{cm}^{-1}$ [149]. To avoid H_2S generation after exposure to air, some metal oxides were added as the H_2S absorbent. For instance, Hayashi *et al.* added M_xO_y (M_xO_y : Fe_2O_3 , ZnO or Bi_2O_3) in the Li_3PS_4 glass, and found that the composite electrolyte of $90\text{Li}_3\text{PS}_4 \cdot 10\text{ZnO}$ exhibited a relatively high conductivity of over $10^{-4} \text{ S} \cdot \text{cm}^{-1}$ while that of $90\text{Li}_3\text{PS}_4 \cdot 10\text{Bi}_2\text{O}_3$ showed the minimum H_2S generation [150]. Yamauchi *et al.* focused on LiBH_4 as a new Li salt additive and mixed it with $75\text{Li}_2\text{S} \cdot 25\text{P}_2\text{S}_5$ glass by a mechanical milling method, and found that the $(100-x)(0.75\text{Li}_2\text{S} \cdot 0.25\text{P}_2\text{S}_5) \cdot x\text{LiBH}_4$ glass at $x = 33$ exhibited the highest conductivity of $1.6 \times 10^{-3} \text{ S} \cdot \text{cm}^{-1}$ [151]. Huang *et al.* reported that the Li^+ ionic conductivity of $70\text{Li}_2\text{S} \cdot 30\text{P}_2\text{S}_5$ can be improved by Li_3PO_4 substitution. As a result, the glass-ceramics substituted with 1 mol% Li_3PO_4 exhibited the highest conductivity of $1.87 \times 10^{-3} \text{ S} \cdot \text{cm}^{-1}$ with the lowest activation energy of $18 \text{ kJ} \cdot \text{mol}^{-1}$ [152]. Lu *et al.* successfully obtained a novel glass-ceramic electrolyte of $(100-x)(70\text{Li}_2\text{S} \cdot 30\text{P}_2\text{S}_5) \cdot x\text{Li}_2\text{ZrO}_3$ ($x = 0, 1, 2, 5$) by a vibratory ball-milling method followed by a heat treatment process. Among the as-prepared ternary electrolyte samples, $99(70\text{Li}_2\text{S} \cdot 30\text{P}_2\text{S}_5) \cdot 1\text{Li}_2\text{ZrO}_3$ glass-ceramic

electrolyte exhibited the highest conductivity of $2.85 \times 10^{-3} \text{ S} \cdot \text{cm}^{-1}$ at RT. Herein, the improvement of electrochemical performance of 99(70Li₂S-30P₂S₅)-1Li₂ZrO₃ glass-ceramic electrolyte is attributed to both the stable crystal structure and the high Li⁺ ion diffusion coefficient of Li₂ZrO₃ [153].

Recently, a series of sulfide crystals of Li_{4-x}M_{1-y}M'_yS₄ (M = Si, Ge, Sn M' = P, Al, Zn, Ga) with the γ -Li₃PO₄ framework structure, called thio-LISICONs, have been synthesized and used as the solid electrolyte [104, 105, 154-160]. The thio-LISICON material was first introduced by Kanno *et al.* [161]. In 2001, they reported a thio-LISICON material, Li_{3.25}Ge_{0.25}P_{0.75}S₄, with a high ionic conductivity ($2.2 \times 10^{-3} \text{ S} \cdot \text{cm}^{-1}$ at 25 °C) [162]. Thereafter, Murayama *et al.* reported another new thio-LISICON compound, Li_{3.4}Si_{0.4}P_{0.6}S₄, with a high ionic conductivity of $6.4 \times 10^{-4} \text{ S} \cdot \text{cm}^{-1}$ at RT, which also showed high electrochemical stability and no reaction with Li metal [163]. Hayashi *et al.* found that the glass-ceramics derived from the mechanically milled Li₂S-SiS₂-P₂S₅ glassy powders also had the structure of the thio-LISICON, and exhibited a high conductivity of $1.2 \times 10^{-3} \text{ S} \cdot \text{cm}^{-1}$ at RT [164]. Ohta *et al.* fabricated a Li_{3.25}Ge_{0.25}P_{0.75}S₄ solid electrolyte thin film with the thio-LISICON structure by a pulsed laser deposition (PLD) method at RT, which showed a high ionic conductivity of $1.7 \times 10^{-4} \text{ S} \cdot \text{cm}^{-1}$ at 25 °C with an activation energy of 0.38 eV for conduction [165]. Very recently, a new thio-LISICON compound, Li₁₀GeP₂S₁₂ (LGPS), was obtained with a very high conductivity of $12 \times 10^{-3} \text{ S} \cdot \text{cm}^{-1}$ at RT [108]. As shown in Figure 1.5, it has a 3D framework structure consisting of (Ge_{0.5}P_{0.5})S₄ tetrahedra, PS₄ tetrahedra, LiS₄ tetrahedra, and LiS₆ octahedra. It is considered that the high ionic conductivity is resulted from the 3D diffusion pathways along *c* axis as well as in *a-b* plane [166-168]. However, due to the scarce deposits and high cost of germanium, LGPS could be difficult to be used in a practical battery. Thusly, it is expected to use some

low-cost isovalent ions to replace germanium. Bron *et al.* successfully synthesized a material named $\text{Li}_{10}\text{SnP}_2\text{S}_{12}$ with a high ionic conductivity of $7 \times 10^{-3} \text{ S} \cdot \text{cm}^{-1}$ by using tin (Sn) to replace the expensive germanium [159].

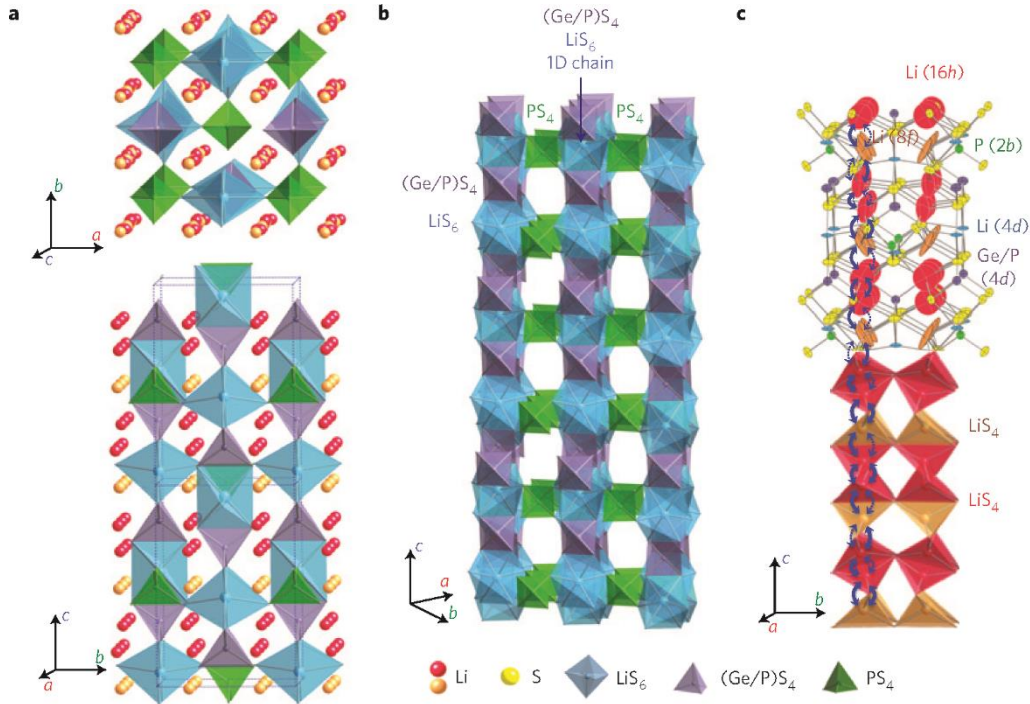


Figure 1.5 Crystal structure of $\text{Li}_{10}\text{GeP}_2\text{S}_{12}$ [108].

1.2.3 Solid polymer electrolytes (SPEs)

The solid polymer electrolytes (SPEs) always use the polymer host as the solid matrix for Li salts in the absence of liquid organic solvents [169]. Compared to the above inorganic solid electrolytes, the SPEs offer better processability, more flexibility besides high safety and stability [170]. In particular, the SPEs can effectively prevent Li dendrite formation and decrease the interface impedance between the electrolyte and electrode [30]. Thusly, the SPEs have been widely developed as the most promising electrolyte candidate for SSLBs [171-173]. To date, poly(ethylene oxide) (PEO) and PEO-like, non-polyether, and single lithium-ion conducting based SPEs have been developed [174-184].

1.2.3.1 PEO and PEO like-based SPEs

The PEO polymers with oligoether ($-\text{CH}_2-\text{CH}_2-\text{O}-$)_n have been widely used as Li^+ ionic conducting electrolytes. After the first report of the ionic conductivities of PEO complexes with alkali metal salts by Wright *et al.* [185], the electrolytes made by PEO incorporating with Li salts have been extensively explored for Li batteries [23]. It is observed that Li salt can be dissolved in the polymer solvent to form cations and anions. Armand *et al.* considered that the ionic mobility should be related to the polymer segmental motion [186], and Ratner and Meyer *et al.* extensively investigated the conduction mechanisms in SPEs [22, 187]. Since PEO-LiX composite always possesses a low ionic conductivity in the order of $10^{-7} \text{ S} \cdot \text{cm}^{-1}$ at RT due to the presence of crystalline domains [188, 189], a variety of methods have been explored to improve the ionic conductivity of PEO-LiX, which include copolymerization with the other monomers, blending with organic solvents or inorganic fillers, and introduction of branching or crosslinking (PEO like).

Blending is one of the most effective ways to reduce crystallinity of the PEO-LiX and increase the electrochemical stability as well as the ionic conductivity [190-195]. Yuan *et al.* fabricated the polyacrylonitrile–polyethylene oxide (PEO–PAN) copolymer by using the macromonomers. The obtained SPE film was transparent and flexible with the ionic conductivity in the range from 3.74×10^{-5} to $6.79 \times 10^{-4} \text{ S} \cdot \text{cm}^{-1}$ at 25 °C and simultaneously the Li-dendrite growth in the charging process of Li batteries was effectively inhibited by the addition of PAN [196]. In addition, the $\text{LiFePO}_4/\text{Li}$ battery using such a SPE exhibited excellent rate capability and high cycling retention owing to its facile ion transport and excellent interfacial compatibility. This provides a route to

develop the advanced SPEs for the future Li batteries with higher performance [197].

Recently, metal organic frameworks (MOFs) have been used as novel fillers in SPEs. Yuan *et al.* incorporated a Zn-based MOF-5 in the PEO based composite polymer electrolytes by an *in-situ* synthesis method, and found that the obtained SPE had a high ionic conductivity of $3.16 \times 10^{-5} \text{ S}\cdot\text{cm}^{-1}$ at 25 °C. Gerbaldi *et al.* also successfully dispersed aluminium-based MOF (Al-BTC MOF) in a PEO-based polymer matrix and produced a SPE for the Li-based batteries with high performance [198].

Moreover, modification of PEO is also an effective method to increase the ionic conductivity of SPEs. Uno *et al.* prepared novel SPEs composed of poly(ethylene oxide) methyl ether methacrylate (PEOMA) unit, α -methylene- γ -butyrolactone (MBL) unit and $\text{LiN}(\text{SO}_2\text{CF}_3)_2$ by the polymer blending, block copolymerization and random copolymerization methods, and found that the combining of the PEOMA unit and MBL unit significantly improved the ionic conductivity at low temperatures [199]. Kwon *et al.* developed a SPE based on poly(ethylene oxide-co-ethylene carbonate) (PEOEC). In comparison with the PEO, the salient features of the PEOEC with amorphous nature and high dielectric constant provided the enhanced ionic conductivity [200].

1.2.3.2 Non-polyether-based SPEs

Besides the PEO host, other SPE materials have also been developed [201, 202]. Bakenov *et al.* prepared a polymeric borate ester plasticized AlPO_4 composite SPE and found that the addition of AlPO_4 improved the performance of SPE effectively [203]. Duan *et al.* constructed an *in-situ* plasticized double-network SPE (poly(ethylene glycol) diacrylate (PEGDA) and poly(ethylene glycol) diglycidyl ether (PEGDE), PEGDA-PEGDE with an appropriate chain length of constitutional unit, and found that the

bendable double-network SPE exhibited an increased ionic conductivity (from 10^{-5} to $10^{-4.5}$ $\text{S}\cdot\text{cm}^{-1}$ at RT), high thermal stability (up to 200 °C) and good capacity to suppress the growth of Li dendrite [204]. The polycarbonate materials can be also tailored for the preparation of novel SPEs. Brandell *et al.* synthesized a high-molecular-weight poly(trimethylene carbonate) (PTMC) as the new host material for SPEs, which showed the electrochemical stability up to 5.0 V vs. Li/Li⁺ and the ionic conductivity on the order of 10^{-7} $\text{S}\cdot\text{cm}^{-1}$ at 60 °C [205]. Meanwhile, Tominaga *et al.* prepared a novel polymer electrolyte composed of poly(ethylene carbonate) (PEC) and Li bis-(fluorosulfonyl) imide with a self-diffusion coefficient of Li⁺ exceeding 10^{-7} $\text{cm}^2\cdot\text{s}^{-1}$ [206]. Cui *et al.* fabricated poly(propylene carbonate) (PPC) PPC-based SPEs and the cellulose-supported PPC (CPPC) CPPC-SPE with the high ionic conductivity at room temperature and wide electrochemical window exceeding 4.6 V [178]. In addition, the polysiloxanes have received much attention as SPEs due to their backbone flexibility, chemical and thermal stability, and low toxicity [207]. Zhang *et al.* synthesized a novel cross-linked siloxane-based solid polymer network by the hydrosilylation of polymethylhydrosiloxane (PMHS) partly substituted with oligo(ethylene glycol) methyl ether side groups and a α,ω -diallyl poly(ethylene glycol) cross-linking reagent, and found that the ionic conductivity of this network doped with LiTFSI was as high as 1.33×10^{-3} $\text{S}\cdot\text{cm}^{-1}$ at ambient temperature [180]. Meanwhile, Lin *et al.* reported a SPE consisting of polysiloxane, poly(vinylidene fluoride) and LiTFSI had an ionic conductivity of 7.9×10^{-5} $\text{S}\cdot\text{cm}^{-1}$ at 25 °C [208]. Furthermore, the plastic crystals with disordered structure could show great plasticity and enhanced diffusivity, which is benefit to the transport of Li⁺ ions [209]. Ha *et al.* developed a highly bendable plastic crystal composite electrolyte based on a UV-crosslinked ethoxylated trimethylolpropane triacrylate (ETPTA) polymer network matrix and a linear polymer of

PVdF-HFP with the succinonitrile (SN-LiTFSI), which showed unprecedented improvement in bendability along with high ionic conductivity [210].

1.2.3.3 Single lithium-ion conducting-based SPEs

The conventional polymer electrolyte is generally the dual ion conductor, in which the migration rate of the anion is about 5-10 times faster than that of the Li^+ ion, resulting in a low Li^+ migration number. To avoid this problem, single lithium-ion conducting-based SPEs (SLIC-SPEs) were considered, in which the anions are covalently bonded to the polymer and/or inorganic backbone, or immobilized by the anion acceptors [211]. To date, various chemical structures have been designed to improve the properties of SLIC-SPEs. Cao *et al.* synthesized a new SLIC with an alternating structure by the simple radical copolymerization of lithium 4-styrenesulfonyl(phenyl-sulfonyl)imide and maleic anhydride, which exhibited both high Li^+ ionic conductivity ($2.67 \times 10^{-3} \text{ S} \cdot \text{cm}^{-1}$) and high transference number (0.98) [212]. Colby *et al.* prepared a polysiloxane SLIC-SPE containing polar cyclic carbonates and weak-binding borate anions with lithium counterions and found that the ionomers with weak-binding borate anions could provide a pathway for the Li^+ ion transference [181]. Furthermore, in order to improve the conductivity of SLIC-SPE, they added a solvating plasticizer (PEG600) with low molecular weight and low-Tg, which effectively increased the ionic conductivity by up to 3 orders of magnitude when compared to the host ionomer. The substantial improvement in ionic conductivity on addition of PEG was considered to be resulted from three factors, i.e., plasticization, homogenization, and solvation [182]. Meanwhile, Armand *et al.* reported a P(STFSILi)-PEO-P(STFSILi) SPE, which exhibited an ionic conductivity of $1.3 \times 10^{-5} \text{ S} \cdot \text{cm}^{-1}$ at 60 °C, a transport number >0.85 , improved mechanical

strength, and enlarged electrochemical stability window up to 5 V versus Li^+/Li [213]. Mecerreyes *et al.* prepared a SLIC-SPE by simple in situ radical copolymerization of the novel lithium sulfonamide methacrylic monomer, poly(ethylene glycol) methyl ether methacrylate (PEGM), and bifunctional poly(ethylene glycol) methyl ether dimethacrylate (PEGDM) in the presence of propylene carbonate (PC), which displayed a high ionic conductivity of $10^{-4} \text{ S}\cdot\text{cm}^{-1}$ at 25 °C [214]. In addition, Poly(ionic liquid)s (PILs) comprising a polymeric backbone and an ionic liquid (IL) species in monomer repeating units can be also used as the SLIC-SPEs [215]. Mecerreyes *et al.* reported the SLIC-PILs via reversible addition-fragmentation chain transfer polymerization technique. These copolymers are comprised of poly(lithium 1-[3-(methacryloyloxy)-propylsulfonyl]-1- (trifluoromethylsulfonyl)imide) and poly(ethylene glycol) methyl ether methacrylate blocks, which showed high ionic conductivity (up to 2.3×10^{-5} and $1.2\times 10^{-5} \text{ S}\cdot\text{cm}^{-1}$ at 25 and 55 °C, respectively), wide electrochemical stability (up to 4.5 V versus Li^+/Li), and a Li^+ transference number close to unity (0.83) [183]. Forsyth *et al.* developed the novel PILs composed of a poly(diallyldimethylammonium)bis(trifluoromethanesulfonyl)- imide (PDADMA TFSI), a high lithium-concentration phosphonium ionic liquid, a trimethyl(isobutyl)phosphonium bis(fluorosulfonyl)imide ($\text{P}_{1114}\text{FSI}$) with Al_2O_3 nanoparticles filler had a high ionic conductivity of $2.8\times 10^{-4} \text{ S}\cdot\text{cm}^{-1}$ at 30 °C [216]. However, these SLIC-SPEs still have low ionic conductivity at RT and bad interfacial property. Thusly, more research efforts are needed to improve these aspects.

1.2.4 Organic-inorganic hybrid electrolytes

The organic-inorganic hybrid electrolytes are generally prepared by dispersing of the

inorganic filler with high active surface and/or high ionic conductivity in the SPEs [170, 217], which is an effective way to enhance the ionic conductivity, mechanical properties and interfacial stability of the hybrid solid electrolyte [218-224]. In general, the inorganic fillers include ZrO_2 [225, 226], Al_2O_3 [227], ZnAl_2O_4 [228], SiO_2 [229], TiO_2 [230], Li_3PO_4 [231], (BaTiO_3 , PbTiO_3 , LiNbO_3 [232, 233]), clay [234-236], carbon nanotubes (CNTs) [237], LLZO [25], LAGP [27] and LGPS [26].

Observations of conductivity enhancement with the addition of ceramic powders were performed by some researchers [238, 239]. It is always considered that the active sites of the surface groups of the ceramic particle could modify the local structure of polymer [227]. Xi *et al.* reported a novel PEO-based nanocomposite polymer electrolyte (NCPE) by using solid superacid of $\text{SO}_4^{2-}/\text{ZrO}_2$ as the filler. The obtained $\text{PEO}_{12}\text{-LiClO}_4\text{-7\%SO}_4^{2-}/\text{ZrO}_2$ electrolyte showed a high RT ionic conductivity of $2.1 \times 10^{-5} \text{ S}\cdot\text{cm}^{-1}$. Herein, it is found that $\text{SO}_4^{2-}/\text{ZrO}_2$ could reduce the crystallinity of PEO effectively through the strong interactions with PEO chains, leading to obvious enhancement of ionic conductivity of the $\text{PEO}_{12}\text{-LiClO}_4$. In addition, $\text{SO}_4^{2-}/\text{ZrO}_2$ could also enhance the Li^+ transference number of the nanocomposite electrolyte [226]. Wang *et al.* investigated $\text{PEO}_{16}\text{-LiClO}_4\text{-ZnAl}_2\text{O}_4$ NCPE prepared by either the hot-pressing or the solution-casting method, and found that the NCPE film prepared by the hot-pressing method had smoother surface, higher interface stability, lower crystallization and lower melting temperature than that prepared by the solution-casting method [228].

It is also found that the addition of Li-exchanged nanoclays (hectotite, laponite and montmorillonite) can improve the performance of SPEs by enhancing the Li transference number [240] since the nanoclays with a layered structure and high dielectric property can provide a large interfacial contact area to improve the solubility of Li salts [236].

Doeff *et al.* reported a single-ion conducting PEO/Li-laponite nanocomposites, in which, by increasing inter-layer spacings and/or intercalating mobile polar oligomers or solvents into the clays, the cation motion coupled with the translational motion of the intercalant, enhancing conductivity greatly. Also, by the addition of a small amount of polymer to such nanocomposites reduced the tendency to film brittleness, resulting in better structural stability [241]. Chen *et al.* demonstrated that the addition of an optimum content of cetyl pyridium chloride-modified montmorillonite increased the ionic conductivity of the PAN-based electrolytes by nearly two orders of magnitude over that of the plain (PAN)₈-LiCF₃SO₃ one. Herein, the presence of montmorillonite could reduce the attractive force between the Li⁺ and anion, producing a highly conductive phase and higher ion conductivity [242]. Recently, Zhang *et al.* reported a simple preparation way for a SPE based on PEO-montmorillonite (MMT) composite. The optimized electrolyte containing 10 wt% MMT exhibited an ionic conductivity of $3.22 \times 10^{-4} \text{ S} \cdot \text{cm}^{-1}$ at 60 °C, a value that met the operation requirement of SSLBs [236].

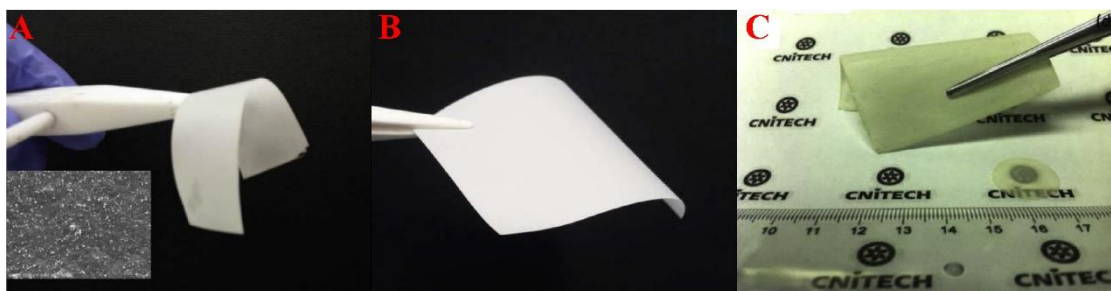


Figure 1.6 Membrane photos of PEO-LLZO (A), PEO-LAGP (B) and PEO-LGPS (C) [25-27].

As stated above, LLZO, LAGP, thio-LISICON and LGPS have attracted increasing attention as solid electrolytes for Li batteries because of their chemical stability (non-reactive with Li metal), high Li⁺ ion conductivity ($\sim 10^{-4} \text{ S} \cdot \text{cm}^{-1}$), and wide potential window ($>5 \text{ V}$ vs. Li/Li⁺). Recently, Choi *et al.* proposed a new concept in which the

garnet-type LLZO solid electrolyte powder was incorporated into a PEO polymer matrix to form a free-standing composite membrane (Figure 1.6A). The as-synthesized hybrid solid electrolytes exhibited enhanced ionic conductivities. It identified that the combination of the organic matrix and the inorganic filler in the solid electrolyte can synergistically enhance the ionic conductivity [25]. Jung *et al.* reported a solvent-free hybrid solid electrolyte (flexible membrane) composed of LAGP and PEO (Figure 1.6B). The addition of LAGP powder into PEO-based SPE improved the electrical and mechanical properties [27]. In order to effectively inhibit the formation of Li dendrites in the LAGP-PEO SPE, Wang *et al.* used a LAGP-PEO SPE and a PEO-LiTFSI modified Li metal anode. It is found that the presence of a PEO-LiTFSI film in the Li anode resulted in a good mechanical property and satisfactory interface contact feature. The film also prevented Li from reacting with LAGP so that the formation of Li dendrites was effectively inhibited [243]. Zhao *et al.* developed a free-standing composite membrane (Figure 1.6C) with a high ionic conductivity and good processing ability through incorporation of LGPS as the active filler into PEO matrix. Herein, it is considered that the improvement of Li^+ conductivity in the PEO matrix was related to the inhibiting of crystallization and weakening of the interactions between the Li^+ ions and the PEO chains. This work provided novel sulfide-based ion conductors combined PEO as the effective solid electrolytes in SSLBs [26].

1.3 Objective of this research

SSLBs using the SEs are considered as an ideal alternative to ultimately realize a safe operation lithium battery. Their broad operating temperature range is also an important benefit from the point of view of energy storage applications. Electrode materials with

large specific capacity, safe operation and low cost are strongly desired for developing and upgrading high-energy-density SSLBs due to the increasing of social demands. SE is a critical component of SSLBs. A SE is utilized to enhance the safety by eliminating the highly flammable liquid electrolytes. Recently, SEs including solid oxide electrolyte, the sulfide electrolyte, the polymer electrolyte and the novel hybrid solid electrolyte have been gained great attention. More importantly, benefiting from the intrinsic solid characteristic of the SE, Li dendrite growth can be suppressed, thus directly employing Li metal as the anode to achieve a higher energy density becomes possible. Using SEs in lithium batteries breaks the standard of conventional lithium batteries. Our purpose is to prepare novel SEs with high ionic conductivity, wide electrochemical windows, high stability and excellent battery performance.

1.4 Scope of dissertation

Chapter 1: The situations of the SEs are critically reviewed, the main challenges and future prospective for the development of SEs are given and the utmost limits of those state-of-the-art SEs are analyzed, and the objectives of this research are listed.

Chapter 2: The synthesis process of various materials, characterization and measurements method are presented.

Chapter 3: A novel $\text{Li}_2\text{S-P}_2\text{S}_5\text{-SeS}_2$ solid sulfide electrolyte was prepared by a facile high-energy ball milling combined annealing way. The effects of doping amount on the crystal structure, the ionic conductivity and electrochemical stabilities of the obtained $70\text{Li}_2\text{S} \cdot (30-x)\text{P}_2\text{S}_5 \cdot x\text{SeS}_2$ ($x=0, 0.3, 0.5, 1, 3, 5$) glass-ceramics were investigated

systematically by experiments and first-principle calculations based on density functional theory (DFT). Furthermore, the solid-state batteries based on this $\text{Li}_2\text{S-P}_2\text{S}_5\text{-SeS}_2$ glass-ceramic and sulfur-reduced graphene oxide (S-rGO) was fabricated and tested.

Chapter 4: A novel PEO-LiTFSI-nanocomposite-based polymer electrolyte was prepared by using VSB-5 nanorods as the filler. The effect of VSB-5 addition on the crystallinity, the ionic conductivity, thermal stability and electrochemical windows were investigated via XRD, Fourier transform infrared (FTIR), SEM, EIS, linear sweep voltammetry (LSV), thermogravimetric analysis (TGA), and differential scanning calorimetry (DSC) test. Meanwhile, Li^+ transference number and the stability with lithium metal were tested by the Li symmetrical battery. Furthermore, the SSLBs with the PEO-LiTFSI-x% VSB-5 SPE, LiFePO_4 -based cathode, and Li anode were assembled and their electrochemical performances were evaluated.

Chapter 5: A novel solid polymer composite electrolyte based on PEO with rod-like $\text{Zn}_2(\text{OH})\text{BO}_3$ particles was prepared by a grinding process followed with a heating treatment process and a cold pressing process. The structure and mechanism of improved property base on such rod-like $\text{Zn}_2(\text{OH})\text{BO}_3$ particles-filled SPEs were systematically investigated. The performance of the PEO-LiTFSI-10% $\text{Zn}_2(\text{OH})\text{BO}_3$ was further evaluated by assembling SSLBs using the lithium metal anode and the LiFePO_4 cathode.

Chapter 6: General conclusions of this research and the challenges and prospects for the future work were presented.

References

- [1] K. Aso, A. Hayashi, M. Tatsumisago, Synthesis of NiS–carbon fiber composites in high-boiling solvent to improve electrochemical performance in all-solid-state lithium secondary batteries, *Electrochim. Acta* 83 (2012) 448-453.
- [2] C. Sun, J. Liu, Y. Gong, D.P. Wilkinson, J. Zhang, Recent advances in all-solid-state rechargeable lithium batteries, *Nano Energy*, 33 (2017) 363-386.
- [3] U. Ulissi, M. Agostini, S. Ito, Y. Aihara, J. Hassoun, All solid-state battery using layered oxide cathode, lithium-carbon composite anode and thio-LISICON electrolyte, *Solid State Ionics*, 296 (2016) 13-17.
- [4] T. Baba, Y. Kawamura, Structure and ionic conductivity of $\text{Li}_2\text{S-P}_2\text{S}_5$ glass electrolytes simulated with first-principles molecular dynamics, *Frontiers in Energy Research* 4 (2016) 22.
- [5] A. Hayashi, Y. Nishio, H. Kitauro, M. Tatsumisago, Novel technique to form electrode-electrolyte nanointerface in all-solid-state rechargeable lithium batteries, *Electrochem. Commun.* 10 (2008) 1860-1863.
- [6] S. Chen, D. Xie, G. Liu, J.P. Mwizerwa, Q. Zhang, Y. Zhao, X. Xu, X. Yao, Sulfide SEs for all-solid-state lithium batteries: structure, conductivity, stability and application, *Energy Storage Mater.* 14 (2018) 58-74.
- [7] A. Manthiram, X. Yu, S. Wang, Lithium battery chemistries enabled by solid-state electrolytes, *Nat. Rev. Mater.* 2 (2017) 16103.
- [8] R.C. Xu, X.L. Wang, S.Z. Zhang, Y. Xia, X.H. Xia, J.B. Wu, J.P. Tu, Rational coating of $\text{Li}_7\text{P}_3\text{S}_{11}$ solid electrolyte on MoS_2 electrode for all-solid-state lithium ion batteries, *J. Power Sources* 374 (2018) 107-112.
- [9] X. Yao, B. Huang, J. Yin, G. Peng, Z. Huang, C. Gao, D. Liu, X. Xu, All-solid-state

- lithium batteries with inorganic SEs: Review of fundamental science, *Chin. Phys. B* 25 (2016) 018802.
- [10] V. Thangadurai, W. Weppner, Recent progress in solid oxide and lithium ion conducting electrolytes research, *Ionics* 12 (2006) 81-92.
- [11] Y. Harada, T. Ishigaki, H. Kawai, J. Kuwano, Lithium ion conductivity of polycrystalline perovskite $\text{La}_{0.67-x}\text{Li}_{3x}\text{TiO}_3$ with ordered and disordered arrangements of the A-site ions, *Solid State Ionics* 108 (1998) 407-413.
- [12] R. Murugan, V. Thangadurai, W. Weppner, Fast lithium ion conduction in garnet-type $\text{Li}_7\text{La}_3\text{Zr}_2\text{O}_{12}$, *Angew. Chem., Int. Ed.* 46 (2007) 7778-7781.
- [13] H. Xu, S. Wang, H. Wilson, F. Zhao, A. Manthiram, Y-Doped NASICON-type $\text{LiZr}_2(\text{PO}_4)_3$ SEs for Lithium-Metal Batteries, *Chem. Mater.* 29 (2017) 7206-7212.
- [14] P. Bruce, A. West, Ionic conductivity of LISICON solid solutions, $\text{Li}_{2+2x}\text{Zn}_{1-x}\text{GeO}_4$, *J. Solid State Chem.* 44 (1982) 354-365.
- [15] R. Jaleem, M. Nakayama, T. Kasuga, Lithium ion conduction in tavorite-type LiMXO_4F (M-X: AlP, MgS) candidate solid electrolyte materials, *Solid State Ionics* 262 (2014) 589-592.
- [16] Y. Lu, X. Meng, J.A. Alonso, M.T. Fernández-Díaz, C. Sun, Effects of fluorine doping on structural and electrochemical properties of $\text{Li}_{6.25}\text{Ga}_{0.25}\text{La}_3\text{Zr}_2\text{O}_{12}$ as electrolytes for solid-state lithium batteries, *ACS Appl. Mater. Interfaces* 11 (2018) 2042-2049.
- [17] C. Masquelier, L. Croguennec, Polyanionic (phosphates, silicates, sulfates) frameworks as electrode materials for rechargeable Li (or Na) batteries, *Chem. Rev.* 113 (2013) 6552-6591.
- [18] J. Goodenough, H.-P. Hong, J. Kafalas, Fast Na^+ -ion transport in skeleton structures,

- Mater. Res. Bull. 11 (1976) 203-220.
- [19] A. Hayashi, M. Tatsumisago, Recent development of bulk-type solid-state rechargeable lithium batteries with sulfide glass-ceramic electrolytes, *Electron. Mater. Lett.* 8 (2012) 199-207.
- [20] F. Mizuno, A. Hayashi, K. Tadanaga, M. Tatsumisago, New, highly ion-conductive crystals precipitated from Li_2S – P_2S_5 glasses, *Adv. Mater.* 17 (2005) 918-921.
- [21] N. Kamaya, K. Homma, Y. Yamakawa, M. Hirayama, R. Kanno, M. Yonemura, T. Kamiyama, Y. Kato, S. Hama, K. Kawamoto, A lithium superionic conductor, *Nat. Mater.* 10 (2011) 682.
- [22] W.H. Meyer, Polymer electrolytes for lithium-ion batteries, *Adv. Mater.* 10 (1998) 439-448.
- [23] G.S. MacGlashan, Y.G. Andreev, P.G. Bruce, Structure of the polymer electrolyte poly (ethylene oxide)₆: LiAsF_6 , *Nature* 398 (1999) 792.
- [24] Y. Ren, K. Chen, R. Chen, T. Liu, Y. Zhang, C.W. Nan, Oxide electrolytes for lithium batteries, *J. Am. Ceram. Soc.* 98 (2015) 3603-3623.
- [25] J.-H. Choi, C.-H. Lee, J.-H. Yu, C.-H. Doh, S.-M. Lee, Enhancement of ionic conductivity of composite membranes for all-solid-state lithium rechargeable batteries incorporating tetragonal $\text{Li}_7\text{La}_3\text{Zr}_2\text{O}_{12}$ into a polyethylene oxide matrix, *J. Power Sources* 274 (2015) 458-463.
- [26] Y. Zhao, C. Wu, G. Peng, X. Chen, X. Yao, Y. Bai, F. Wu, S. Chen, X. Xu, A new solid polymer electrolyte incorporating $\text{Li}_{10}\text{GeP}_2\text{S}_{12}$ into a polyethylene oxide matrix for all-solid-state lithium batteries, *J. Power Sources* 301 (2016) 47-53.
- [27] Y.C. Jung, S.M. Lee, J.H. Choi, S.S. Jang, D.W. Kim, All solid-state lithium batteries assembled with hybrid SEs, *J. Electrochem. Soc.* 162 (2015) A704-A710.

- [28] Z. Wu, Z. Xie, A. Yoshida, Z. Wang, X. Hao, A. Abudula, G. Guan, Utmost limits of various solid electrolytes in all-solid-state lithium batteries: A critical review, *Renewable Sustainable Energy Rev.* 109 (2019) 367-385.
- [29] J.C. Bachman, S. Muy, A. Grimaud, H.-H. Chang, N. Pour, S.F. Lux, O. Paschos, F. Maglia, S. Lupart, P. Lamp, Inorganic solid-state electrolytes for lithium batteries: mechanisms and properties governing ion conduction, *Chem. Rev.* 116 (2016) 140-162.
- [30] L. Yue, J. Ma, J. Zhang, J. Zhao, S. Dong, Z. Liu, G. Cui, L. Chen, All solid-state polymer electrolytes for high-performance lithium ion batteries, *Energy Storage Mater.* 5 (2016) 139-164.
- [31] F. Lalère, J.B. Leriche, M. Courty, S. Boulineau, V. Viallet, C. Masquelier, V. Seznec, An all-solid state NASICON sodium battery operating at 200 °C, *J. Power Sources* 247 (2014) 975-980.
- [32] H. El-Shinawi, A. Regoutz, D.J. Payne, E.J. Cussen, S.A. Corr, NASICON $\text{LiM}_2(\text{PO}_4)_3$ electrolyte ($\text{M}=\text{Zr}$) and electrode ($\text{M}=\text{Ti}$) materials for all solid-state Li-ion batteries with high total conductivity and low interfacial resistance, *J. Mater. Chem. A* 6 (2018) 5296-5303.
- [33] M. Subramanian, R. Subramanian, A. Clearfield, Lithium ion conductors in the system $\text{AB(IV)}_2(\text{PO}_4)_3$ ($\text{B}=\text{Ti}$, Zr and Hf), *Solid State Ionics* 18 (1986) 562-569.
- [34] Y. Li, M. Liu, K. Liu, C.-A. Wang, High Li^+ conduction in NASICON-type $\text{Li}_{1+x}\text{Y}_x\text{Zr}_{2-x}(\text{PO}_4)_3$ at room temperature, *J. Power Sources* 240 (2013) 50-53.
- [35] H. Aono, E. Sugimoto, Y. Sadaoka, N. Imanaka, G.y. Adachi, Ionic conductivity of SEs based on lithium titanium phosphate, *J. Electrochem. Soc.* 137 (1990) 1023-1027.
- [36] O. Gromov, G. Kunshina, A. Kuz'min, V. Kalinnikov, Ionic conductivity of SEs

- based on $\text{Li}_{1.3}\text{Al}_{0.3}\text{Ti}_{1.7}(\text{PO}_4)_3$, Russ. J. Appl. Chem. 69 (1996) 385-388.
- [37] W. Zhao, L. Chen, R. Xue, J. Min, W. Cui, Ionic conductivity and luminescence of Eu^{3+} -doped $\text{LiTi}_2(\text{PO}_4)_3$, Solid state ionics 70 (1994) 144-146.
- [38] H. Aono, E. Sugimoto, Y. Sadaoka, N. Imanaka, G.-y. Adachi, Electrical properties and sinterability for lithium germanium phosphate $\text{Li}_{1+x}\text{M}_x\text{Ge}_{2-x}(\text{PO}_4)_3$, M=Al, Cr, Ga, Fe, Sc, and In systems, Bull. Chem. Soc. Jpn. 65 (1992) 2200-2204.
- [39] P. Hartmann, T. Leichtweiss, M.R. Busche, M. Schneider, M. Reich, J. Sann, P. Adelhelm, J. Janek, Degradation of NASICON-type materials in contact with lithium metal: formation of mixed conducting interphases (MCI) on SEs, J. Phys. Chem. C 117 (2013) 21064-21074.
- [40] E. Kobayashi, L.S. Plashnitsa, T. Doi, S. Okada, J.-i. Yamaki, Electrochemical properties of Li symmetric solid-state cell with NASICON-type solid electrolyte and electrodes, Electrochem. Commun. 12 (2010) 894-896.
- [41] K. Arbi, W. Bucheli, R. Jiménez, J. Sanz, High lithium ion conducting SEs based on NASICON $\text{Li}_{1+x}\text{Al}_x\text{M}_{2-x}(\text{PO}_4)_3$ materials (M = Ti, Ge and $0 \leq x \leq 0.5$), J. Eur. Ceram. Soc 35 (2015) 1477-1484.
- [42] Y. Hao, S. Wang, F. Xu, Y. Liu, N. Feng, P. He, H. Zhou, A design of solid-state Li-S cell with evaporated lithium anode to eliminate shuttle effects, ACS Appl. Mater. Interfaces 9 (2017) 33735-33739.
- [43] P. Fu, Y. Zhao, Y. Dong, X. An, G. Shen, Synthesis of $\text{Li}_3\text{V}_2(\text{PO}_4)_3$ with high performance by optimized solid-state synthesis routine, J. Power Sources 162 (2006) 651-657.
- [44] Y. Kee, N. Dimov, E. Kobayashi, A. Kitajou, S. Okada, Structural and electrochemical properties of Fe- and Al-doped $\text{Li}_3\text{V}_2(\text{PO}_4)_3$ for all-solid-state

- symmetric lithium ion batteries prepared by spray-drying-assisted carbothermal method, *Solid State Ionics* 272 (2015) 138-143.
- [45] A. Salah, P. Jozwiak, J. Garbarczyk, K. Benkhoucha, K. Zaghib, F. Gendron, C. Julien, Local structure and redox energies of lithium phosphates with olivine- and Nasicon-like structures, *J. Power Sources* 140 (2005) 370-375.
- [46] P. Fu, Y. Zhao, Y. Dong, X. An, G. Shen, Low temperature solid-state synthesis routine and mechanism for $\text{Li}_3\text{V}_2(\text{PO}_4)_3$ using LiF as lithium precursor, *Electrochim. Acta* 52 (2006) 1003-1008.
- [47] H. Aono, E. Sugimoto, Y. Sadaoka, N. Imanaka, G.-y. Adachi, Electrical properties and crystal structure of solid electrolyte based on lithium hafnium phosphate $\text{LiHf}_2(\text{PO}_4)_3$, *Solid State Ionics* 62 (1993) 309-316.
- [48] H. Aono, E. Sugimoto, Y. Sadaoka, N. Imanaka, G.y. Adachi, The electrical properties of ceramic electrolytes for $\text{LiM}_x\text{Ti}_{2-x}(\text{PO}_4)_{3+y}\text{Li}_2\text{O}$, M= Ge, Sn, Hf, and Zr systems, *J. Electrochem. Soc.* 140 (1993) 1827-1833.
- [49] A. Inoishi, A. Nishio, Y. Yoshioka, A. Kitajou, S. Okada, Single-phase all-solid-state lithium battery based on $\text{Li}_{1.5}\text{Cr}_{0.5}\text{Ti}_{1.5}(\text{PO}_4)_3$ for high rate capability and low temperature operation, *Chem. Commun.* 54 (2018) 3178-3181.
- [50] L. Latie, G. Villeneuve, D. Conte, G. Le Flem, Ionic conductivity of oxides with general formula $\text{Li}_x\text{Ln}_{1/3}\text{Nb}_{1-x}\text{Ti}_x\text{O}_3$ (Ln= La, Nd), *J. Solid State Chem.* 51 (1984) 293-299.
- [51] A. Belous, G. Novitskaya, S. Polyanetskaya, Y.I. Gornikov, Investigation into complex oxides of $\text{La}_{2/3-x}\text{Li}_{3x}\text{TiO}_3$ composition, *Izv. Akad. Nauk SSSR, Neorg. Mater.* 23 (1987) 470-472.
- [52] Y. Harada, Y. Hirakoso, H. Kawai, J. Kuwano, Order–disorder of the A-site ions and

- lithium ion conductivity in the perovskite solid solution $\text{La}_{0.67-x}\text{Li}_{3x}\text{TiO}_3$ ($x=0.11$), Solid State Ionics 121 (1999) 245-251.
- [53] O. Bohnke, C. Bohnke, J. Fourquet, Mechanism of ionic conduction and electrochemical intercalation of lithium into the perovskite lanthanum lithium titanate, Solid State Ionics 91 (1996) 21-31.
- [54] Y. Inaguma, T. Katsumata, M. Itoh, Y. Morii, Crystal structure of a lithium ion-conducting perovskite $\text{La}_{2/3-x}\text{Li}_{3x}\text{TiO}_3$ ($x=0.05$), J. Solid State Chem. 166 (2002) 67-72.
- [55] Y. Inaguma, M. Itoh, Influences of carrier concentration and site percolation on lithium ion conductivity in perovskite-type oxides, Solid State Ionics 86 (1996) 257-260.
- [56] Y. Inaguma, Y. Matsui, Y.-J. Shan, M. Itoh, T. Nakamura, Lithium ion conductivity in the perovskite-type $\text{LiTaO}_3\text{-SrTiO}_3$ solid solution, Solid State Ionics 79 (1995) 91-97.
- [57] H. Kawai, J. Kuwano, Lithium ion conductivity of A-site deficient perovskite solid solution $\text{La}_{0.67-x}\text{Li}_{3x}\text{TiO}_3$, J. Electrochem. Soc. 141 (1994) L78-L79.
- [58] Y.J. Shan, L. Chen, Y. Inaguma, M. Itoh, T. Nakamura, Oxide cathode with perovskite structure for rechargeable lithium batteries, J. Power Sources 54 (1995) 397-402.
- [59] K. Takada, Progress and prospective of solid-state lithium batteries, Acta Mater. 61 (2013) 759-770.
- [60] Y. Kobayashi, T. Takeuchi, M. Tabuchi, K. Ado, H. Kageyama, Densification of $\text{LiTi}_2(\text{PO}_4)_3$ -based SEs by spark-plasma-sintering, J. Power Sources 81 (1999) 853-858.

- [61] H. Aono, E. Sugimoto, Y. Sadaoka, N. Imanaka, G.-y. Adachi, Electrical property and sinterability of $\text{LiTi}_2(\text{PO}_4)_3$ mixed with lithium salt (Li_3PO_4 or Li_3BO_3), *Solid State Ionics* 47 (1991) 257-264.
- [62] C. Chen, S. Xie, E. Sperling, A. Yang, G. Henriksen, K. Amine, Stable lithium-ion conducting perovskite lithium-strontium-tantalum-zirconium-oxide system, *Solid State Ionics* 167 (2004) 263-272.
- [63] B. Huang, B. Xu, Y. Li, W. Zhou, Y. You, S. Zhong, C.-A. Wang, J.B. Goodenough, Li-ion conduction and stability of perovskite $\text{Li}_{3/8}\text{Sr}_{7/16}\text{Hf}_{1/4}\text{Ta}_{3/4}\text{O}_3$, *ACS Appl Mater Interfaces* 8 (2016) 14552-14557.
- [64] R. Yu, Q.-X. Du, B.-K. Zou, Z.-Y. Wen, C.-H. Chen, Synthesis and characterization of perovskite-type $(\text{Li}, \text{Sr})(\text{Zr}, \text{Nb})\text{O}_3$ quaternary solid electrolyte for all-solid-state batteries, *J. Power Sources* 306 (2016) 623-629.
- [65] K.K. Fu, Y. Gong, G.T. Hitz, D.W. McOwen, Y. Li, S. Xu, Y. Wen, L. Zhang, C. Wang, G. Pastel, Three-dimensional bilayer garnet solid electrolyte based high energy density lithium metal–sulfur batteries, *Energy Environ. Sci.* 10 (2017) 1568-1575.
- [66] M. Saccoccio, J. Yu, Z. Lu, S.C. Kwok, J. Wang, K.K. Yeung, M.M. Yuen, F. Ciucci, Low temperature pulsed laser deposition of garnet $\text{Li}_{6.4}\text{La}_3\text{Zr}_{1.4}\text{Ta}_{0.6}\text{O}_{12}$ films as all solid-state lithium battery electrolytes, *J. Power Sources* 365 (2017) 43-52.
- [67] R.-H. Shin, S.I. Son, Y.S. Han, Y. Do Kim, H.-T. Kim, S.-S. Ryu, W. Pan, Sintering behavior of garnet-type $\text{Li}_7\text{La}_3\text{Zr}_2\text{O}_{12}$ - Li_3BO_3 composite SEs for all-solid-state lithium batteries, *Solid State Ionics* 301 (2017) 10-14.
- [68] T. Liu, Y. Zhang, X. Zhang, L. Wang, S.-X. Zhao, Y.-H. Lin, Y. Shen, J. Luo, L. Li, C.-W. Nan, Enhanced electrochemical performance of bulk type oxide ceramic lithium batteries enabled by interface modification, *J. Mater. Chem. A* 6 (2018) 4649-

4657.

- [69] V. Thangadurai, W. Weppner, $\text{Li}_6\text{AlLa}_2\text{Ta}_2\text{O}_{12}$ (A= Sr, Ba): Novel garnet-like oxides for fast lithium ion conduction, *Adv. Funct. Mater.* 15 (2005) 107-112.
- [70] V. Thangadurai, H. Kaack, W.J. Weppner, Novel fast lithium ion conduction in garnet-type $\text{Li}_5\text{La}_3\text{M}_2\text{O}_{12}$ (M= Nb, Ta), *J. Am. Ceram. Soc.* 86 (2003) 437-440.
- [71] V. Thangadurai, W. Weppner, Effect of sintering on the ionic conductivity of garnet-related structure $\text{Li}_5\text{La}_3\text{Nb}_2\text{O}_{12}$ and In- and K-doped $\text{Li}_5\text{La}_3\text{Nb}_2\text{O}_{12}$, *J. Solid State Chem.* 179 (2006) 974-984.
- [72] A. Kaeriyama, H. Munakata, K. Kajihara, K. Kanamura, Y. Sato, T. Yoshida, Evaluation of electrochemical characteristics of $\text{Li}_7\text{La}_3\text{Zr}_2\text{O}_{12}$ solid electrolyte, *ECS Trans.* 16 (2009) 175-180.
- [73] Y. Shimonishi, A. Toda, T. Zhang, A. Hirano, N. Imanishi, O. Yamamoto, Y. Takeda, Synthesis of garnet-type $\text{Li}_{7-x}\text{La}_3\text{Zr}_2\text{O}_{12-1/2x}$ and its stability in aqueous solutions, *Solid State Ionics* 183 (2011) 48-53.
- [74] S. Kumazaki, Y. Iriyama, K.-H. Kim, R. Murugan, K. Tanabe, K. Yamamoto, T. Hirayama, Z. Ogumi, High lithium ion conductive $\text{Li}_7\text{La}_3\text{Zr}_2\text{O}_{12}$ by inclusion of both Al and Si, *Electrochem. Commun.* 13 (2011) 509-512.
- [75] R. Murugan, S. Ramakumar, N. Janani, High conductive yttrium doped $\text{Li}_7\text{La}_3\text{Zr}_2\text{O}_{12}$ cubic lithium garnet, *Electrochem. Commun.* 13 (2011) 1373-1375.
- [76] H. El Shinawi, J. Janek, Stabilization of cubic lithium-stuffed garnets of the type “ $\text{Li}_7\text{La}_3\text{Zr}_2\text{O}_{12}$ ” by addition of gallium, *J. Power Sources* 225 (2013) 13-19.
- [77] S. Afyon, F. Krumeich, J.L. Rupp, A shortcut to garnet-type fast Li-ion conductors for all-solid state batteries, *J. Mater. Chem. A* 3 (2015) 18636-18648.
- [78] W. Gu, M. Ezbiri, R.P. Rao, M. Avdeev, S. Adams, Effects of penta-and trivalent

- dopants on structure and conductivity of $\text{Li}_7\text{La}_3\text{Zr}_2\text{O}_{12}$, *Solid State Ionics* 274 (2015) 100-105.
- [79] N. Bernstein, M. Johannes, K. Hoang, Origin of the structural phase transition in $\text{Li}_7\text{La}_3\text{Zr}_2\text{O}_{12}$, *Phys. Rev. Lett.* 109 (2012) 205702.
- [80] C. Deviannapoorani, L. Dhivya, S. Ramakumar, R. Murugan, Lithium ion transport properties of high conductive tellurium substituted $\text{Li}_7\text{La}_3\text{Zr}_2\text{O}_{12}$ cubic lithium garnets, *J. Power Sources* 240 (2013) 18-25.
- [81] S. Hu, Y.-F. Li, R. Yang, Z. Yang, L. Wang, Structure and ionic conductivity of $\text{Li}_7\text{La}_3\text{Zr}_{2-x}\text{Ge}_x\text{O}_{12}$ garnet-like solid electrolyte for all solid state lithium ion batteries, *Ceram. Int.* 44 (2018) 6614-6618.
- [82] R. Charles, Some structural and electrical properties of lithium silicate glasses, *J. Am. Ceram. Soc.* 46 (1963) 235-238.
- [83] S.W. Martin, Ionic conduction in phosphate glasses, *J. Am. Ceram. Soc.* 74 (1991) 1767-1784.
- [84] L.D. Pye, V.D. Fréchette, N.J. Kreidl, *Borate glasses: structure, properties, applications*, Springer Science & Business Media 2012.
- [85] M.A. Levasseur, B. Calès, J.-M. Réau, P. Hagenmuller, Conductivite ionique du lithium dans les verres du systeme $\text{B}_2\text{O}_3\cdot\text{Li}_2\text{O}\cdot\text{LiCl}$, *Mater. Res. Bull.* 13 (1978) 205-209.
- [86] M. Doreau, A.A. El Anouar, G. Robert, Domaine vitreux, structure et conductivite electrique des verres du systeme $\text{LiCl}/1\text{bLi}_2\text{O}/1\text{bP}_2\text{O}_5$, *Mater. Res. Bull.* 15 (1980) 285-294.
- [87] M.K. MURTHY, J. Ip, Studies in germanium oxide systems: I, phase equilibria in the system $\text{Li}_2\text{O}\text{-GeO}_2$, *J. Am. Ceram. Soc.* 47 (1964) 328-331.

- [88] K. Otto, Electrical conductivity of $\text{SiO}_2\text{-B}_2\text{O}_3$ glasses containing lithium or sodium, *Phys. Chem. Glasses* 7 (1966) 29.
- [89] A. Levasseur, J.-C. Brethous, J.-M. Réau, P. Hagenmuller, Etude comparee de la conductivite ionique du lithium dans les halogenoborates vitreux, *Mater. Res. Bull.* 14 (1979) 921-927.
- [90] A. Pradel, T. Pagnier, M. Ribes, Effect of rapid quenching on electrical properties of lithium conductive glasses, *Solid State Ionics* 17 (1985) 147-154.
- [91] K. Tanaka, T. Yoko, H. Yamada, K. Kamiya, Structure and ionic conductivity of $\text{LiCl}\cdot\text{Li}_2\text{O}\cdot\text{TeO}_2$ glasses, *J. Non-Cryst. Solids* 103 (1988) 250-256.
- [92] Y.-I. Lee, J.-H. Lee, S.-H. Hong, Y. Park, Li-ion conductivity in $\text{Li}_2\text{O-B}_2\text{O}_3\text{-V}_2\text{O}_5$ glass system, *Solid State Ionics* 175 (2004) 687-690.
- [93] C.E. Kim, H.C. Hwang, M.Y. Yoon, B.H. Choi, H.J. Hwang, Fabrication of a high lithium ion conducting lithium borosilicate glass, *J. Non-Cryst. Solids* 357 (2011) 2863-2867.
- [94] C.-H. Lee, K. Joo, J. Kim, S. Woo, H.-J. Sohn, T. Kang, Y. Park, J. Oh, Characterizations of a new lithium ion conducting $\text{Li}_2\text{O-SeO}_2\text{-B}_2\text{O}_3$ glass electrolyte, *Solid State Ionics* 149 (2002) 59-65.
- [95] J. Bates, N. Dudney, G. Gruzalski, R. Zuhr, A. Choudhury, C. Luck, J. Robertson, Electrical properties of amorphous lithium electrolyte thin films, *Solid state ionics* 53 (1992) 647-654.
- [96] J. Bates, N. Dudney, G. Gruzalski, R. Zuhr, A. Choudhury, C. Luck, J. Robertson, Fabrication and characterization of amorphous lithium electrolyte thin films and rechargeable thin-film batteries, *J. Power Sources* 43 (1993) 103-110.
- [97] J. Bates, G. Gruzalski, N. Dudney, C. Luck, X. Yu, Rechargeable thin-film lithium

- batteries, *Solid State Ionics* 70 (1994) 619-628.
- [98] N.J. Dudney, Thin film micro-batteries, *Electrochem. Soc. Interface* 17 (2008) 44.
- [99] X. Yu, J. Bates, G. Jellison Jr, F. Hart, A stable thin-film lithium electrolyte: lithium phosphorus oxynitride, *J. Electrochem. Soc.* 144 (1997) 524-532.
- [100] K. Takada, S. Kondo, Lithium ion conductive glass and its application to solid state batteries, *Ionics* 4 (1998) 42-47.
- [101] M. Murayama, N. Sonoyama, A. Yamada, R. Kanno, Material design of new lithium ionic conductor, thio-LISICON, in the $\text{Li}_2\text{S}-\text{P}_2\text{S}_5$ system, *Solid State Ionics* 170 (2004) 173-180.
- [102] T. Ohtomo, F. Mizuno, A. Hayashi, K. Tadanaga, M. Tatsumisago, Electrical and electrochemical properties of $\text{Li}_2\text{S}-\text{P}_2\text{S}_5-\text{P}_2\text{O}_5$ glass-ceramic electrolytes, *J. Power Sources* 146 (2005) 715-718.
- [103] M. Tatsumisago, F. Mizuno, A. Hayashi, All-solid-state lithium secondary batteries using sulfide-based glass-ceramic electrolytes, *J. Power Sources* 159 (2006) 193-199.
- [104] T. Kobayashi, Y. Imade, D. Shishihara, K. Homma, M. Nagao, R. Watanabe, T. Yokoi, A. Yamada, R. Kanno, T. Tatsumi, All solid-state battery with sulfur electrode and thio-LISICON electrolyte, *J. Power Sources* 182 (2008) 621-625.
- [105] T. Inada, T. Kobayashi, N. Sonoyama, A. Yamada, S. Kondo, M. Nagao, R. Kanno, All solid-state sheet battery using lithium inorganic solid electrolyte, thio-LISICON, *J. Power Sources* 194 (2009) 1085-1088.
- [106] M. Nagao, H. Kitaura, A. Hayashi, M. Tatsumisago, Characterization of all-solid-state lithium secondary batteries using $\text{Cu}_x\text{Mo}_6\text{S}_{8-y}$ electrode and $\text{Li}_2\text{S}-\text{P}_2\text{S}_5$ solid electrolyte, *J. Power Sources* 189 (2009) 672-675.
- [107] M. Nagao, A. Hayashi, M. Tatsumisago, Sulfur-carbon composite electrode for all-

- solid-state Li/S battery with Li_2S – P_2S_5 solid electrolyte, *Electrochim. Acta* 56 (2011) 6055-6059.
- [108] N. Kamaya, K. Homma, Y. Yamakawa, M. Hirayama, R. Kanno, M. Yonemura, T. Kamiyama, Y. Kato, S. Hama, K. Kawamoto, A. Mitsui, A lithium superionic conductor, *Nat. Mater.* 10 (2011) 682-686.
- [109] F. Mizuno, All-solid-state lithium secondary batteries using $\text{Li}_2\text{S}\cdot\text{SiS}_2\cdot\text{Li}_4\text{SiO}_4$ glasses and $\text{Li}_2\text{S}\cdot\text{P}_2\text{S}_5$ glass ceramics as SEs, *Solid State Ionics* 175 (2004) 699-702.
- [110] J. Kennedy, Ionically conductive glasses based on SiS_2 , *Mater. Chem. Phys.* 23 (1989) 29-50.
- [111] S. Kondo, K. Takada, Y. Yamamura, New lithium ion conductors based on Li_2S – SiS_2 system, *Solid State Ionics* 53 (1992) 1183-1186.
- [112] H. MORIMOTO, H. YAMASHITA, M. TATSUMISAGO, T. MINAMI, Mechanochemical synthesis of the high lithium ion conductive amorphous materials in the systems Li_2S – SiS_2 and Li_2S – SiS_2 – Li_4SiO_4 , *J. Ceram. Soc. Jpn.* 108 (2000) 128-131.
- [113] H. Morimoto, H. Yamashita, M. Tatsumisago, T. Minami, Mechanochemical synthesis of new amorphous materials of $60\text{Li}_2\text{S}\cdot 40\text{SiS}_2$ with high lithium ion conductivity, *J. Am. Ceram. Soc.* 82 (1999) 1352-1354.
- [114] A. Hayashi, M. Tatsumisago, T. Minami, Y. Miura, Structural investigation of $95(0.6\text{Li}_2\text{S}\cdot 0.4\text{SiS}_2)\cdot 5\text{Li}_4\text{SiO}_4$ oxysulfide glass by using X-ray photoelectron spectroscopy, *J. Am. Ceram. Soc.* 81 (1998) 1305-1309.
- [115] A. Hayashi, M. Tatsumisago, T. Minami, Y. Miura, X-ray photoelectron spectroscopy of $(100-x)(0.6\text{Li}_2\text{S}\cdot 0.4\text{SiS}_2)\cdot x\text{Li}_4\text{SiO}_4$ oxysulphide glasses, *Phys. Chem. Glasses* 39 (1998) 145-150.

- [116] A. Hayashi, R. Araki, R. Komiya, K. Tadanaga, M. Tatsumisago, T. Minami, Thermal and electrical properties of rapidly quenched $\text{Li}_2\text{S-SiS}_2\text{-Li}_2\text{O-P}_2\text{O}_5$ oxysulfide glasses, *Solid State Ionics* 113 (1998) 733-738.
- [117] M. Tatsumisago, K. Hirai, T. Minami, M. Takahashi, Preparation and characterisation of superionic $\text{Li}_2\text{S-SiS}_2\text{-Li}_4\text{GeO}_4$ glasses, *Phys. Chem. Glasses* 38 (1997) 63-65.
- [118] K. Hirai, M. Tatsumisago, M. Takahashi, T. Minami, ^{29}Si and ^{31}P MAS-NMR spectra of $\text{Li}_2\text{S-SiS}_2\text{-Li}_3\text{PO}_4$ rapidly quenched glasses, *J. Am. Ceram. Soc.* 79 (1996) 349-352.
- [119] M. Tatsumisago, K. Hirai, T. Hirata, M. Takahashi, T. Minami, Structure and properties of lithium ion conducting oxysulfide glasses prepared by rapid quenching, *Solid State Ionics* 86 (1996) 487-490.
- [120] A. Hayashi, K. Hirai, M. Tatsumisago, M. Takahashi, T. Minami, Preparation of $\text{Li}_6\text{Si}_2\text{S}_7\text{-Li}_6\text{B}_4\text{X}_9$ ($\text{X}=\text{S}, \text{O}$) glasses by rapid quenching and their lithium ion conductivities, *Solid State Ionics* 86 (1996) 539-542.
- [121] K. Hirai, M. Tatsumisago, T. Minami, Thermal and electrical properties of rapidly quenched glasses in the systems $\text{Li}_2\text{S-SiS}_2\text{-Li}_x\text{MO}_y$ ($\text{Li}_x\text{MO}_y=\text{Li}_4\text{SiO}_4, \text{Li}_2\text{SO}_4$), *Solid State Ionics* 78 (1995) 269-273.
- [122] M. Tatsumisago, K. Hirai, T. Minami, K. Takada, S. KONDO, Superionic conduction in rapidly quenched $\text{Li}_2\text{S-SiS}_2\text{-Li}_3\text{PO}_4$ glasses, *J. Ceram. Soc. Jpn.* 101 (1993) 1315-1317.
- [123] J. Kim, M. Eom, S. Noh, D. Shin, Effect of mixing method on the properties of composite cathodes for all-solid-state lithium batteries using $\text{Li}_2\text{S-P}_2\text{S}_5$ SEs, *J. Power Sources* 244 (2013) 476-481.

- [124] M. Nagao, A. Hayashi, M. Tatsumisago, Electrochemical performance of all-solid-state Li/S batteries with sulfur-based composite electrodes prepared by mechanical milling at high temperature, *Energy Technol.* 1 (2013) 186-192.
- [125] M. Nagao, A. Hayashi, M. Tatsumisago, T. Kanetsuku, T. Tsuda, S. Kuwabata, In situ SEM study of a lithium deposition and dissolution mechanism in a bulk-type solid-state cell with a $\text{Li}_2\text{S}-\text{P}_2\text{S}_5$ solid electrolyte, *Phys. Chem. Chem. Phys.* 15 (2013) 18600-18606.
- [126] S. Noh, J. Kim, M. Eom, D. Shin, Surface modification of LiCoO_2 with $\text{Li}_3\text{xLa}_{2/3-\text{x}}\text{TiO}_3$ for all-solid-state lithium ion batteries using $\text{Li}_2\text{S}-\text{P}_2\text{S}_5$ glass-ceramic, *Ceram. Int.* 39 (2013) 8453-8458.
- [127] T. Ohtomo, A. Hayashi, M. Tatsumisago, Y. Tsuchida, S. Hama, K. Kawamoto, All-solid-state lithium secondary batteries using the $75\text{Li}_2\text{S}\cdot 25\text{P}_2\text{S}_5$ glass and the $70\text{Li}_2\text{S}\cdot 30\text{P}_2\text{S}_5$ glass-ceramic as SEs, *J. Power Sources* 233 (2013) 231-235.
- [128] T. Hakari, M. Nagao, A. Hayashi, M. Tatsumisago, Preparation of composite electrode with $\text{Li}_2\text{S}-\text{P}_2\text{S}_5$ glasses as active materials for all-solid-state lithium secondary batteries, *Solid State Ionics* 262 (2014) 147-150.
- [129] S. Kinoshita, K. Okuda, N. Machida, T. Shigematsu, Additive effect of ionic liquids on the electrochemical property of a sulfur composite electrode for all-solid-state lithium-sulfur battery, *J. Power Sources* 269 (2014) 727-734.
- [130] M. Otoyama, Y. Ito, A. Hayashi, M. Tatsumisago, Raman imaging for LiCoO_2 composite positive electrodes in all-solid-state lithium batteries using $\text{Li}_2\text{S}-\text{P}_2\text{S}_5$ SEs, *J. Power Sources* 302 (2016) 419-425.
- [131] H. Visbal, Y. Aihara, S. Ito, T. Watanabe, Y. Park, S. Doo, The effect of diamond-like carbon coating on $\text{LiNi}_{0.8}\text{Co}_{0.15}\text{Al}_{0.05}\text{O}_2$ particles for all solid-state lithium-ion

- batteries based on Li_2S – P_2S_5 glass-ceramics, *J. Power Sources* 314 (2016) 85-92.
- [132] S. Chida, A. Miura, N.C. Rosero-Navarro, M. Higuchi, N.H. Phuc, H. Muto, A. Matsuda, K. Tadanaga, Liquid-phase synthesis of $\text{Li}_6\text{PS}_5\text{Br}$ using ultrasonication and application to cathode composite electrodes in all-solid-state batteries, *Ceram. Int.* 44 (2018) 742-746.
- [133] Y. Kato, S. Shiotani, K. Morita, K. Suzuki, M. Hirayama, R. Kanno, All-solid-state batteries with thick electrode configurations, *J Phys Chem Lett*, 9 (2018) 607–613.
- [134] Z. Zhang, J.H. Kennedy, Synthesis and characterization of the B_2S_3 · Li_2S , the P_2S_5 · Li_2S and the B_2S_3 · P_2S_5 · Li_2S glass systems, *Solid State Ionics* 38 (1990) 217-224.
- [135] J.H. Kennedy, Z. Zhang, Preparation and electrochemical properties of the SiS_2 – P_2S_5 – Li_2S glass coformer system, *J. Electrochem. Soc.* 136 (1989) 2441-2443.
- [136] A. Hayashi, S. Hama, H. Morimoto, M. Tatsumisago, T. Minami, Preparation of Li_2S – P_2S_5 amorphous SEs by mechanical milling, *J. Am. Ceram. Soc.* 84 (2001) 477-479.
- [137] A. Hayashi, K. Minami, S. Ujiie, M. Tatsumisago, Preparation and ionic conductivity of $\text{Li}_7\text{P}_3\text{S}_{11-z}$ glass-ceramic electrolytes, *J. Non-Cryst. Solids* 356 (2010) 2670-2673.
- [138] K. Minami, F. Mizuno, A. Hayashi, M. Tatsumisago, Lithium ion conductivity of the Li_2S – P_2S_5 glass-based electrolytes prepared by the melt quenching method, *Solid State Ionics* 178 (2007) 837-841.
- [139] F. Mizuno, A. Hayashi, K. Tadanaga, M. Tatsumisago, High lithium ion conducting glass-ceramics in the system Li_2S – P_2S_5 , *Solid State Ionics* 177 (2006) 2721-2725.
- [140] A. Hayashi, S. Hama, T. Minami, M. Tatsumisago, Formation of superionic crystals from mechanically milled Li_2S – P_2S_5 glasses, *Electrochem. Commun.* 5 (2003) 111-

114.

- [141] J. Kim, Y. Yoon, J. Lee, D. Shin, Formation of the high lithium ion conducting phase from mechanically milled amorphous Li_2S – P_2S_5 system, *J. Power Sources* 196 (2011) 6920-6923.
- [142] Y. Seino, T. Ota, K. Takada, A. Hayashi, M. Tatsumisago, A sulphide lithium super ion conductor is superior to liquid ion conductors for use in rechargeable batteries, *Energy Environ. Sci.* 7 (2014) 627-631.
- [143] K. Minami, A. Hayashi, M. Tatsumisago, Crystallization process for superionic $\text{Li}_7\text{P}_3\text{S}_{11}$ glass–ceramic electrolytes, *J. Am. Ceram. Soc.* 94 (2011) 1779-1783.
- [144] R.C. Xu, X.H. Xia, Z.J. Yao, X.L. Wang, C.D. Gu, J.P. Tu, Preparation of $\text{Li}_7\text{P}_3\text{S}_{11}$ glass-ceramic electrolyte by dissolution-evaporation method for all-solid-state lithium ion batteries, *Electrochim. Acta* 219 (2016) 235-240.
- [145] H. Muramatsu, A. Hayashi, T. Ohtomo, S. Hama, M. Tatsumisago, Structural change of Li_2S – P_2S_5 sulfide SEs in the atmosphere, *Solid State Ionics* 182 (2011) 116-119.
- [146] A. Hayashi, H. Muramatsu, T. Ohtomo, S. Hama, M. Tatsumisago, Improved chemical stability and cyclability in Li_2S – P_2S_5 – P_2O_5 – ZnO composite electrolytes for all-solid-state rechargeable lithium batteries, *J. Alloys Compd.* 591 (2014) 247-250.
- [147] K. Minami, A. Hayashi, S. Ujiie, M. Tatsumisago, Electrical and electrochemical properties of glass–ceramic electrolytes in the systems Li_2S – P_2S_5 – P_2S_3 and Li_2S – P_2S_5 – P_2O_5 , *Solid State Ionics* 192 (2011) 122-125.
- [148] J.E. Trevey, Y.S. Jung, S.-H. Lee, Preparation of Li_2S – GeSe_2 – P_2S_5 electrolytes by a single step ball milling for all-solid-state lithium secondary batteries, *J. Power Sources* 195 (2010) 4984-4989.

- [149] J.E. Trevey, J.R. Gilsdorf, S.W. Miller, S.-H. Lee, $\text{Li}_2\text{S}-\text{Li}_2\text{O}-\text{P}_2\text{S}_5$ solid electrolyte for all-solid-state lithium batteries, *Solid State Ionics* 214 (2012) 25-30.
- [150] A. Hayashi, H. Muramatsu, T. Ohtomo, S. Hama, M. Tatsumisago, Improvement of chemical stability of Li_3PS_4 glass electrolytes by adding M_xO_y ($\text{M} = \text{Fe}, \text{Zn}, \text{and Bi}$) nanoparticles, *J. Mater. Chem. A* 1 (2013) 6320-6326.
- [151] A. Yamauchi, A. Sakuda, A. Hayashi, M. Tatsumisago, Preparation and ionic conductivities of $(100-x)(0.75\text{Li}_2\text{S}\cdot 0.25\text{P}_2\text{S}_5)\cdot x\text{LiBH}_4$ glass electrolytes, *J. Power Sources* 244 (2013) 707-710.
- [152] B. Huang, X. Yao, Z. Huang, Y. Guan, Y. Jin, X. Xu, Li_3PO_4 -doped $\text{Li}_7\text{P}_3\text{S}_{11}$ glass-ceramic electrolytes with enhanced lithium ion conductivities and application in all-solid-state batteries, *J. Power Sources* 284 (2015) 206-211.
- [153] P. Lu, F. Ding, Z. Xu, J. Liu, X. Liu, Q. Xu, Study on $(100-x)(70\text{Li}_2\text{S}\cdot 30\text{P}_2\text{S}_5)\cdot x\text{Li}_2\text{ZrO}_3$ glass-ceramic electrolyte for all-solid-state lithium-ion batteries, *J. Power Sources* 356 (2017) 163-171.
- [154] R. Kanno, M. Murayama, T. Inada, T. Kobayashi, K. Sakamoto, N. Sonoyama, A. Yamada, S. Kondo, A self-assembled breathing interface for all-solid-state ceramic lithium batteries, *Electrochem. Solid-State Lett.* 7 (2004) A455- A458.
- [155] T. Matsumura, K. Nakano, R. Kanno, A. Hirano, N. Imanishi, Y. Takeda, Nickel sulfides as a cathode for all-solid-state ceramic lithium batteries, *J. Power Sources* 174 (2007) 632-636.
- [156] T. Kobayashi, A. Yamada, R. Kanno, Interfacial reactions at electrode/electrolyte boundary in all solid-state lithium battery using inorganic solid electrolyte, thio-LISICON, *Electrochim. Acta* 53 (2008) 5045-5050.
- [157] M. Nagao, Y. Imade, H. Narisawa, T. Kobayashi, R. Watanabe, T. Yokoi, T. Tatsumi,

- R. Kanno, All-solid-state Li–sulfur batteries with mesoporous electrode and thio-LISICON solid electrolyte, *J. Power Sources* 222 (2013) 237-242.
- [158] J.M. Whiteley, J.H. Woo, E. Hu, K.W. Nam, S.H. Lee, Empowering the lithium metal battery through a silicon-based superionic conductor, *J. Electrochem. Soc.* 161 (2014) A1812-A1817.
- [159] P. Bron, S. Johansson, K. Zick, J. Schmedt auf der Gunne, S. Dehnen, B. Roling, $\text{Li}_{10}\text{SnP}_2\text{S}_{12}$: an affordable lithium superionic conductor, *J. Am. Chem. Soc.* 135 (2013) 15694-15697.
- [160] K. SUZUKI, D. KATO, K. HARA, T.-a. YANO, M. HIRAYAMA, M. HARA, R. KANNO, Composite sulfur electrode for all-solid-state lithium-sulfur battery with Li_2S - GeS_2 - P_2S_5 -based thio-LISICON solid electrolyte, *Electrochem.* 86 (2018) 1-5.
- [161] R. Kanno, T. Hata, Y. Kawamoto, M. Irie, Synthesis of a new lithium ionic conductor, thio-LISICON–lithium germanium sulfide system, *Solid State Ionics* 130 (2000) 97-104.
- [162] R. Kanno, M. Murayama, Lithium ionic conductor thio-LISICON: the Li_2S - GeS_2 - P_2S_5 system, *J. Electrochem. Soc.* 148 (2001) A742.
- [163] M. Murayama, Synthesis of new lithium ionic conductor thio-LISICON-lithium silicon sulfides system, *J. Solid State Chem.* 168 (2002) 140-148.
- [164] A. Hayashi, Y. Ishikawa, S. Hama, T. Minami, M. Tatsumisago, Fast lithium-ion conducting glass-ceramics in the system Li_2S - SiS_2 - P_2S_5 , *Electrochem. Solid-State Lett.* 6 (2003) A47-A49.
- [165] N. Ohta, K. Takada, M. Osada, L. Zhang, T. Sasaki, M. Watanabe, Solid electrolyte, thio-LISICON, thin film prepared by pulsed laser deposition, *J. Power Sources* 146 (2005) 707-710.

- [166] C. Cao, Z.-B. Li, X.-L. Wang, X.-B. Zhao, W.-Q. Han, Recent advances in inorganic SEs for lithium batteries, *Front. Energy Res.* 2 (2014).
- [167] Y. Mo, S.P. Ong, G. Ceder, First principles study of the $\text{Li}_{10}\text{GeP}_2\text{S}_{12}$ lithium super ionic conductor material, *Chem. Mater.* 24 (2011) 15-17.
- [168] S. Adams, R. Prasada Rao, Structural requirements for fast lithium ion migration in $\text{Li}_{10}\text{GeP}_2\text{S}_{12}$, *J. Mater. Chem.* 22 (2012) 7687-7691.
- [169] S. Ibrahim, M.M. Yassin, R. Ahmad, M.R. Johan, Effects of various LiPF_6 salt concentrations on PEO-based solid polymer electrolytes, *Ionics* 17 (2011) 399-405.
- [170] A. Manuel Stephan, K.S. Nahm, Review on composite polymer electrolytes for lithium batteries, *Polymer* 47 (2006) 5952-5964.
- [171] D. Marmorstein, T. Yu, K. Striebel, F. McLarnon, J. Hou, E. Cairns, Electrochemical performance of lithium/sulfur cells with three different polymer electrolytes, *J. Power Sources* 89 (2000) 219-226.
- [172] C.-W. Park, H.-S. Ryu, K.-W. Kim, B.-Y. Hur, K.-K. Cho, J.-H. Ahn, J.-Y. Lee, H.-J. Ahn, Effect of sulfur electrode composition on the electrochemical property of lithium/PEO/sulfur battery, *Met. Mater. Int.* 10 (2004) 375-379.
- [173] H. Marceau, C.-S. Kim, A. Paoletta, S. Ladouceur, M. Lagacé, M. Chaker, A. Vijn, A. Guerfi, C.M. Julien, A. Mauger, M. Armand, P. Hovington, K. Zaghib, In operando scanning electron microscopy and ultraviolet–visible spectroscopy studies of lithium/sulfur cells using all solid-state polymer electrolyte, *J. Power Sources* 319 (2016) 247-254.
- [174] G.B. Appetecchi, J. Hassoun, B. Scrosati, F. Croce, F. Cassel, M. Salomon, Hot-pressed, solvent-free, nanocomposite, PEO-based electrolyte membranes, *J. Power Sources* 124 (2003) 246-253.

- [175] C. Chiang, G. Davis, C. Harding, T. Takahashi, Polymeric electrolyte based on poly (ethylene imine) and lithium salts, *Solid State Ionics* 18 (1986) 300-305.
- [176] K.G. Ishmukhametova, O.V. Yarmolenko, L.M. Bogdanova, B.A. Rozenberg, O.N. Efimov, New solid polymer electrolytes based on polyester diacrylate for lithium power sources, *Russ. J. Electrochem.* 45 (2009) 558-563.
- [177] X. Yang, F. Zhang, L. Zhang, T. Zhang, Y. Huang, Y. Chen, A high-performance graphene oxide-doped ion gel as gel polymer electrolyte for all-solid-state supercapacitor applications, *Adv. Funct. Mater.* 23 (2013) 3353-3360.
- [178] J. Zhang, J. Zhao, L. Yue, Q. Wang, J. Chai, Z. Liu, X. Zhou, H. Li, Y. Guo, G. Cui, L. Chen, Safety-reinforced poly(propylene carbonate)-based all-solid-state polymer electrolyte for ambient-temperature solid polymer lithium batteries, *Adv. Energy Mater.* 5 (2015) 1501082.
- [179] X. Ban, W. Zhang, N. Chen, C. Sun, A high-performance and durable poly (ethylene oxide)-based composite solid electrolyte for all solid-state lithium battery, *J. Phys. Chem. C* 122 (2018) 9852-9858.
- [180] Z. Zhang, D. Sherlock, R. West, R. West, K. Amine, L.J. Lyons, Cross-linked network polymer electrolytes based on a polysiloxane backbone with oligo (oxyethylene) side chains: synthesis and conductivity, *Macromolecules* 36 (2003) 9176-9180.
- [181] S. Liang, U.H. Choi, W. Liu, J. Runt, R.H. Colby, Synthesis and lithium ion conduction of polysiloxane single-ion conductors containing novel weak-binding borates, *Chem. Mater.* 24 (2012) 2316-2323.
- [182] U.H. Choi, S. Liang, M.V. O'Reilly, K.I. Winey, J. Runt, R.H. Colby, Influence of solvating plasticizer on ion conduction of polysiloxane single-ion conductors,

- Macromolecules 47 (2014) 3145-3153.
- [183] L. Porcarelli, A.S. Shaplov, M. Salsamendi, J.R. Nair, Y.S. Vygodskii, D. Mecerreyes, C. Gerbaldi, Single-ion block copoly (ionic liquid) s as electrolytes for all-solid state lithium batteries, *ACS Appl. Mater. Interfaces* 8 (2016) 10350-10359.
- [184] C.P. Fonseca, S. Neves, Characterization of polymer electrolytes based on poly (dimethyl siloxane-co-ethylene oxide), *J. Power Sources* 104 (2002) 85-89.
- [185] D. Fenton, J. Parker, P. Wright, Complexes of alkali metal ions with poly (ethylene oxide), *polymer* 14 (1973) 589.
- [186] C. Berthier, W. Gorecki, M. Minier, M. Armand, J. Chabagno, P. Rigaud, Microscopic investigation of ionic conductivity in alkali metal salts-poly (ethylene oxide) adducts, *Solid State Ionics* 11 (1983) 91-95.
- [187] M. Ratner, J. MacCallum, C. Vincent, *Polymer electrolyte reviews*, Elsevier, London, (1987) 173-236.
- [188] R. Tanaka, M. Sakurai, H. Sekiguchi, H. Mori, T. Murayama, T. Ooyama, Lithium ion conductivity in polyoxyethylene/polyethylenimine blends, *Electrochim. Acta* 46 (2001) 1709-1715.
- [189] P.V. Wright, Polymer electrolytes-the early days, *Electrochim. Acta* 43 (1998) 1137-1143.
- [190] J.-H. Shin, W.A. Henderson, S. Scaccia, P.P. Prosini, S. Passerini, Solid-state Li/LiFePO₄ polymer electrolyte batteries incorporating an ionic liquid cycled at 40°C, *J. Power Sources* 156 (2006) 560-566.
- [191] H.-M. Xiong, Z.-D. Wang, D.-P. Xie, L. Cheng, Y.-Y. Xia, Stable polymer electrolytes based on polyether-grafted ZnO nanoparticles for all-solid-state lithium batteries, *J. Mater. Chem.* 16 (2006) 1345-1349.

- [192] Y. Masuda, M. Nakayama, M. Wakihara, Fabrication of all solid-state lithium polymer secondary batteries using PEG-borate/aluminate ester as plasticizer for polymer electrolyte, *Solid State Ionics* 178 (2007) 981-986.
- [193] H. Nakano, K. Dokko, J.-i. Sugaya, T. Yasukawa, T. Matsue, K. Kanamura, All-solid-state micro lithium-ion batteries fabricated by using dry polymer electrolyte with micro-phase separation structure, *Electrochem. Commun.* 9 (2007) 2013-2017.
- [194] M. Nakayama, S. Wada, S. Kuroki, M. Nogami, Factors affecting cyclic durability of all-solid-state lithium polymer batteries using poly(ethylene oxide)-based solid polymer electrolytes, *Energy Environ. Sci.* 3 (2010) 1995-2002.
- [195] X. Liang, Z. Wen, Y. Liu, H. Zhang, L. Huang, J. Jin, Highly dispersed sulfur in ordered mesoporous carbon sphere as a composite cathode for rechargeable polymer Li/S battery, *J. Power Sources* 196 (2011) 3655-3658.
- [196] F. Yuan, H.-Z. Chen, H.-Y. Yang, H.-Y. Li, M. Wang, PAN-PEO solid polymer electrolytes with high ionic conductivity, *Mater. Chem. Phys.* 89 (2005) 390-394.
- [197] J. Zhang, L. Yue, P. Hu, Z. Liu, B. Qin, B. Zhang, Q. Wang, G. Ding, C. Zhang, X. Zhou, J. Yao, G. Cui, L. Chen, Taichi-inspired rigid-flexible coupling cellulose-supported solid polymer electrolyte for high-performance lithium batteries, *Sci. Rep.* 4 (2014) 6272.
- [198] C. Gerbaldi, J.R. Nair, M.A. Kulandainathan, R.S. Kumar, C. Ferrara, P. Mustarelli, A.M. Stephan, Innovative high performing metal organic framework (MOF)-laden nanocomposite polymer electrolytes for all-solid-state lithium batteries, *J. Mater. Chem. A* 2 (2014) 9948-9954.
- [199] T. Uno, S. Kawaguchi, M. Kubo, T. Itoh, Ionic conductivity and thermal property of solid hybrid polymer electrolyte composed of oligo(ethylene oxide) unit and

- butyrolactone unit, *J. Power Sources* 178 (2008) 716-722.
- [200] S.-J. Kwon, D.-G. Kim, J. Shim, J.H. Lee, J.-H. Baik, J.-C. Lee, Preparation of organic/inorganic hybrid semi-interpenetrating network polymer electrolytes based on poly(ethylene oxide-co-ethylene carbonate) for all-solid-state lithium batteries at elevated temperatures, *Polymer* 55 (2014) 2799-2808.
- [201] H. Zeng, X. Ji, F. Tsai, Q. Zhang, T. Jiang, R.K. Li, H. Shi, S. Luan, D. Shi, Enhanced cycling performance for all-solid-state lithium ion battery with LiFePO_4 composite cathode encapsulated by poly (ethylene glycol)(PEG) based polymer electrolyte, *Solid State Ionics* 320 (2018) 92-99.
- [202] J. Mindemark, M.J. Lacey, T. Bowden, D. Brandell, Beyond PEO-Alternative host materials for Li^+ -conducting solid polymer electrolytes, *Prog. Polym. Sci.* 81 (2018) 114-143.
- [203] Z. Bakenov, M. Nakayama, M. Wakihara, I. Taniguchi, Lithium AlPO_4 composite polymer battery with nanostructured LiMn_2O_4 cathode, *J. Solid State Electrochem.* 12 (2007) 295-302.
- [204] H. Duan, Y.-X. Yin, X.-X. Zeng, J.-Y. Li, J.-L. Shi, Y. Shi, R. Wen, Y.-G. Guo, L.-J. Wan, In-situ plasticized polymer electrolyte with double-network for flexible solid-state lithium-metal batteries, *Energy Storage Mater.* 10 (2018) 85-91.
- [205] B. Sun, J. Mindemark, K. Edström, D. Brandell, Polycarbonate-based solid polymer electrolytes for Li-ion batteries, *Solid State Ionics* 262 (2014) 738-742.
- [206] Y. Tominaga, K. Yamazaki, Fast Li-ion conduction in poly (ethylene carbonate)-based electrolytes and composites filled with TiO_2 nanoparticles, *Chem Commun.* 50 (2014) 4448-4450.
- [207] Y. Kang, J. Lee, D.H. Suh, C. Lee, A new polysiloxane based cross-linker for solid

- polymer electrolyte, *J. Power Sources* 146 (2005) 391-396.
- [208] Y. Lin, J. Li, Y. Lai, C. Yuan, Y. Cheng, J. Liu, A wider temperature range polymer electrolyte for all-solid-state lithium ion batteries, *RSC Adv.* 3 (2013) 10722-10730.
- [209] H.-J. Ha, Y.H. Kwon, J.Y. Kim, S.-Y. Lee, A self-standing, UV-cured polymer networks-reinforced plastic crystal composite electrolyte for a lithium-ion battery, *Electrochim. Acta* 57 (2011) 40-45.
- [210] H.-J. Ha, E.-H. Kil, Y.H. Kwon, J.Y. Kim, C.K. Lee, S.-Y. Lee, UV-curable semi-interpenetrating polymer network-integrated, highly bendable plastic crystal composite electrolytes for shape-conformable all-solid-state lithium ion batteries, *Energy Environ. Sci.* 5 (2012) 6491-6499.
- [211] H. Zhang, C. Li, M. Piszcz, E. Coya, T. Rojo, L.M. Rodriguez-Martinez, M. Armand, Z. Zhou, Single lithium-ion conducting solid polymer electrolytes: advances and perspectives, *Chem. Soc. Rev.* 46 (2017) 797-815.
- [212] C. Cao, Y. Li, Y. Feng, P. Long, H. An, C. Qin, J. Han, S. Li, W. Feng, A sulfonimide-based alternating copolymer as a single-ion polymer electrolyte for high-performance lithium-ion batteries, *J. Mater. Chem. A* 5 (2017) 22519-22526.
- [213] R. Bouchet, S. Maria, R. Meziane, A. Aboulaich, L. Lienafa, J.-P. Bonnet, T.N. Phan, D. Bertin, D. Gigmes, D. Devaux, Single-ion BAB triblock copolymers as highly efficient electrolytes for lithium-metal batteries, *Nat. Mater.* 12 (2013) 452-457.
- [214] L. Porcarelli, A.S. Shaplov, F. Bella, J.R. Nair, D. Mecerreyes, C. Gerbaldi, Single-ion conducting polymer electrolytes for lithium metal polymer batteries that operate at ambient temperature, *ACS Energy Lett.* 1 (2016) 678-682.
- [215] W. Qian, J. Texter, F. Yan, *Frontiers in poly(ionic liquid)s: syntheses and applications*, *Chem. Soc. Rev.* 46 (2017) 1124-1159.

- [216] X. Wang, H. Zhu, G.M. Girard, R. Yunis, D.R. MacFarlane, D. Mecerreyes, A.J. Bhattacharyya, P.C. Howlett, M. Forsyth, Preparation and characterization of gel polymer electrolytes using poly (ionic liquids) and high lithium salt concentration ionic liquids, *J. Mater. Chem. A* 5 (2017) 23844-23852.
- [217] E. Quartarone, P. Mustarelli, A. Magistris, PEO-based composite polymer electrolytes, *Solid State Ionics* 110 (1998) 1-14.
- [218] G. Appetecchi, S. Passerini, PEO-carbon composite lithium polymer electrolyte, *Electrochim. Acta* 45 (2000) 2139-2145.
- [219] M. Michael, M. Jacob, S. Prabakaran, S. Radhakrishna, Enhanced lithium ion transport in PEO-based solid polymer electrolytes employing a novel class of plasticizers, *Solid State Ionics* 98 (1997) 167-174.
- [220] S. Slane, M. Salomon, Composite gel electrolyte for rechargeable lithium batteries, *J. Power Sources* 55 (1995) 7-10.
- [221] N. Rippaus, B. Stiaszny, S.J. Sedlmaier, H. Beyer, H.A. Gasteiger, Understanding chemical stability issues between different SEs in all-solid-state batteries, in: *Meeting Abstracts, The Electrochemical Society* 2018, 488-488.
- [222] P. Bashiri, G.A. Nazri, V. Naik, R. Naik, Conformal solid state $\text{Li}_7\text{La}_3\text{Zr}_2\text{O}_{12}$ -PEO- LiClO_4 composite electrolyte for advanced lithium batteries, *Bull. Am. Phys. Soc.* 63 (2018).
- [223] M.-S. Park, Y.-C. Jung, D.-W. Kim, Hybrid SEs composed of poly (1, 4-butylene adipate) and lithium aluminum germanium phosphate for all-solid-state $\text{Li}/\text{LiNi}_{0.6}\text{Co}_{0.2}\text{Mn}_{0.2}\text{O}_2$ cells, *Solid State Ionics* 315 (2018) 65-70.
- [224] S. Zekoll, C. Marriner-Edwards, A.O. Hekselman, J. Kasemchainan, C. Kuss, D.E. Armstrong, D. Cai, R.J. Wallace, F.H. Richter, J.H. Thijssen, Hybrid electrolytes with

- 3D bicontinuous ordered ceramic and polymer microchannels for all-solid-state batteries, *Energy Environ. Sci.* 11 (2018) 185-201.
- [225] J. Hassoun, B. Scrosati, Moving to a solid-state configuration: a valid approach to making lithium-sulfur batteries viable for practical applications, *Adv. Mater.* 22 (2010) 5198-5201.
- [226] J. Xi, X. Tang, Nanocomposite polymer electrolyte based on Poly(ethylene oxide) and solid super acid for lithium polymer battery, *Chem. Phys. Lett.* 393 (2004) 271-276.
- [227] F. Croce, G. Appetecchi, L. Persi, B. Scrosati, Nanocomposite polymer electrolytes for lithium batteries, *Nature* 394 (1998) 456.
- [228] L. Wang, X. Li, W. Yang, Enhancement of electrochemical properties of hot-pressed poly(ethylene oxide)-based nanocomposite polymer electrolyte films for all-solid-state lithium polymer batteries, *Electrochim. Acta* 55 (2010) 1895-1899.
- [229] D. Lin, W. Liu, Y. Liu, H.R. Lee, P.C. Hsu, K. Liu, Y. Cui, High ionic conductivity of composite solid polymer electrolyte via in situ synthesis of monodispersed SiO₂ nanospheres in poly(ethylene oxide), *Nano Lett.* 16 (2016) 459-465.
- [230] X. Yu, J. Xie, J. Yang, K. Wang, All solid-state rechargeable lithium cells based on nano-sulfur composite cathodes, *J. Power Sources* 132 (2004) 181-186.
- [231] S.-W. Baek, I. Honma, J. Kim, D. Rangappa, Solidified inorganic-organic hybrid electrolyte for all solid state flexible lithium battery, *J. Power Sources* 343 (2017) 22-29.
- [232] H.Y. Sun, Enhanced lithium-ion transport in PEO-Based composite polymer electrolytes with ferroelectric BaTiO₃, *J. Electrochem. Soc.* 146 (1999) 1672-1676.
- [233] H. Sun, Y. Takeda, N. Imanishi, O. Yamamoto, H.J. Sohn, Ferroelectric materials

- as a ceramic filler in solid composite polyethylene Oxide-Based electrolytes, *J. Electrochem. Soc.* 147 (2000) 2462-2467.
- [234] M. Moreno, R. Quijada, M.A. Santa Ana, E. Benavente, P. Gomez-Romero, G. González, Electrical and mechanical properties of poly(ethylene oxide)/intercalated clay polymer electrolyte, *Electrochim. Acta* 58 (2011) 112-118.
- [235] R. Prasanth, N. Shubha, H.H. Hng, M. Srinivasan, Effect of nano-clay on ionic conductivity and electrochemical properties of poly(vinylidene fluoride) based nanocomposite porous polymer membranes and their application as polymer electrolyte in lithium ion batteries, *Eur. Polym. J.* 49 (2013) 307-318.
- [236] Y. Zhang, Y. Zhao, D. Gosselink, P. Chen, Synthesis of poly(ethylene-oxide)/nanoclay solid polymer electrolyte for all solid-state lithium/sulfur battery, *Ionics* 21 (2014) 381-385.
- [237] C. Tang, K. Hackenberg, Q. Fu, P.M. Ajayan, H. Ardebili, High ion conducting polymer nanocomposite electrolytes using hybrid nanofillers, *Nano Lett.* 12 (2012) 1152-1156.
- [238] F. Croce, F. Bonino, S. Panero, B. Scrosati, Properties of mixed polymer and crystalline ionic conductors, *Philos. Mag. B* 59 (1989) 161-168.
- [239] B. Kumar, L.G. Scanlon, Polymer-ceramic composite electrolytes, *J. Power Sources* 52 (1994) 261-268.
- [240] H.J. Walls, M.W. Riley, R.R. Singhal, R.J. Spontak, P.S. Fedkiw, S.A. Khan, Nanocomposite electrolytes with fumed silica and hectorite clay networks: passive versus active fillers, *Adv. Funct. Mater.* 13 (2003) 710-717.
- [241] M.M. Doeff, J.S. Reed, Li ion conductors based on laponite/poly (ethylene oxide) composites, *Solid State Ionics* 113 (1998) 109-115.

- [242] H.W. Chen, F.C. Chang, Interaction mechanism of a novel polymer electrolyte composed of poly (acrylonitrile), lithium triflate, and mineral clay, *J. Polym. Sci., Part B: Polym. Phys.* 39 (2001) 2407-2419.
- [243] C. Wang, Y. Yang, X. Liu, H. Zhong, H. Xu, Z. Xu, H. Shao, F. Ding, Suppression of lithium dendrite formation by using LAGP-PEO (LiTFSI) composite solid electrolyte and lithium metal anode modified by PEO (LiTFSI) in all-solid-state lithium batteries, *ACS Appl. Mater. Interfaces* 9 (2017) 13694-13702.

Chapter 2 Experimental

2.1 Chemical reagents

Table 2.1 Chemical reagents used in this study.

Chemical reagents	Grade	Producer
Lithium Sulfide Li_2S	99.98%	SIGMA-ALDRICH
Phosphorus Pentasulfide P_2S_5	99.0%	SIGMA-ALDRICH
Selenium Sulfide SeS_2	--	SIGMA-ALDRICH
Graphite	99.0%	NACALAI TESQUE INC.
Sodium Nitrate NaNO_3	99.0%	KANTO CHEMICAL CO., INC.
Sulfuric Acid H_2SO_4	95.0%	WAKO
Potassium Permanganate KMnO_4	99.3%	WAKO
Hydrogen Peroxide H_2O_2	30.0%	WAKO
Sulfur S	98.0%	WAKO

Nickel Chloride Hexahydrate	98.0%	WAKO
$\text{NiCl}_2 \cdot 6\text{H}_2\text{O}$		
Hexamethylenetetramine	$\geq 99.0\%$	SIGMA-ALDRICH
(HMT)		
Disodium Hydrogenphosphate	99.5%	WAKO
$(\text{Na}_2\text{HPO}_4)$		
Ammonia Solution	28.0%-30.0%	WAKO
$\text{NH}_3 \cdot \text{H}_2\text{O}$		
Hydrochloric Acid	35.0%-37.0%	WAKO
HCl		
Poly (ethylene oxide)	--	SIGMA-ALDRICH
PEO (MW = 6×10^5)		
Lithium Bis(trifluoromethanesulfonyl)imide	$>98.0\%$	TCI
LiTFSI		
Lithium Iron(II) Phosphate	--	LIZHIYUAN
LiFePO_4		CHINA
Super P	99.0+%	ALFA AESAR
Polyvinylidene fluoride	--	MTI CORP
(PVDF)		
N-methyl-2-pyrrolidone	99.5%	SIGMA-ALDRICH
(NMP)		
		THE HONJO
Li foil	--	CHEMICAL
		CORPORATION

Zinc Sulfate Heptahydrate ($\text{ZnSO}_4 \cdot 7\text{H}_2\text{O}$)	99.5%	WAKO
Polyethylene glycol-300 (PEG 300)	--	WAKO
Sodium Tetraborate Decahydrate ($\text{Na}_2\text{B}_4\text{O}_7 \cdot 10\text{H}_2\text{O}$)	99.5%-101.0%	WAKO
Ethanol	99.5%	WAKO

2.2 Performance evaluation

The ionic conductivity of the SEs was determined by measuring the EIS (1 MHz to 10 Hz) of blocking batteries. The lithium stability and Li^+ transference number of Li/SEs/Li symmetric batteries were evaluated by periodically charging-discharging and direct current (DC) polarization method combined with the EIS. The electrochemical stability window of the SEs was determined by a linear sweep voltammetry (LSV) and cyclic voltammogram (CV) performed on a working electrode of stainless steel and a counter electrode of lithium metal foil. The battery performances of the SSLBs were investigated by galvanostatic charge and discharge testing.

2.3 Characterization

2.3.1 X-Ray Diffraction (XRD)

The phase composition of the material was characterized by XRD (Rigaku Smartlab, Japan) with Cu $\text{K}\alpha$ radiation ($\lambda = 1.5406 \text{ \AA}$) in a 2θ range from 10° to 90° , and the scanning rate of $10^\circ \cdot \text{min}^{-1}$. Phase identification was achieved through comparison of obtained XRD patterns to those of “Joint Committee on Powder Diffraction Standards

(JCPDS)".

2.3.2 Scanning Electron Microscopy (SEM) and Energy Dispersive X-Ray Spectrometer (EDS)

The microstructure and element analysis were performed on SEM coupled to an EDS (SU8010, Hitachi, Japan).

2.3.3 Transmission Electron Microscopy (TEM)

Images from TEM were obtained on a JEM-2100F transmission electron microscope. Samples for TEM were prepared by sonicating small amounts of the powder in the ethanol for a few minutes and then depositing a few drops of the suspension on a holey copper grid.

2.3.4 Differential Scanning Calorimetry (DSC)

DSC was performed for the obtained powder samples sealed in an Al pan in a dry Ar-filled glove box using a thermal analyzer (Shimadzu, DSC6200) at the scanning rate of $10\text{ }^{\circ}\text{C}\cdot\text{min}^{-1}$.

2.3.5 Thermogravimetric (TG)

TG was carried out using a TA machine (TA-60WS, SHIMADZU, Japan) with a heating rate of $10\text{ }^{\circ}\text{C}\cdot\text{min}^{-1}$ under N_2 atmosphere.

2.3.6 Fourier transform infrared spectrum (FT-IR)

FT-IR spectroscopy was performed to determine chemical structures in the sample in the wave number ranging from 4000 to 400 cm^{-1} (FT/IR-4200, JASCO, Japan).

2.3.7 Raman

Raman spectra were measured using a Raman spectrometer (Jasco, NRS-5100) with 532.1 nm laser.

2.3.8 Electrochemical Measurement

The electrochemical performances were measurement by using the electrochemical

impedance spectroscopy (EIS), direct current (DC) polarization, linear sweep voltammetry (LSV) and cyclic voltammogram (CV) (VersaSTAT 4, Princeton Applied Research, USA).

2.3.9 Charge and Discharge Measurement

Galvanostatic charge and discharge performances of the SSLBs were investigated using battery testing workstation (HOKUTO DENKO HJ1020mSD8, Japan) and LANHE CT2001A charge/discharge system (Wuhan LAND Electronics Co., Ltd.).

Chapter 3 Novel SeS₂ doped Li₂S–P₂S₅ solid electrolyte with high ionic conductivity for all-solid-state lithium sulfur batteries

3.1 Introduction

Lithium ion (Li⁺) batteries are widely used as power sources for various portable devices because of their high operating voltage, high energy density, light weight, and long cycle life [1-7]. However, the safety improvement is still required due to the usage of flammable liquid electrolytes. Recently, development of safely nonflammable SEs to fabricate solid-state batteries (SSBs) is considered to be the best way [8-18]. Recently, the sulfide-based Li₂S–P₂S₅ (LPS) glass-ceramic electrolyte with a molar ratio of 70Li₂S:30P₂S₅ has been found to have superior properties such as high lithium ion conductivity over $1 \times 10^{-3} \text{ S} \cdot \text{cm}^{-1}$ at room temperature and wide electrochemical window up to 5 V vs. Li/Li⁺ [19, 20]. For instance, LPS electrolyte prepared by the heat treatment of the mechanically milled 70Li₂S·30P₂S₅ glass exhibited a Li⁺ ionic conductivity as high as $3.2 \times 10^{-3} \text{ S} \cdot \text{cm}^{-1}$ at room temperature [21]. LPS electrolyte have been used in all-solid-state lithium sulfur batteries (ASSLSBs), however, the relatively lower Li⁺ ionic conductivity than the liquid electrolytes, poor stability and low cycle performance in the battery hinder their large-scale applications [22]. Moreover, the high interfacial resistance and the formation of interphase layers between the electrolyte and electrode should be also avoided [23-28].

Doping other materials to substitute P₂S₅ in LPS is an effective way in enhancing its conductivity and stability. For instances, Xu *et al.* doped MoS₂ in LPS glass-ceramic

electrolyte by a facile high-energy ball milling followed with an annealing way. As a result, the obtained $\text{Li}_2\text{S-P}_2\text{S}_5\text{-MoS}_2$ exhibits a high ionic conductivity of $4.8 \times 10^{-3} \text{ S} \cdot \text{cm}^{-1}$ at room temperature [29]. Other materials such as Li_2O was also used for such a doping to improve the stability and the Li^+ ionic conductivity of LPS [30]. In general, doping other elements in the sulfide electrolytes can expand Li^+ ion transport pathways to increase the conductivity. Furthermore, it could reduce the interfacial resistance and grain boundary effects to improve the electrical and electrochemical properties of solid electrolyte [31, 32]. Recently, it is reported that heterocyclic selenium–sulfur molecules (Se_xS_y) have high stability and compatibility with other sulfides [33-35], which could be doped in the LPS glass-ceramic electrolyte to improve its performance.

In this work, SeS_2 was selected to be doped into LPS glass-ceramic electrolyte ($\text{Li}_2\text{S-P}_2\text{S}_5\text{-SeS}_2$) via a high-energy ball milling combined annealing way in order to enhance the ionic conductivity and stability. The effects of doping amount on the crystal structure, the ionic conductivity and chemical stability versus lithium metal of the obtained $\text{Li}_2\text{S-P}_2\text{S}_5\text{-SeS}_2$ glass-ceramics were investigated systematically by experiments and first-principle calculations based on density functional theory (DFT). Furthermore, the solid-state batteries based on this $\text{Li}_2\text{S-P}_2\text{S}_5\text{-SeS}_2$ glass-ceramic and sulfur-reduced graphene oxide (S-rGO) was fabricated and tested. It is expected to provide a novel solid electrolyte for high performance solid-state batteries.

3.2 Experimental

3.2.1 Solid electrolyte synthesis

$70\text{Li}_2\text{S} \cdot (30-x)\text{P}_2\text{S}_5 \cdot x\text{SeS}_2$ (LPS, $x=0, 0.3, 0.5, 1, 3, 5$) solid electrolyte was prepared by high energy ball milling of Li_2S , P_2S_5 , and SeS_2 powders followed by a heat treatment process. The powder mixture was sealed in a hardened agate pot (45 cm^3) with 10 agate balls (10 mm in diameter) in a glove box with Argon (Ar) gas atmosphere. The ball milling was performed under a rotating speed of 510 rpm for 30 h at room temperature in a planetary ball mill apparatus (Fritsch Pulverisette 7). Then, the powder mixture was heated in Ar atmosphere at 260-280 °C for 4 h to obtain the $70\text{Li}_2\text{S} \cdot 30-x\text{P}_2\text{S}_5 \cdot x\text{SeS}_2$ glass-ceramic solid electrolyte.

3.2.2 Cathode materials synthesis

The other nanocomposite as cathode material was synthesized as follows: firstly, Graphene oxide (GO) was synthesized by oxidation and exfoliation of a natural graphite according to a modified Hummer's method, as described elsewhere [36]; Then, reduced graphene oxides (rGO) were prepared by pyrolysis of GO in a quartz tube furnace at 420 °C for 2 h and 750 °C for 1 h with the protection of high pure N_2 ; thereafter, to form the S-rGO nanocomposite, sulfur and rGO were mixed in water with a weight ratio of $\text{S:rGO} = 3:1$ by ultrasonic method, dried and milled with a rotation speed of 370 rpm for 30 h; finally, the mixture of S-rGO and LPS solid electrolyte with a weight ratio of $\text{S-rGO:LPS}=1:4$ was milled with a rotation speed of 370 rpm for 60 h at room temperature to obtain the $\text{S-}70\text{Li}_2\text{S} \cdot (30-x)\text{P}_2\text{S}_5 \cdot x\text{SeS}_2\text{-rGO}$ nanocomposites.

3.2.3 Characterizations

The phase composition of the cathode material was characterized by X-ray powder diffraction (XRD) (Rigaku Smartlab, Japan) with Cu K α radiation ($\lambda=1.54178$ Å) at a voltage of 15 kV. The unit cell dimensions were refined on *FullProf* software program. Pseudo-Voigt (*pV*) function was selected to refine peak profile. The Rietveld refinements included the following items: (i) background; (ii) scale factors; (iii) global instrumental parameters; (iv) lattice parameters; (v) profile parameters; and (vi) asymmetry parameters. Differential scanning calorimetry (DSC) was performed for the obtained powder samples sealed in an Al pan in a dry Ar-filled glove box using a thermal analyzer (Shimazu, DSC6200) at the scanning rate of 10 °C·min⁻¹. Raman spectra were measured using a Raman spectrometer (Jasco, NRS-5100) with 532.1 nm laser. Meanwhile, microstructure and element analysis were performed on scanning electron microscope (SEM) coupled to an energy dispersive X-Ray spectrometer (EDS) (SU8010, Hitachi, Japan).

3.2.4 Electrochemical performance measurements

The ionic conductivity of the SEs was determined by measuring the electrochemical impedance spectra (EIS) (1 MHz to 10 Hz) of an electron-blocking indium(In)/solid electrolyte/In battery cell, which was fabricated by sandwiching 100 mg solid electrolyte powder between two current collectors of In foil with a diameter of 12 mm by a cold-pressing process with a pressure of 380 MPa. Meanwhile, Li/solid electrolyte/Li and Li/solid electrolyte/stainless steel battery cells were also fabricated by the cold-pressing process for chronoamperometry test and cyclic voltammogram (CV) measurement, respectively. Here, the chronoamperometry test was performed with a constant voltage of

1 V at 30 °C while the CV measurement was carried out at a scan rate of 1 mV·s⁻¹ between -0.5 and 5 V at 30 °C. The electrochemical performance of Li/solid electrolyte/Li symmetric batteries were evaluated by periodically charging-discharging. EIS measurements of the ASSLSBs were performed from 10 Hz to 1 MHz.

3.2.5 All-solid-state Li-S batteries assembling and test

The ASSLSBs were assembled with the prepared cathode (S-70Li₂S·(30-x)P₂S₅·xSeS₂-rGO) and electrolyte (70Li₂S·(30-x)P₂S₅·xSeS₂) materials and Li foil anode in a dry Ar-filled glovebox. Firstly, 100 mg of the solid electrolyte was cold-pressed into a pellet with a diameter of 12 mm at a pressure of 380 MPa (Thickness: 0.5 mm). Then, the cathode material was carefully spread on the one side of the solid electrolyte pellet and pressed under 380 MPa. Finally, a 100 μm thick lithium metal was attached on the other side of the solid electrolyte pellet as the anode electrode by pressing under a pressure of 120 MPa. The detailed battery configuration is shown in Figure 3.1. The obtained ASSLSB was set in a Thermostat with a temperature of 30 °C for charge/discharge performance test using a battery testing workstation (HOKUTO DENKO HJ1020mSD8, Japan). Here, the calculation of specific charge/discharge capacity was based on the mass of sulfur. Meanwhile, the electrochemical impedance spectrum and cyclic voltammogram were measured on an electrochemistry workstation (Princeton Applied Research, VersaSTAT 4, USA).

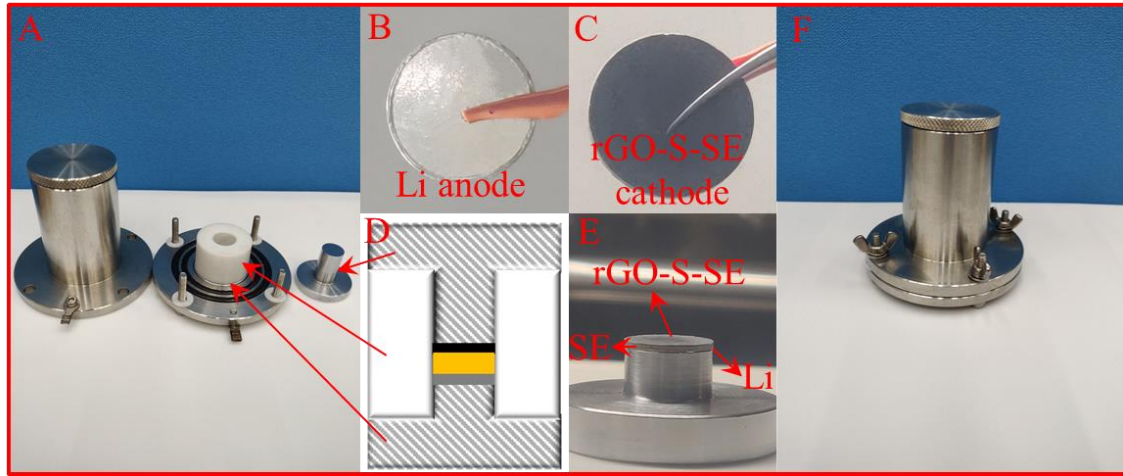


Figure 3.1 Optical image of (A) the disassembling of battery equipment, (B) Li anode, (C) rGO-S-SE cathode, (D) the schematic diagram and (E) the side view of rGO-S/SE/Li battery, and (F) the whole of battery equipment.

3.2.6 Computational details

All calculations in this work were performed by using density functional theory of plane wave pseudopotential calculation program-Cambridge Serial Total Energy Package (CASTEP), and the generalized gradient approximation (GGA) with the Perdew-Burke-Ernzerh function (PBE) was used to describe the exchange correlation energy of the system. An energy cutoff of 300 eV and $1 \times 2 \times 1$ k-point Monkhorst-Pack grid were used. In the process of geometric optimization, the same convergence accuracy and maximum stress were set at values less than 1×10^{-5} eV/atom and below 0.05 GPa, respectively. For the convenience of building $\text{Li}_7\text{P}_3\text{S}_{11}$ model structure, supercells containing PS_4 tetrahedra and P_2S_7 ditetrahedra of $\text{Li}_7\text{P}_3\text{S}_{11}$ are used to simulate SeS2 doped $\text{Li}_7\text{P}_3\text{S}_{11}$ system. P atoms in the supercell are replaced by Se atoms. The extra Li atoms are added to the supercell to maintain electronic neutrality.

3.3 Results and discussion

Figure 3.2 shows the effect of doping amount of SeS₂ in the LPS glass ceramics on the ionic conductivity. One can see that the ionic conductivity increases with the increase in the doping amount from x=0.3 to 1 at first and then, decreases with the further increase in the doping amount. As a result, the ionic conductivities of the 70Li₂S·29.7P₂S₅·0.3SeS₂, 70Li₂S·29.5P₂S₅·0.5SeS₂, 70Li₂S·29P₂S₅·1SeS₂, 70Li₂S·27P₂S₅·3SeS₂, and 70Li₂S·25P₂S₅·5SeS₂ are 3.16×10^{-3} , 4.20×10^{-3} , 5.48×10^{-3} , 3.01×10^{-4} , and 1.35×10^{-5} S·cm⁻¹ at 30 °C, respectively, and the highest conductivity (5.48×10^{-3} S·cm⁻¹) at the composition of x=1 (70Li₂S·29P₂S₅·1SeS₂) is obtained. For comparison, the ionic conductivity of the original 70Li₂S·30P₂S₅ prepared in this study is about 2.53×10^{-3} S·cm⁻¹ at 30 °C, which is close to the result reported in the previous literature [29]. Thusly, a little amount of SeS₂ doping (x≤1) can be effectively enhance the ionic conductivity.

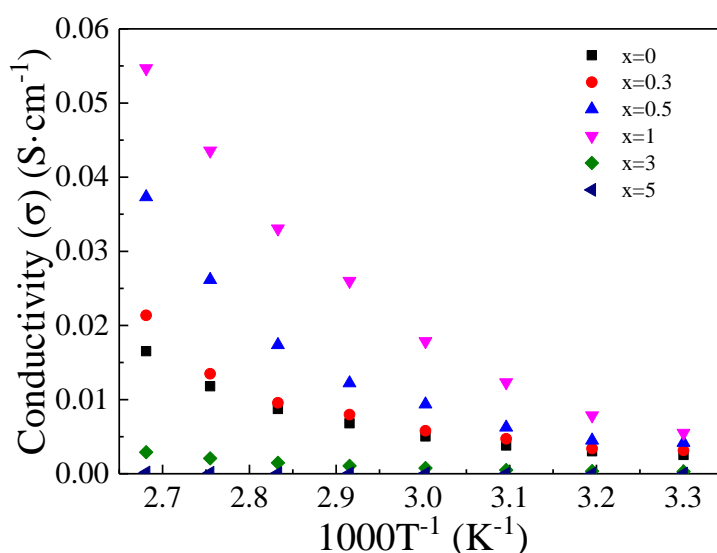


Figure 3.2 Ion conductivity of 70Li₂S·30-xP₂S₅·xSeS₂ (x=0, 0.3, 0.5, 1, 3, 5) solid electrolyte systems.

As shown in Figure 3.3A, no semicircles appear in Nyquist plots of the $70\text{Li}_2\text{S}\cdot 30\text{P}_2\text{S}_5$ and $70\text{Li}_2\text{S}\cdot 29\text{P}_2\text{S}_5\cdot 1\text{SeS}_2$ glass-ceramics at 20 °C. Here, the total resistance can be obtained from the intersection of the straight line with the Z' axis, which is originated from the bulk resistance and interfacial resistance of the electrolyte material and the diffusion impedance [37]. As a result, the total resistances of $70\text{Li}_2\text{S}\cdot 30\text{P}_2\text{S}_5$ and $70\text{Li}_2\text{S}\cdot 29\text{P}_2\text{S}_5\cdot 1\text{SeS}_2$ SEs are 23.86 and 53.23 Ω , respectively. The ionic conductivity of $70\text{Li}_2\text{S}\cdot 30\text{P}_2\text{S}_5$ is $2.37\times 10^{-3} \text{ S}\cdot\text{cm}^{-1}$. In comparison, the ionic conductivity of $70\text{Li}_2\text{S}\cdot 29\text{P}_2\text{S}_5\cdot 1\text{SeS}_2$ is $5.28\times 10^{-3} \text{ S}\cdot\text{cm}^{-1}$ at 20 °C, indicating that the doping of SeS_2 can increase ionic conductivity effectively.

Figure 3.3B shows the temperature dependence of ionic conductivities of $70\text{Li}_2\text{S}\cdot 30\text{P}_2\text{S}_5$ and $70\text{Li}_2\text{S}\cdot 29\text{P}_2\text{S}_5\cdot 1\text{SeS}_2$ glass-ceramics from 30 °C to 100 °C. Here, the activation energy E_a is calculated according to the Arrhenius equation $\sigma(T)=A \exp(-E_a/RT)$, where T is the absolute temperature and A is a pre-exponential factor. As a result, the E_a of the $70\text{Li}_2\text{S}\cdot 29\text{P}_2\text{S}_5\cdot 1\text{SeS}_2$ is decreased to 24.70 $\text{kJ}\cdot\text{mol}^{-1}$ from 26.06 $\text{kJ}\cdot\text{mol}^{-1}$ for $70\text{Li}_2\text{S}\cdot 30\text{P}_2\text{S}_5$ due to the doping of SeS_2 . This is consistent with the ionic conductivity measurement result. Herein, the lower E_a also indicates a faster Li^+ migration capability of the electrolyte.

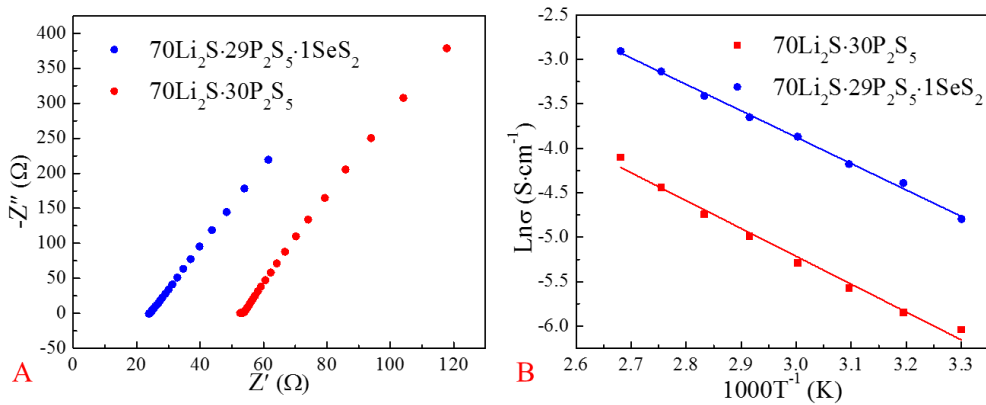


Figure 3.3 (A) Nyquist plots of $70\text{Li}_2\text{S}\cdot 30\text{P}_2\text{S}_5$ and $70\text{Li}_2\text{S}\cdot 29\text{P}_2\text{S}_5\cdot 1\text{SeS}_2$ glass-ceramics at 20°C , (B) Temperature dependence of conductivity for $70\text{Li}_2\text{S}\cdot 30\text{P}_2\text{S}_5$ and $70\text{Li}_2\text{S}\cdot 29\text{P}_2\text{S}_5\cdot 1\text{SeS}_2$ glass-ceramics from 30°C to 100°C .

Figure 3.4 shows XRD patterns of $70\text{Li}_2\text{S}\cdot 30\text{-xP}_2\text{S}_5\cdot \text{xSeS}_2$ ($x=0, 0.3, 0.5, 1, 3, 5$) glass ceramics. From Figure 3.4A, it can be seen that the crystalline structures of $70\text{Li}_2\text{S}\cdot 30\text{-xP}_2\text{S}_5\cdot \text{xSeS}_2$ ($x=0.3, 0.5, 1$) are similar to that of $70\text{Li}_2\text{S}\cdot 30\text{P}_2\text{S}_5$ one, indicating that the doping of SeS_2 with a little amount ($x\leq 1$) cannot change the crystal structure of original $70\text{Li}_2\text{S}\cdot 30\text{P}_2\text{S}_5$. In contrast, the intensity of the main XRD peak decreases with the further increasing of the SeS_2 doping amount ($x=3, 5$), and meanwhile some impurity phases appear. As a result, the ionic conductivity ($70\text{Li}_2\text{S}\cdot 30\text{-xP}_2\text{S}_5\cdot \text{xSeS}_2$ ($x=3, 5$)) also decreases. Moreover, as shown in Figure 3.4B, no peak shift is observed for the LPS with $x=0.3$ and 0.5 mol%, but a shift towards the lower angle is found as $x=1$ mol%, which indicates that the crystal lattice should be expanded due to the larger ionic radius of Se^{4+} (0.64 \AA) than P^{5+} (0.52 \AA). Furthermore, by charge balance, geometric optimization and structure analysis based on first-principle calculations [38], it is found that the peak appeared at $2\theta=32.2^\circ$ can be indexed as the diffraction from the (113) plane (Figure 3.5 and Figure 3.4C). Similarly, Table 3.1 summarizes the unit cell dimensions evaluated by

the refinement of the whole diffraction profile. Generally, a, b, c-axis dimensions and unit cell volume gradually increase as Se-doping. This increasing trend in the dimension correlates with the substitution of P^{5+} with smaller effective ionic radius by the larger Se^{4+} in the $Li_7P_3S_{11}$ lattice structure. The difference in variation of dimensions reflects the facts about the structural change and transport of Li^+ . As shown in Figure 3.5, when the phosphorus element is replaced by selenium, because Se-S bond is longer than P-S bond, and the resulted Se-S bonds are not on the crystal (113) plane, it leads to the weakening of the peak intensity at $2\theta=32.2^\circ$ (Figure 3.4C). Such a new structure could provide larger transmission channel for Li^+ ions. Therefore, selenium can be well doped into the lattices of LPS glass ceramic, generating novel active sites (defects) and broadening the channels for Li^+ transmission, and thusly promote the Li^+ ionic conductivity of LPS glass ceramics.

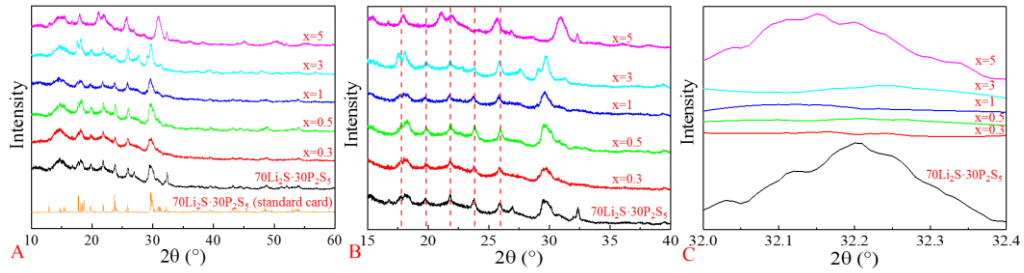


Figure 3.4 XRD patterns of the $70Li_2S \cdot 30-xP_2S_5 \cdot xSeS_2$ ($x=0, 0.3, 0.5, 1, 3, 5$) glass-ceramics (A) in the 2θ range from 10° to 60° and (B) Magnified 2θ range from 15° to 30° and (C) 32.0° to 32.4° .

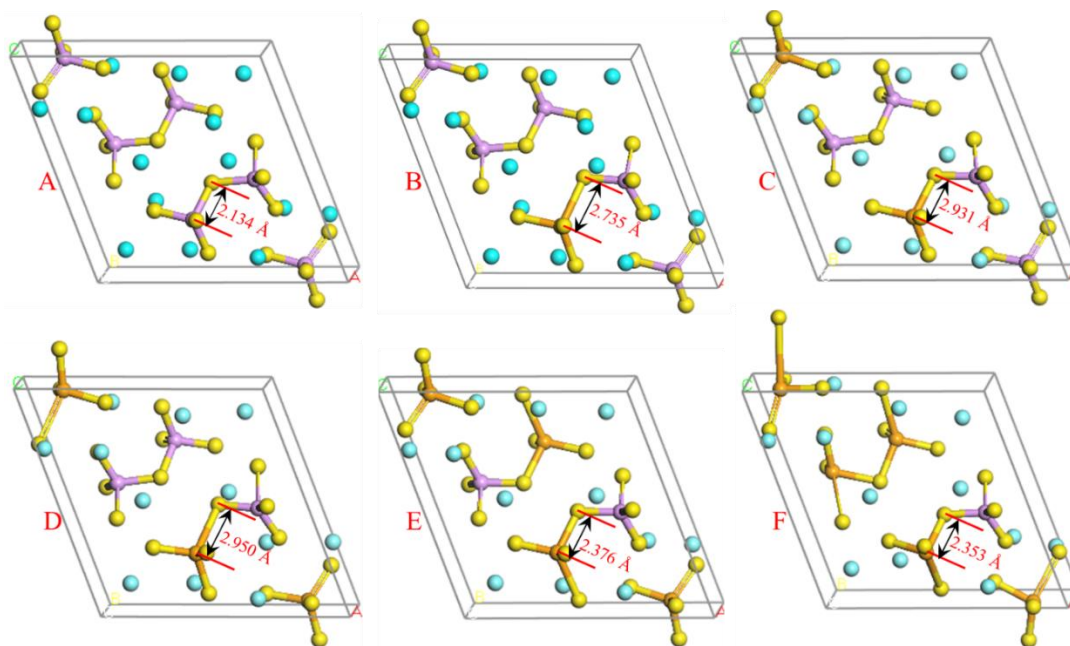


Figure 3.5 (Color online.) Ball and stick diagrams of supercells of calculated optimum structures of (A): $70\text{Li}_2\text{S}\cdot 30\text{P}_2\text{S}_5$, (B): 1 Se doping $70\text{Li}_2\text{S}\cdot 30\text{P}_2\text{S}_5$, (C): 2 Se doping $70\text{Li}_2\text{S}\cdot 30\text{P}_2\text{S}_5$, D): 3 Se doping $70\text{Li}_2\text{S}\cdot 30\text{P}_2\text{S}_5$, (E): 4 Se doping $70\text{Li}_2\text{S}\cdot 30\text{P}_2\text{S}_5$, and (F): 5 Se doping $70\text{Li}_2\text{S}\cdot 30\text{P}_2\text{S}_5$ electrolytes. Li, P, S, and Se are indicated with wathet blue, purple, yellow, and orange balls, respectively.

Table 3.1 Refined unit cell dimensions and cell angles in Se doping $70\text{Li}_2\text{S}\cdot 30\text{P}_2\text{S}_5$.

Composition	a (Å)	b (Å)	c (Å)	α	β	γ	V (Å ³)	Phase model
$70\text{Li}_2\text{S}\cdot 30\text{P}_2\text{S}_5$	12.5009	6.0316	12.5303	102.845	113.202	74.467	829.348	Triclinic
1Se	12.5017	6.0319	12.5308	102.846	113.200	74.466	829.492	Triclinic
2Se	12.5017	6.0321	12.5308	102.846	113.198	74.467	829.527	Triclinic
3Se	12.5017	6.0322	12.5308	102.846	113.200	74.467	829.506	Triclinic
4Se	12.5014	6.0319	12.5308	102.845	113.200	74.468	829.477	Triclinic
5Se	12.5016	6.0319	12.5309	102.846	113.202	74.466	829.469	Triclinic

Figure 3.6 shows the DSC curves of $70\text{Li}_2\text{S}\cdot 30\text{-xP}_2\text{S}_5\cdot \text{xSeS}_2$ ($x=0, 0.3, 0.5, 1, 3, 5$) glasses. For $70\text{Li}_2\text{S}\cdot 30\text{-xP}_2\text{S}_5\cdot \text{xSeS}_2$ ($x=0, 0.3, 0.5, 1$) glasses. The obvious exothermic peaks attributed to the crystallization are observed between $260\text{ }^\circ\text{C}$ and $280\text{ }^\circ\text{C}$ in the DSC curves. These results suggest that these electrolyte samples are in a glassy state. Furthermore, the crystallization temperatures of $70\text{Li}_2\text{S}\cdot 30\text{-xP}_2\text{S}_5\cdot \text{xSeS}_2$ ($x=0.3, 0.5, 1$) glasses are slightly different from those of $70\text{Li}_2\text{S}\cdot 30\text{P}_2\text{S}_5$ glass, indicating that the added SeS_2 has been incorporated into $\text{Li}_2\text{S}\text{--P}_2\text{S}_5$ matrix [39]. When more SeS_2 ($x=3, 5$) is added, the intensity of the peak is weakened and some other exothermic peaks appear in the DSC curves, which might mean that superabundant SeS_2 hinders the crystallization of the phases.

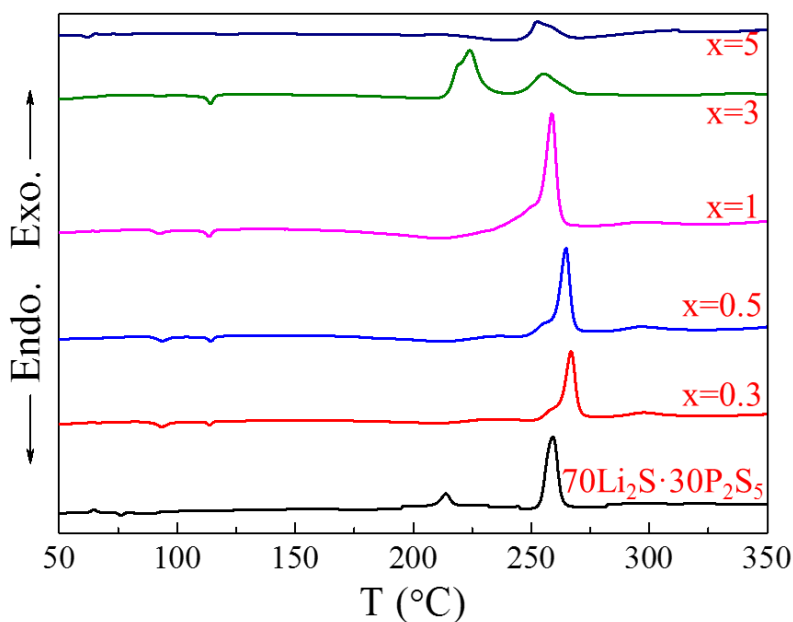


Figure 3.6 DSC curves of $70\text{Li}_2\text{S}\cdot 30\text{-xP}_2\text{S}_5\cdot \text{xSeS}_2$ ($x=0, 0.3, 0.5, 1, 3, 5$) glasses prepared by ball milling.

Figure 3.7 shows Raman spectra of $70\text{Li}_2\text{S} \cdot 30\text{-xP}_2\text{S}_5 \cdot \text{xSeS}_2$ ($x=0, 0.3, 0.5, 1, 3, 5$) glass ceramic electrolytes. The band at 425 cm^{-1} is observed in the spectra of the $70\text{Li}_2\text{S} \cdot 30\text{-xP}_2\text{S}_5 \cdot \text{xSeS}_2$ ($x=0, 0.3, 0.5, 1, 3, 5$) electrolytes, which is attributable to PS_4^{3-} ions [40], suggesting that PS_4^{3-} ions remained in the electrolyte with SeS_2 . However, the peaks in the Raman spectra of $70\text{Li}_2\text{S} \cdot 30\text{-xP}_2\text{S}_5 \cdot \text{xSeS}_2$ ($x=3, 5$) electrolytes had a certain degree of shift and attenuation, indicating that the addition of the SeS_2 destroys the structure of some PS_4^{3-} ions. Moreover, the intensity decreases with the increasing of x in the mixed systems. Meanwhile, this peak is slightly shifted toward higher wavenumber for $x=0$ (423 cm^{-1}) and $x=0.3$ (425 cm^{-1}), which should be attributed to the increase of the length of PS_4^{3-} chain as seen in the similar amorphous mixtures [41]. These results are agreement well with the above DSC results.

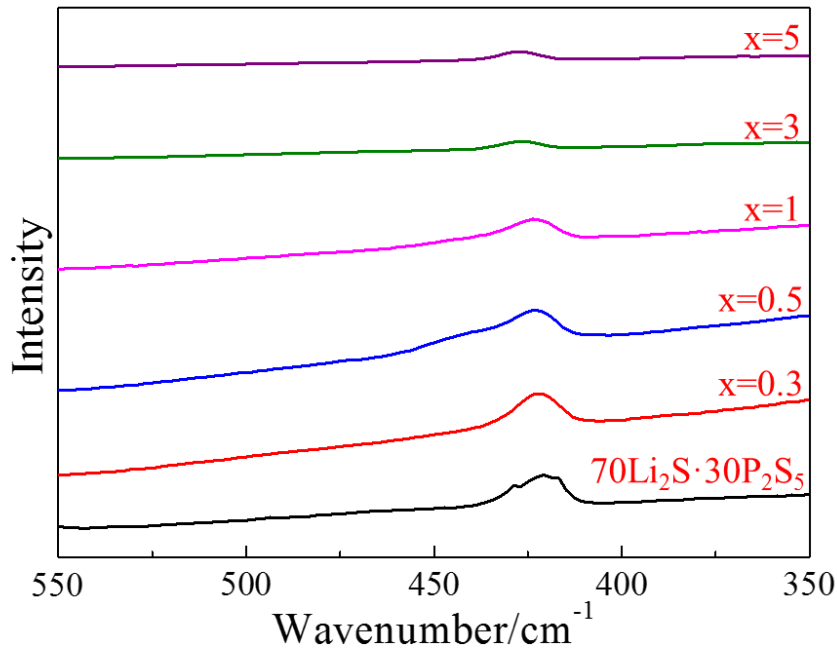


Figure 3.7 Raman spectra of $70\text{Li}_2\text{S} \cdot 30\text{-xP}_2\text{S}_5 \cdot \text{xSeS}_2$ ($x=0, 0.3, 0.5, 1, 3, 5$) electrolytes.

Figure 3.8 shows the time-dependent current profile for Li/solid electrolyte/Li symmetric batteries with the $70\text{Li}_2\text{S}\cdot 30\text{P}_2\text{S}_5$ and $70\text{Li}_2\text{S}\cdot 29\text{P}_2\text{S}_5\cdot 1\text{SeS}_2$ SEs cycled for up to 66 h under a constant voltage of 0.1 V at 30 °C. It is obvious that a current decay of cycling occurs, which is possible to be resulted from the dendrite crossover in the battery in the case using $70\text{Li}_2\text{S}\cdot 30\text{P}_2\text{S}_5$ electrolyte [42]. In contrast, the current maintains stable for $70\text{Li}_2\text{S}\cdot 29\text{P}_2\text{S}_5\cdot 1\text{SeS}_2$ electrolyte, indicating its high stability with metallic lithium. Thusly, $70\text{Li}_2\text{S}\cdot 29\text{P}_2\text{S}_5\cdot 1\text{SeS}_2$ electrolyte could resist the dendrite crossover during a long-term cycling. This proves that the SeS_2 doping improves the electrochemical stability between sulfide electrolytes and lithium metal, which is a very important for ASSLSBs.

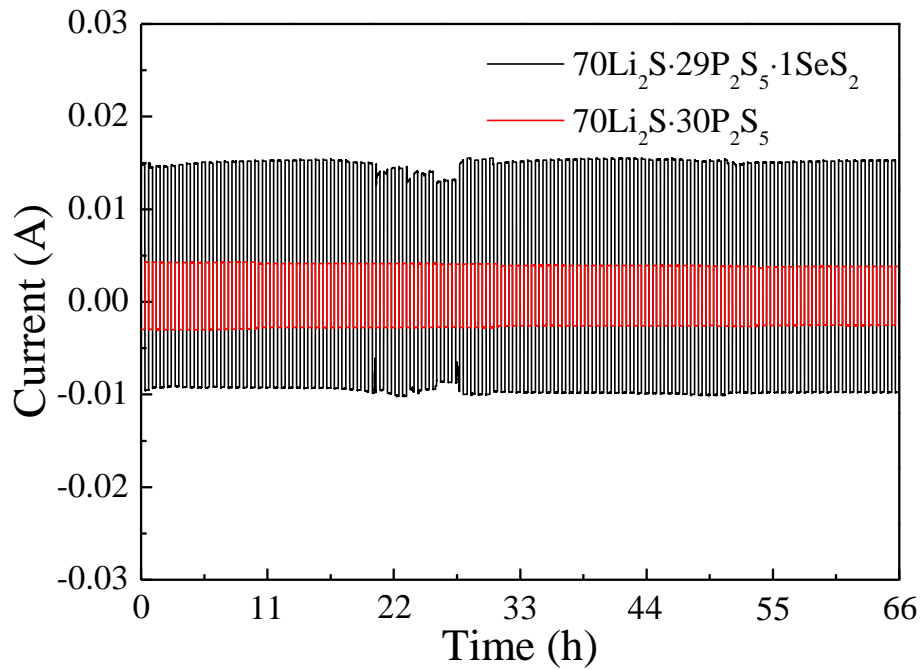


Figure 3.8 Chronoamperometry test of $70\text{Li}_2\text{S}\cdot 30\text{P}_2\text{S}_5$ and $70\text{Li}_2\text{S}\cdot 29\text{P}_2\text{S}_5\cdot 1\text{SeS}_2$ solid electrolyte-based Li/solid electrolyte/Li symmetric batteries cycled at a constant voltage

of 0.1 V at 30 °C.

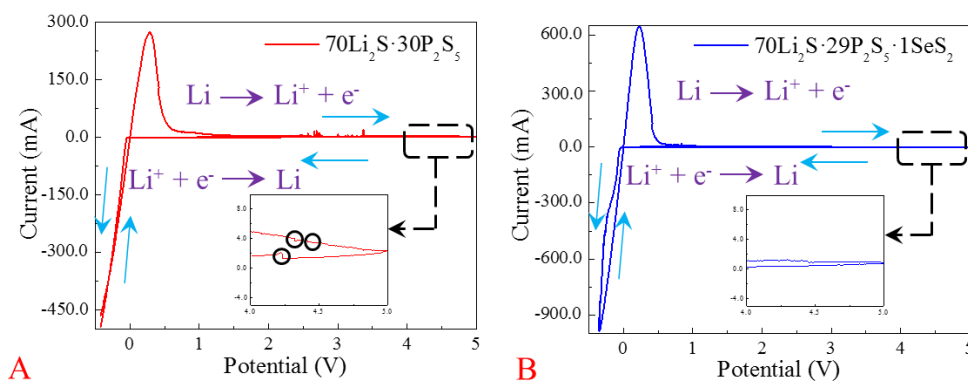


Figure 3.9 CV curves of (A) 70Li₂S·30P₂S₅ and (B) 70Li₂S·29P₂S₅·1SeS₂ glass-ceramics based Li/solid electrolyte/stainless steel batteries in the potential range from -0.5 V to 5 V (vs. Li/Li⁺) at a scanning rate of 1 mV·s⁻¹ at 30 °C.

Apart from the requirement of high ionic conductivity, electrochemical stability window of solid electrolyte is also crucial for its practical application in ASSLSBs. Figure 3.9 represents CV scan results of Li/solid electrolyte/stainless steel battery cells. No other additional reactions are observed in these curves except for lithium deposition ($\text{Li}^+ + \text{e}^- \rightarrow \text{Li}$) and dissolution ($\text{Li} \rightarrow \text{Li}^+ + \text{e}^-$) between -0.5 and 1 V, indicating that both of 70Li₂S·30P₂S₅ and 70Li₂S·29P₂S₅·1SeS₂ SEs have a wide electrochemical window up to 5 V vs. Li⁺/Li. Furthermore, the insets show the enlarged CV curves in the voltage range from 4.0 to 5.0 V. It is obvious that large and wrinkled current curves appear for the 70Li₂S·30P₂S₅ glass ceramic. In contrast, the current curves become smooth and stable by the doping of SeS₂. These results indicate that the incorporation of a small amount of SeS₂ into Li₂S-P₂S₅ can improve the electrochemical stability.

Figure 3.10(A-B) shows the SEM images of pure rGO and S-rGO composite. One can see that the obtained pure rGO and S-rGO composite have a wrinkled nanosheet structure with a curly morphology. From the elemental composition analysis by EDS (Figure 3.10C), sulfur is confirmed to be homogenously distributed on the rGO nanosheets. Such a distinctive nanostructure of rGO endows it to have a great potential application in the electrode of lithium sulfur batteries because of its excellent electronic conductive behavior, good mechanical properties, and high surface area. These characteristics make it enhance the contact between the active materials of electrode and the electrolyte [43-45]. Thusly, in this study, it is used for prepare high-performance cathode material in ASSLSBs.

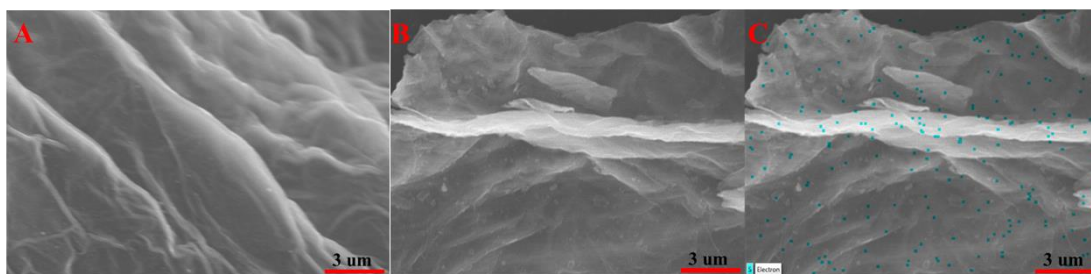


Figure 3.10 SEM images of the as-prepared (A) pure rGO and (B) S-rGO, EDS image of (C) S-rGO.

Figure 3.11 compares the cyclic voltammetry properties of $\text{rGO-S}/70\text{Li}_2\text{S} \cdot 30\text{P}_2\text{S}_5/\text{Li}$, and $\text{rGO-S}/70\text{Li}_2\text{S} \cdot 29\text{P}_2\text{S}_5 \cdot 1\text{SeS}_2/\text{Li}$ batteries. Here, the oxidation and the reduction peaks are observed at 2.4-2.5 V and 1.8 V, respectively. The symmetrical pair of oxidation and reduction peaks indicates a well reversible Li^+ ion intercalation–deintercalation process. It is obvious that the ASSLSB with the rGO-S cathode and the $70\text{Li}_2\text{S} \cdot 29\text{P}_2\text{S}_5 \cdot 1\text{SeS}_2$ solid electrolyte has higher capacitance performance than the $70\text{Li}_2\text{S} \cdot 30\text{P}_2\text{S}_5$ electrolyte. Thusly, the $\text{rGO-S}/70\text{Li}_2\text{S} \cdot 29\text{P}_2\text{S}_5 \cdot 1\text{SeS}_2/\text{Li}$ battery has lower internal resistance, which would be beneficial to get higher specific capacitance and better power performance [46].

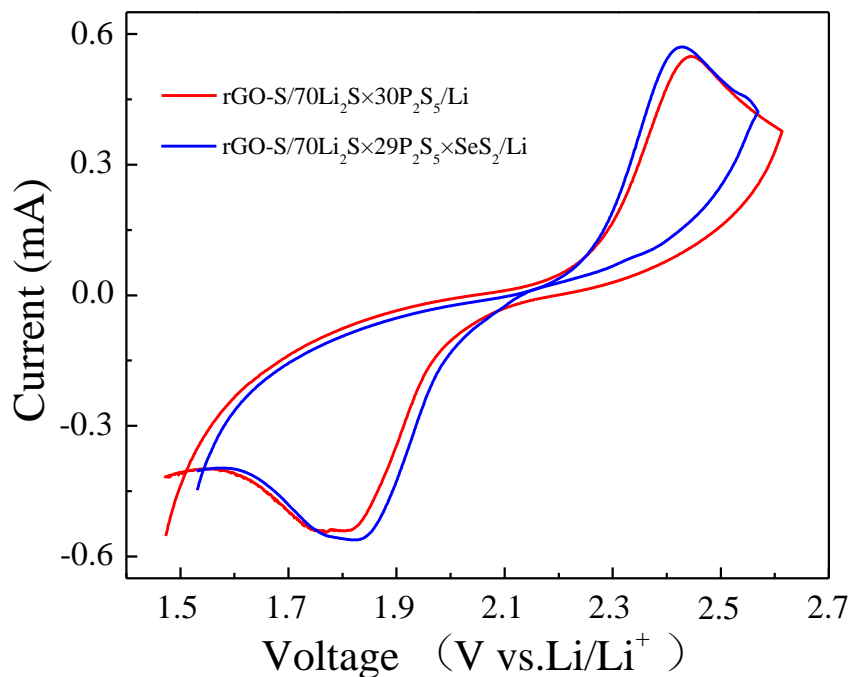


Figure 3.11 CV measurements of ASSLSBs based on $70\text{Li}_2\text{S} \cdot 30\text{P}_2\text{S}_5$ and $70\text{Li}_2\text{S} \cdot 29\text{P}_2\text{S}_5 \cdot 1\text{SeS}_2$ electrolytes respectively at 30°C .

Figure 3.12A shows initial charge-discharge curves of $\text{rGO-S}/70\text{Li}_2\text{S} \cdot 30\text{P}_2\text{S}_5/\text{Li}$, and $\text{rGO-S}/70\text{Li}_2\text{S} \cdot 29\text{P}_2\text{S}_5 \cdot 1\text{SeS}_2/\text{Li}$ ASSLSBs. One plateau at around 2.5 V is observed on the charge curve while one plateau at around 1.8 V appears on the discharge curve. The charge-discharge capacity of the solid battery with the $70\text{Li}_2\text{S} \cdot 29\text{P}_2\text{S}_5 \cdot 1\text{SeS}_2$ electrolyte is obviously larger than those with the $70\text{Li}_2\text{S} \cdot 30\text{P}_2\text{S}_5$ electrolyte. As a result, the first discharge capacity ($658.1 \text{ mAh} \cdot \text{g}^{-1}$) of $\text{rGO-S}/70\text{Li}_2\text{S} \cdot 29\text{P}_2\text{S}_5 \cdot 1\text{SeS}_2/\text{Li}$ ASSLSB is about 1.08 times larger than that of $\text{rGO-S}/70\text{Li}_2\text{S} \cdot 30\text{P}_2\text{S}_5/\text{Li}$ ASSLSB ($607.5 \text{ mAh} \cdot \text{g}^{-1}$) at $0.1 \text{ mA} \cdot \text{cm}^{-2}$, indicating that SeS_2 doping in $\text{Li}_2\text{S}-\text{P}_2\text{S}_5$ solid electrolyte can effectively increase the capacity of ASSLSBs due to the improved ionic conductivity, and improved contact property with the electrode due to the reduced interface resistance. Moreover, the cycling performances of $\text{rGO-S}/70\text{Li}_2\text{S} \cdot 30\text{P}_2\text{S}_5/\text{Li}$, and $\text{rGO-S}/70\text{Li}_2\text{S} \cdot 29\text{P}_2\text{S}_5 \cdot 1\text{SeS}_2/\text{Li}$

ASSLSBs are displayed in Figure 3.12B. The ASSLSB of rGO-S/70Li₂S·29P₂S₅·1SeS₂/Li exhibits much better cycle performance than the rGO-S/70Li₂S·30P₂S₅/Li, the coulombic efficiencies of rGO-S/70Li₂S·30P₂S₅/Li, and rGO-S/70Li₂S·29P₂S₅·1SeS₂/Li ASSLSB are almost the same with a value of approximately 97% after the 20 cycles, indicating that a stable interface layer has been formed at the electrode-electrolyte interface which can effectively avoid the dendrite crossover. It should be noted that the capacity of rGO-S/70Li₂S·29P₂S₅·1SeS₂/Li ASSLSB suddenly drops during 10-12 cycles which is caused by unconscious collision by hand during the test. Even so, the ASSLSB of rGO-S/70Li₂S·29P₂S₅·1SeS₂/Li still shows an excellent cycling stability and the reversible discharge capacity maintains at 558.3 mAh·g⁻¹ after 100 cycles with a coulombic efficiency of almost 99%, attaining 84.8% of capacity retention compared to the 1st discharge capacity. In contrast, it should be noted that rGO-S/70Li₂S·30P₂S₅/Li battery shows the discharge capacity of 283.5 mAh·g⁻¹ after 100 cycles, which is only 46.7% of the 1st discharge capacity. Thusly, the excellent rate and cycling stability of ASSLSBs can be realized by employing 70Li₂S·29P₂S₅·1SeS₂ as the solid electrolyte and rGO-S nanocomposite as the cathode material.

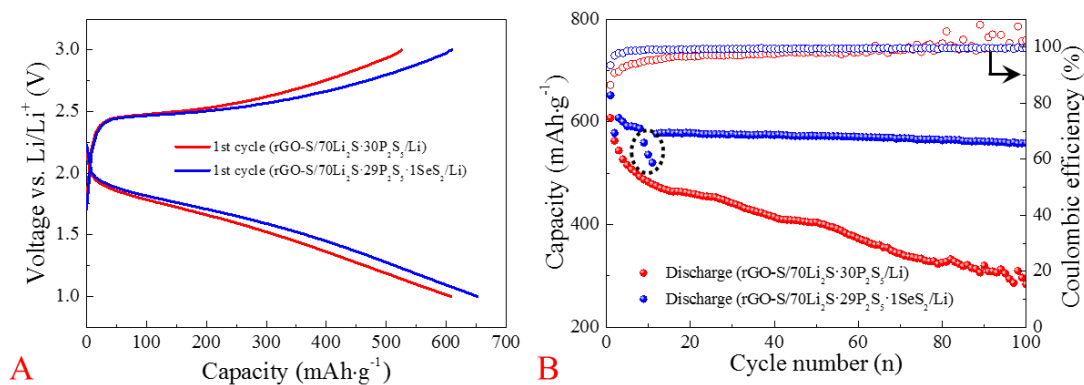


Figure 3.12 (A) The initial charge-discharge curves and (B) cycle performances of

ASSLSBs based on $70\text{Li}_2\text{S}\cdot 30\text{P}_2\text{S}_5$ and $70\text{Li}_2\text{S}\cdot 29\text{P}_2\text{S}_5\cdot 1\text{SeS}_2$ electrolytes at a rate of $0.1\text{ mA}\cdot\text{cm}^{-2}$ at $30\text{ }^\circ\text{C}$.

In order to further understand the improved electrochemical performances of ASSLSBs assembled with rGO-S nanocomposite cathode and $70\text{Li}_2\text{S}\cdot 29\text{P}_2\text{S}_5\cdot 1\text{SeS}_2$ solid electrolyte, the EIS measurements of ASSLSB and interface studies of SE/Li after the charge-discharge test were performed. Figure 3.13 shows Nyquist plots of rGO-S/ $70\text{Li}_2\text{S}\cdot 30\text{P}_2\text{S}_5$ /Li, and rGO-S/ $70\text{Li}_2\text{S}\cdot 29\text{P}_2\text{S}_5\cdot 1\text{SeS}_2$ /Li ASSLSBs. As shown in Figure 3.13A, the Nyquist plot of the ASSLSB with $70\text{Li}_2\text{S}\cdot 29\text{P}_2\text{S}_5\cdot 1\text{SeS}_2$ solid electrolyte before the charge-discharge process shows a smaller semicircle than that with the $70\text{Li}_2\text{S}\cdot 30\text{P}_2\text{S}_5$ solid electrolyte. Here, the intercept of the Z_0 axis in the high-frequency region corresponds to the resistance of the solid electrolyte layer, and the resistance from the semicircle in the middle-frequency region is attributed to the charge transfer resistance and the interface resistance between the cathode and solid electrolyte, the interface resistances of the ASSLSB assembled with the $70\text{Li}_2\text{S}\cdot 30\text{P}_2\text{S}_5$ and $70\text{Li}_2\text{S}\cdot 29\text{P}_2\text{S}_5\cdot 1\text{SeS}_2$ electrolytes before the charge-discharge processes are $463\text{ }\Omega$ and $358\text{ }\Omega$, respectively. As a result, the $70\text{Li}_2\text{S}\cdot 29\text{P}_2\text{S}_5\cdot 1\text{SeS}_2$ solid electrolyte has lower charge transfer resistance and better reaction kinetics for ASSLSBs. Figure 3.13B shows the EIS spectra of the batteries assembled with the $70\text{Li}_2\text{S}\cdot 30\text{P}_2\text{S}_5$ and $70\text{Li}_2\text{S}\cdot 29\text{P}_2\text{S}_5\cdot 1\text{SeS}_2$ electrolytes after the 20 charge-discharge cycles. Compared with that before the charge-discharge process (Figure 3.13A), the interface resistances of the ASSLSB of $70\text{Li}_2\text{S}\cdot 30\text{P}_2\text{S}_5$ and $70\text{Li}_2\text{S}\cdot 29\text{P}_2\text{S}_5\cdot 1\text{SeS}_2$ electrolytes after the 20 charge-discharge cycles increase to $1051\text{ }\Omega$ and $642\text{ }\Omega$, respectively. Meanwhile, compared with the rGO/ $70\text{Li}_2\text{S}\cdot 30\text{P}_2\text{S}_5$ /Li battery, the interfacial resistance of the rGO-S/ $70\text{Li}_2\text{S}\cdot 29\text{P}_2\text{S}_5\cdot 1\text{SeS}_2$ /Li battery changed only a little and the battery becomes more stable after the multiple charge-discharge cycles.

These results suggest that adding a certain amount of SeS_2 into the $\text{Li}_2\text{S}-\text{P}_2\text{S}_5$ electrolyte substrate could decrease interfacial resistance between SE and cathode material.

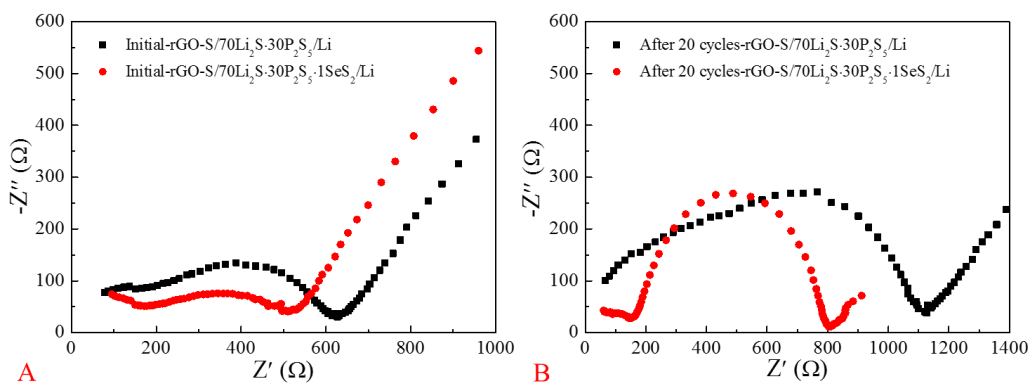


Figure 3.13 Nyquist plots of $\text{rGO}/70\text{Li}_2\text{S}\cdot30\text{P}_2\text{S}_5/\text{Li}$, and $\text{rGO-S}/70\text{Li}_2\text{S}\cdot29\text{P}_2\text{S}_5\cdot1\text{SeS}_2/\text{Li}$ ASSLSBs at $30\text{ }^\circ\text{C}$. Measurements were conducted (A) before and (B) after 20 cycles at $0.1\text{ mA}\cdot\text{cm}^{-2}$.

In order to clarify the dendrite crossover between SE and Li, the interface between the $70\text{Li}_2\text{S}\cdot30\text{P}_2\text{S}_5/70\text{Li}_2\text{S}\cdot29\text{P}_2\text{S}_5\cdot1\text{SeS}_2$ and Li based $\text{rGO-S}/\text{solid electrolyte}/\text{Li}$ batteries were observed by SEM. Figure 3.14 shows the SEM images of the interface between the (A) $70\text{Li}_2\text{S}\cdot30\text{P}_2\text{S}_5/(\text{B}) 70\text{Li}_2\text{S}\cdot29\text{P}_2\text{S}_5\cdot1\text{SeS}_2$ and Li layer after 100 charge-discharge cycles. The interface between the $70\text{Li}_2\text{S}\cdot30\text{P}_2\text{S}_5/\text{Li}$ layer (Figure 3.14A) has a rough surface and some lithium dendrites appear. In contrast, the interface between the $70\text{Li}_2\text{S}\cdot29\text{P}_2\text{S}_5\cdot1\text{SeS}_2/\text{Li}$ layer (Figure 3.14B) is smoother, although some lithium dendrites also appear, it is significantly less than the case using the $70\text{Li}_2\text{S}\cdot30\text{P}_2\text{S}_5$ electrolyte. These results indicate that the proper amount of SeS_2 doping into the $\text{Li}_2\text{S}-\text{P}_2\text{S}_5$ electrolyte can effectively reduce the generation of lithium dendrites and improve interfacial stability.

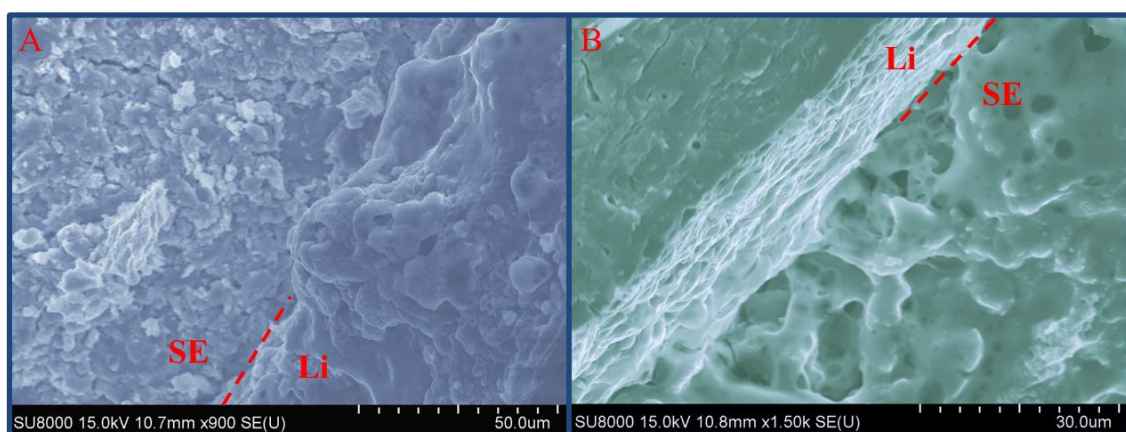


Figure 3.14 SEM images of the interface between the (A) $70\text{Li}_2\text{S}\cdot 30\text{P}_2\text{S}_5$; (B) $70\text{Li}_2\text{S}\cdot 29\text{P}_2\text{S}_5\cdot 1\text{SeS}_2$ and Li in rGO-S/solid electrolyte/Li batteries at $0.1\text{ mA}\cdot\text{cm}^{-2}$ for 100 charge-discharge cycles.

3.4 Conclusions

In conclusion, the ionic conductivity of $70\text{Li}_2\text{S}\cdot 30\text{P}_2\text{S}_5$ solid electrolyte can be effectively improved by doping a small amount of SeS_2 by a facile mechanical milling followed with a heat treatment process. The $70\text{Li}_2\text{S}\cdot 29\text{P}_2\text{S}_5\cdot 1\text{SeS}_2$ solid electrolyte exhibits a highest conductivity of $5.28\times 10^{-3}\text{ S}\cdot\text{cm}^{-1}$ at $20\text{ }^\circ\text{C}$ with a lowest activation energy of $24.70\text{ kJ}\cdot\text{mol}^{-1}$ and excellent electrochemical stability among all prepared electrolytes. The crystalline structures of SeS_2 doping LPS solid electrolyte by XRD analysis-refinement assisting with the first principles calculations based on the DFT. Furthermore, the ASSLSBs assembled based on $70\text{Li}_2\text{S}\cdot 29\text{P}_2\text{S}_5\cdot 1\text{SeS}_2$ electrolyte and sulfur-reduced graphene oxide (S-rGO) composite cathode shows an initial discharge capacity of $658.1\text{ mAh}\cdot\text{g}^{-1}$ at $0.1\text{ mA}\cdot\text{cm}^{-2}$, and an excellent cycling stability with a maintained reversible discharge capacity at $558.3\text{ mAh}\cdot\text{g}^{-1}$ after 100 cycles with a coulombic efficiency of almost 100%, attaining 84.8% of capacity retention compared to the 1st discharge capacity. And analytical results of EIS and the interface observe by SEM reveal that addition of SeS_2 into the $\text{Li}_2\text{S}\cdot\text{P}_2\text{S}_5$ electrolyte substrate can decrease the

interfacial resistance between the electrode and solid electrolyte and reduce the production of lithium dendrites. It is expected that $70\text{Li}_2\text{S}\cdot 29\text{P}_2\text{S}_5\cdot 1\text{SeS}_2$ electrolyte can be served as an effective solid electrolyte for the construction of high performance all-solid-state batteries.

References

- [1] Y. Li, J. Song, J. Yang, A review on structure model and energy system design of lithium-ion battery in renewable energy vehicle, *Renewable Sustainable Energy Rev.* 37 (2014) 627-633.
- [2] H. Peng, J. Huang, X. Cheng, Q. Zhang, Review on high-loading and high-energy lithium-sulfur batteries, *Adv. Energy Mater.* 7 (2017) 1700260.
- [3] H. Peng, J. Huang, Q. Zhang, A review of flexible lithium-sulfur and analogous alkali metal-chalcogen rechargeable batteries, *Chem. Soc. Rev.* 46 (2017) 5237-5288.
- [4] D. Chen, K. Wen, W. Lv, Z. Wei, W. He, Separator modification and functionalization for inhibiting the shuttle effect in lithium-sulfur batteries, *Phys Status Solidi-R* 12 (2018) 1800249.
- [5] M. Waqas, C. Tan, W. Lv, S. Ali, B. Boateng, W. Chen, Z. Wei, C. Feng, J. Ahmed, J.B. Goodenough, A highly-efficient composite separator with strong ligand interaction for high-temperature lithium-ion batteries, *ChemElectroChem* 5 (2018) 2722-2728.
- [6] S. Ali, M. Waqas, X. Jing, N. Chen, D. Chen, J. Xiong, W. He, Carbon-tungsten disulfide composite bilayer separator for high-performance lithium-sulfur batteries, *ACS Appl. Mater. Interfaces* 10 (2018) 39417-39421.

- [7] W. Chen, T. Lei, C. Wu, M. Deng, C. Gong, K. Hu, Y. Ma, L. Dai, W. Lv, W. He, Designing safe electrolyte systems for a high-stability lithium-sulfur battery, *Adv. Energy Mater.* 8 (2018) 1702348.
- [8] D. Lei, K. Shi, H. Ye, Z. Wan, Y. Wang, L. Shen, B. Li, Q. Yang, F. Kang, Y. He, Progress and perspective of solid-state lithium-sulfur batteries, *Adv. Funct. Mater.* (2018) 1707570.
- [9] A. Hayashi, A. Sakuda, M. Tatsumisago, Development of sulfide SEs and interface formation processes for bulk-type all-solid-state Li and Na batteries, *Frontiers in Energy Research* 4 (2016) 25.
- [10] C. Sun, J. Liu, Y. Gong, D. Wilkinson, J. Zhang, Recent advances in all-solid-state rechargeable lithium batteries, *Nano Energy* 33 (2017) 363-386.
- [11] J. Bachman, S. Muy, A. Grimaud, H. Chang, N. Pour, S. Lux, O. Paschos, F. Maglia, S. Lupart, P. Lamp, Inorganic solid-state electrolytes for lithium batteries: mechanisms and properties governing ion conduction, *Chem. Rev.* 116 (2015) 140-162.
- [12] W. Zhang, J. Nie, F. Li, Z. Wang, C. Sun, A durable and safe solid-state lithium battery with a hybrid electrolyte membrane, *Nano Energy* 45 (2018) 413-419.
- [13] H. Hou, Q. Xu, Y. Pang, L. Li, J. Wang, C. Zhang, C. Sun, Efficient storing energy harvested by triboelectric nanogenerators using a safe and durable all-solid-state sodium-ion battery, *Adv. Sci.* 4 (2017) 1700072.
- [14] J. Wang, C. Sun, Y. Gong, H. Zhang, J. Alonso, M. Fernández-Díaz, Z. Wang, J. Goodenough, Imaging the diffusion pathway of Al^{3+} ion in NASICON-type $(\text{Al}_{0.2}\text{Zr}_{0.8})_{20/19}\text{Nb}(\text{PO}_4)_3$ as electrolyte for rechargeable solid-state Al batteries, *Chin. Phys. B* 27 128201-128201.

- [15] Y. Zhang, J. Lai, Y. Gong, Y. Hu, J. Liu, C. Sun, Z. Wang, A safe high-performance all-solid-state lithium–vanadium battery with a freestanding V_2O_5 nanowire composite paper cathode, *ACS Appl. Mater. Interfaces* 8 (2016) 34309-34316.
- [16] X. Ban, W. Zhang, N. Chen, C. Sun, A high-performance and durable poly(ethylene oxide)-based composite solid electrolyte for all solid-state lithium battery, *J. Phys. Chem. C* 122 (2018) 9852-9858.
- [17] Z. Xie, Z. Wu, X. An, A. Yoshida, Z. Wang, X. Hao, A. Abudula, G. Guan, Bifunctional ionic liquid and conducting ceramic co-assisted solid polymer electrolyte membrane for quasi-solid-state lithium metal batteries, *J. Membr. Sci.* 586 (2019) 122-129.
- [18] Z. Wu, Z. Xie, A. Yoshida, Z. Wang, X. Hao, A. Abudula, G. Guan, Utmost limits of various solid electrolytes in all-solid-state lithium batteries: A critical review, *Renewable Sustainable Energy Rev.* 109 (2019) 367-385.
- [19] F. Mizuno, A. Hayashi, K. Tadanaga, M. Tatsumisago, New lithium-ion conducting crystal obtained by crystallization of the Li_2S – P_2S_5 glasses, *Electrochem. Solid-State Lett.* 8 (2005) A603-A606.
- [20] T. Ohtomo, A. Hayashi, M. Tatsumisago, Y. Tsuchida, S. Hama, K. Kawamoto, All-solid-state lithium secondary batteries using the $75\text{Li}_2\text{S} \cdot 25\text{P}_2\text{S}_5$ glass and the $70\text{Li}_2\text{S} \cdot 30\text{P}_2\text{S}_5$ glass–ceramic as SEs, *J. Power Sources* 233 (2013) 231-235.
- [21] F. Mizuno, A. Hayashi, K. Tadanaga, M. Tatsumisago, New, highly ion–conductive crystals precipitated from Li_2S – P_2S_5 glasses, *Adv. Mater.* 17 (2005) 918-921.
- [22] W. Richards, L. Miara, Y. Wang, J. Kim, G. Ceder, Interface stability in solid-state batteries, *Chem. Mater.* 28 (2015) 266-273.

- [23] F. Han, T. Gao, Y. Zhu, K. Gaskell, C. Wang, A battery made from a single material, *Adv. Mater.* 27 (2015) 3473-3483.
- [24] A. Sakuda, A. Hayashi, M. Tatsumisago, Interfacial observation between LiCoO_2 electrode and $\text{Li}_2\text{S-P}_2\text{S}_5$ SEs of all-solid-state lithium secondary batteries using transmission electron microscopy, *Chem. Mater.* 22 (2009) 949-956.
- [25] K. Takada, Interfacial nanoarchitectonics for solid-state lithium batteries, *Langmuir* 29 (2013) 7538-7541.
- [26] Y. Shao, H. Wang, Z. Gong, D. Wang, B. Zheng, J. Zhu, Y. Lu, Y. Hu, X. Guo, H. Li, X. Huang, Y. Yong, C. Nan, L. Chen, Drawing a soft interface: an effective interfacial modification strategy for garnet-type solid-state Li batteries, *ACS Energy Lett.* 3 (2018) 1212-1218.
- [27] D. Wang, G. Zhong, W. Pang, Z. Guo, Y. Li, M. McDonald, R. Fu, J. Mi, Y. Yang, Toward understanding the lithium transport mechanism in garnet-type SEs: Li^+ ion exchanges and their mobility at octahedral/tetrahedral sites, *Chem. Mater.* 27 (2015) 6650-6659.
- [28] W. Zhao, G. Zheng, M. Lin, W. Zhao, D. Li, X. Guan, Y. Ji, G. Ortiz, Y. Yang, Toward a stable solid-electrolyte-interfaces on nickel-rich cathodes: LiPO_2F_2 salt-type additive and its working mechanism for $\text{LiNi}_{0.5}\text{Mn}_{0.25}\text{Co}_{0.25}\text{O}_2$ cathodes, *J. Power Sources* 380 (2018) 149-157.
- [29] R. Xu, X. Xia, X. Wang, Y. Xia, J. Tu, Tailored $\text{Li}_2\text{S-P}_2\text{S}_5$ glass-ceramic electrolyte by MoS_2 doping, possessing high ionic conductivity for all-solid-state lithium-sulfur batteries, *J. Mater. Chem. A* 5 (2017) 2829-2834.

- [30] T. Ohtomo, A. Hayashi, M. Tatsumisago, K. Kawamoto, All-solid-state batteries with $\text{Li}_2\text{O-Li}_2\text{S-P}_2\text{S}_5$ glass electrolytes synthesized by two-step mechanical milling, *J. Solid State Electrochem.* 17 (2013) 2551-2557.
- [31] B. Huang, X. Yao, Z. Huang, Y. Guan, Y. Jin, X. Xu, Li_3PO_4 -doped $\text{Li}_7\text{P}_3\text{S}_{11}$ glass-ceramic electrolytes with enhanced lithium ion conductivities and application in all-solid-state batteries, *J. Power Sources* 284 (2015) 206-211.
- [32] R. Xu, X. Xia, S. Li, S. Zhang, X. Wang, J. Tu, All-solid-state lithium–sulfur batteries based on a newly designed $\text{Li}_7\text{P}_{2.9}\text{Mn}_{0.1}\text{S}_{10.7}\text{I}_{0.3}$ superionic conductor, *J. Mater. Chem. A* 5 (2017) 6310-6317.
- [33] Y. Wei, Y. Tao, Z. Kong, L. Liu, J. Wang, W. Qiao, L. Ling, D. Long, Unique electrochemical behavior of heterocyclic selenium–sulfur cathode materials in ether-based electrolytes for rechargeable lithium batteries, *Energy Storage Mater.* 5 (2016) 171-179.
- [34] Z. Li, J. Zhang, B. Guan, X. Lou, Mesoporous carbon@titanium nitride hollow spheres as an efficient SeS_2 host for advanced Li– SeS_2 batteries, *Angew. Chem., Int. Ed.* 129 (2017) 16219-16223.
- [35] J. He, W. Lv, Y. Chen, J. Xiong, K. Wen, C. Xu, W. Zhang, Y. Li, W. Qin, W. He, Direct impregnation of SeS_2 into a MOF-derived 3D nanoporous Co–N–C architecture towards superior rechargeable lithium batteries, *J. Mater. Chem. A* 6 (2018) 10466-10473.
- [36] D. Chen, H. Feng, J. Li, Graphene oxide: preparation, functionalization, and electrochemical applications, *Chem Rev.* 112 (2012) 6027-6053.

- [37] N. Kamaya, K. Homma, Y. Yamakawa, M. Hirayama, R. Kanno, M. Yonemura, T. Kamiyama, Y. Kato, S. Hama, K. Kawamoto, A lithium superionic conductor, *Nat. Mater.* 10 (2011) 682.
- [38] G. Liu, D. Xie, X. Wang, X. Yao, S. Chen, R. Xiao, H. Li, X. Xu, High air-stability and superior lithium ion conduction of $\text{Li}_{3+3x}\text{P}_{1-x}\text{Zn}_x\text{S}_{4-x}\text{O}_x$ by aliovalent substitution of ZnO for all-solid-state lithium batteries, *Energy Storage Mater.* 17 (2018) 266-274.
- [39] S. Mo, P. Lu, F. Ding, Z. Xu, J. Liu, X. Liu, Q. Xu, High-temperature performance of all-solid-state battery assembled with 95(0.7Li₂S-0.3P₂S₅)-5Li₃PO₄ glass electrolyte, *Solid State Ionics* 296 (2016) 37-41.
- [40] M. Tachez, J.-P. Malugani, R. Mercier, G. Robert, Ionic conductivity of and phase transition in lithium thiophosphate Li₃PS₄, *Solid State Ionics* 14 (1984) 181-185.
- [41] A. El kharbachi, Y. Hu, K. Yoshida, P. Vajeeston, S. Kim, M.H. Sørby, S.-I. Orimo, H. Fjellvåg, B.C. Hauback, Lithium ionic conduction in composites of Li(BH₄)_{0.75}I_{0.25} and amorphous 0.75Li₂S-0.25P₂S₅ for battery applications, *Electrochim. Acta* 278 (2018) 332-339.
- [42] F. Han, J. Yue, X. Zhu, C. Wang, Suppressing Li dendrite formation in Li₂S-P₂S₅ solid electrolyte by LiI incorporation, *Adv. Energy Mater.* (2018) 1703644.
- [43] H. Chen, C. Wang, W. Dong, W. Lu, Z. Du, L. Chen, Monodispersed sulfur nanoparticles for lithium-sulfur batteries with theoretical performance, *Nano lett.* 15 (2014) 798-802.
- [44] H. Wan, G. Peng, X. Yao, J. Yang, P. Cui, X. Xu, Cu₂ZnSnS₄/graphene nanocomposites for ultrafast, long life all-solid-state lithium batteries using lithium metal anode, *Energy Storage Mater.* 4 (2016) 59-65.

- [45] Z. Wu, W. Ren, L. Wen, L. Gao, J. Zhao, Z. Chen, G. Zhou, F. Li, H. Cheng, Graphene anchored with Co_3O_4 nanoparticles as anode of lithium ion batteries with enhanced reversible capacity and cyclic performance, *ACS nano* 4 (2010) 3187-3194.
- [46] X. Yang, F. Zhang, L. Zhang, T. Zhang, Y. Huang, Y. Chen, A high-performance graphene oxide-doped ion gel as gel polymer electrolyte for all-solid-state supercapacitor applications, *Adv. Funct. Mater.* 23 (2013) 3353-3360.

Chapter 4 Nickel phosphate nanorod-enhanced polyethylene oxide-based composite polymer electrolytes for solid-state lithium batteries

4.1 Introduction

Traditional lithium batteries (LIBs) with liquid electrolytes always have high energy density, good cyclability, and reliability, which have been an excellent choice for energy storage [1-3]. However, liquid electrolytes usually consist of organic solvents, which are flammable and unstable at a high voltage, resulting in severe accidents [4-6]. Recently, solid-state batteries (SSBs) with solid-state electrolytes have attracted much attention due to their high energy density as well as high safety performance [7-13]. To date, various inorganic SEs have been developed for SSBs [14-17]. However, the applications of these inorganic SEs are still in a limited state owing to the lack of stiffness and film processability as well as high interface resistance with electrodes [18-21]. In contrast, solid polymer electrolytes (SPEs) are known to have relatively reliable stability, low interfacial resistance, flexibility, stretchable property, and low fabricating cost [22-26]. However, the low ionic conductivity ($<10^{-6} \text{ S}\cdot\text{cm}^{-1}$) of SPEs at ambient temperature and high-temperature instability restricts their wide utilization [27-29]. Among the developed SPEs, poly(ethylene oxide) (PEO)-based composite SPE is the most attractive one [30, 31]. In particular, the ionic conductivity can be tuned by changing the molar ratio of PEO to lithium salts and the preparation method [31]. To enhance the ionic conductivity and stability of SPEs, various attempts such as doping other materials, crosslinking, and block copolymerization have been tried [32-37]. It is reported that the addition of inorganic

nanomaterials such as Al_2O_3 , ZnAl_2O_4 , BaTiO_3 , TiO_2 , SiO_2 , and montmorillonite (MMT) to the PEO-based SPEs can effectively enhance the ionic conductivity [38-42]. Moreover, sulfide and oxide electrolytes can be used as additive to enhance the performance of SPEs. For examples, the PEO_{18} -LiTFSI-1%LGPS SPE containing 1% $\text{Li}_{10}\text{GeP}_2\text{S}_{12}$ (LGPS) exhibited high ionic conductivities of $1.21 \times 10^{-3} \text{ S} \cdot \text{cm}^{-1}$ at 80°C and $1.18 \times 10^{-5} \text{ S} \cdot \text{cm}^{-1}$ at 25°C [32], and the ionic conductivity of PEO-LiClO₄-LLZO SPE with 52.5% of $\text{Li}_7\text{La}_3\text{Zr}_2\text{O}_{12}$ (LLZO) reached $4.42 \times 10^{-4} \text{ S} \cdot \text{cm}^{-1}$ at 55°C [43]. Furthermore, the incorporation of some fillers could inhibit the crystallization of PEO and weaken the interactions between the lithium ions and the PEO chains for the further improvement of ionic conductivity and the stability of SPEs [6, 27, 44].

Nickel phosphate VSB-5 (Versailles-Santa Barbara-5, $\text{Ni}_{20}[(\text{OH})_{12}(\text{H}_2\text{O})_6][(\text{HPO}_4)_8(\text{PO}_4)_4] \cdot 12\text{H}_2\text{O}$), which was firstly synthesized by Ferrey and Cheetham *et al.*) is a nanoporous material with 24-ring open framework and high thermal stability [45]. It is found that VSB-5 has 1-D channels with a large pore size of 1.1 nm, which could provide the pathway for large molecules and lithium ions [46]. Considering these characteristics, herein, VSB-5 was selected as the filler for PEO-based SPE, and a series of PEO-LiTFSI-x%VSB-5 ($x = 0, 1, 3, 5$, and 10) SPEs were fabricated for the first time using a grinding process followed with a heat treatment way. The effect of VSB-5 addition amount on the crystallinity as well as the ionic conductivity was investigated via X-ray diffraction (XRD) analysis, Fourier transform infrared (FTIR) analysis, scanning electron microscope (SEM) observation, electrochemical impedance spectroscopy (EIS) measurement, and differential scanning calorimetry (DSC) test. Meanwhile, the electrochemical windows of the prepared SPEs were evaluated by linear sweep voltammetry (LSV). Li^+ transference number and the stability with lithium metal were

tested by the Li symmetrical battery. The thermal stability of SPEs was also investigated by thermogravimetric analysis (TGA). Furthermore, the SSBs with the PEO-LiTFSI-x% VSB-5 SPE, LiFePO₄-based cathode, and Li anode were assembled and their electrochemical performances were evaluated.

4.2 Experimental Section

4.2.1 Synthesis of VSB-5 nanorods

VSB-5 nanorods were synthesized by hydrothermal synthesis method. Briefly, 1 mmol of nickel chloride (NiCl₂·6H₂O) and 10 mmol of hexamethylenetetramine (HMT) were dissolved in 25 mL of water at first. It is known that the properties such as particle size and crystallinity are different depending on the synthetic conditions [47]. To obtain a variety of VSB-5 nanorods, varying amounts of disodium hydrogenphosphate (Na₂HPO₄) were added under stirring and meanwhile the pH of the solution was adjusted to 7 or 9 by adding NH₃·H₂O or HCl. After stirring for 30 min, the final gel was kept in a Telfon-lined stainless autoclave and heated in an oven at 140 °C for 8 h. The powder products were washed repeatedly with distilled water, filtered, and dried at 100 °C. Finally, the as-synthesized samples were calcined at 350 °C in air for 1 h.

4.2.2 Fabrications of the cathode and solid polymer electrolyte

PEO (MW = 6×10⁵), LiTFSI, and VSB-5 were completely dried before use. PEO, LiTFSI, and VSB-5 were mixed using an agate mortar to obtain a rough, soft cloth state material. Herein, the amount of LiTFSI was determined by the molar ratio of (EO)/Li⁺ (EO/Li⁺=8), and the quantity of VSB-5 was decided by the mass ratio of VSB-5/LiTFSI-

PEO (0, 1, 3, 5, 10 wt%). The obtained rough sheet film was sealed in the glove box and transferred to a vacuum oven at 80 °C and dried for 12 h. Subsequently, it was pressed under 5 MPa for 2 h, and as such, a uniform composite membrane with a thickness of 80-120 μm was obtained.

For the fabrication of cathode, LiFePO_4 particles, conductive additive super P and polyvinylidene fluoride (PVDF) with a weight ratio of LiFePO_4 :super P:PVDF=8:1:1 were dispersed in a certain amount of N-methyl-2-pyrrolidone (NMP) solvent and stirred for 12 h to get a homogenous slurry, and then the slurry was coated on an Al current collector and dried at 120 °C in vacuum for 12 h.

4.2.3 Characterizations

Differential Scanning Calorimetry (DSC) measurement of the SPE was performed by using a thermal analyzer (SII, DSC 6200, Japan) with a heating rate of $10\text{ }^\circ\text{C}\cdot\text{min}^{-1}$. X-ray diffraction (XRD) pattern was collected in a 2θ range from 10° to 90° on an X-ray diffractometer (Smartlab 9kW, Rigaku, Japan) with the $\text{Cu K}\alpha$ radiation ($\lambda = 1.5406\text{ \AA}$). The morphology was characterized using a scanning electron microscope (SEM) (SU8010, Hitachi, Japan). Thermogravimetric analysis (TGA) was conducted on a TA machine (TA-60WS, SHIMADZU, Japan) to investigate the thermal stability of the SPE. Chemical structures of PEO, LiTFSI, VSB-5, PEO-LiTFSI, PEO-LiTFSI-VSB-5 were determined by the Fourier transform infrared spectrum (FT-IR) (FT/IR-4200, JASCO, Japan).

4.2.4 Electrochemical evaluation

The obtained SPE film was sandwiched by stainless steel foils (SS) to form a SS/SPE/SS battery for the ionic conductivity measurement by using the electrochemical impedance spectroscopy (EIS) (VersaSTAT 4, Princeton Applied Research, USA), in which the temperature was set in a range of 30-100 °C with a frequency range of 10-10⁶ Hz. For measuring Li⁺ transference number (t_{Li}^+) of SPE, the Li/SPE/Li battery with Li foils was assembled, and its DC polarization property was investigated. Herein, a voltage of 10 mV was applied on the battery, and EIS spectra of battery before and after polarization were obtained in a frequency range of 10⁻²-10⁶ Hz. The t_{Li}^+ is calculated based on the following equation:

$$t_{Li}^+ = \frac{I_s(\Delta V - I_0 R_0)}{I_0(\Delta V - I_s R_s)} \quad \text{Eq. (1)}$$

where ΔV is the applied DC polarization voltage (0.01 V), I_0 and I_s are initial and stable currents during the polarization, R_0 and R_s are the resistances of the SPE before and after the polarization. Linear sweep voltammetry (LSV) curves were recorded on the electrochemical workstation in a voltage range of 0-5.5 V by using Li/SPE/SS 2025 cells. The stability of the interface between SPE and Li electrode was examined with Li symmetrical battery by a stripping/plating test at 0.01 mA.

The solid batteries were assembled in 2025-type coin cells with lithium metal anode, PEO-LiTFSI-VSB-5 composite electrolyte and LiFePO₄ cathode. Galvanostatic charge and discharge performances of the solid-state batteries were investigated using a LANHE CT2001A charge/discharge system (Wuhan LAND Electronics Co., Ltd.) in a potential range of 4.0-2.5 V at 60 °C.

4.3 Results and discussion

In order to prepare VSB-5 with suitable morphology, the effect of initial pH as well as $\text{NiCl}_2 \cdot 6\text{H}_2\text{O}/\text{HMT}/\text{NaH}_2\text{PO}_4$ ratio on the morphology of VSB-5 was investigated. As shown in Figure 4.1, the sizes of VSB-5 nanorods were large and inhomogeneous with about 270-320 nm in diameter and several micrometers in length as it was prepared with a $\text{NiCl}_2 \cdot 6\text{H}_2\text{O}:\text{HMT}:\text{NaH}_2\text{PO}_4$ molar ratio of 1:10:5 at pH = 7 (Figure 4.1A). Meanwhile, when the pH was increased to 9, a mixture of flower-like particles was obtained (Figure 4.1B). However, when the $\text{NiCl}_2 \cdot 6\text{H}_2\text{O}/\text{HMT}/\text{NaH}_2\text{PO}_4$ ratio was changed from 1:10:5 to 1:10:15 (Figs. 1C-D), the rods became thinner (as compared to Figure 4.1A), and at pH = 7, the VSB-5 nanorods had a diameter in the range of 180-220 nm with different lengths. In contrast, as pH = 9, the VSB-5 nanorods became thinner with a uniform size, which had a diameter of approximately 100 nm, and a length of 3 μm (Figure 4.1D). Herein, the flower-like VSB-5 particles were only observed from the SEM image as the molar ratio of $\text{NiCl}_2 \cdot 6\text{H}_2\text{O}:\text{HMT}:\text{NaH}_2\text{PO}_4 = 1:10:5$ at pH = 9. In general, the aligned nanorods could provide channels for the fast ion transport owing to no crossing junctions [6, 27, 44]. Therefore, the VSB-5 nanorods prepared with the $\text{NiCl}_2 \cdot 6\text{H}_2\text{O}:\text{HMT}:\text{NaH}_2\text{PO}_4$ molar ratio of 1:10:15 at pH = 9 was selected for further studies in this work.

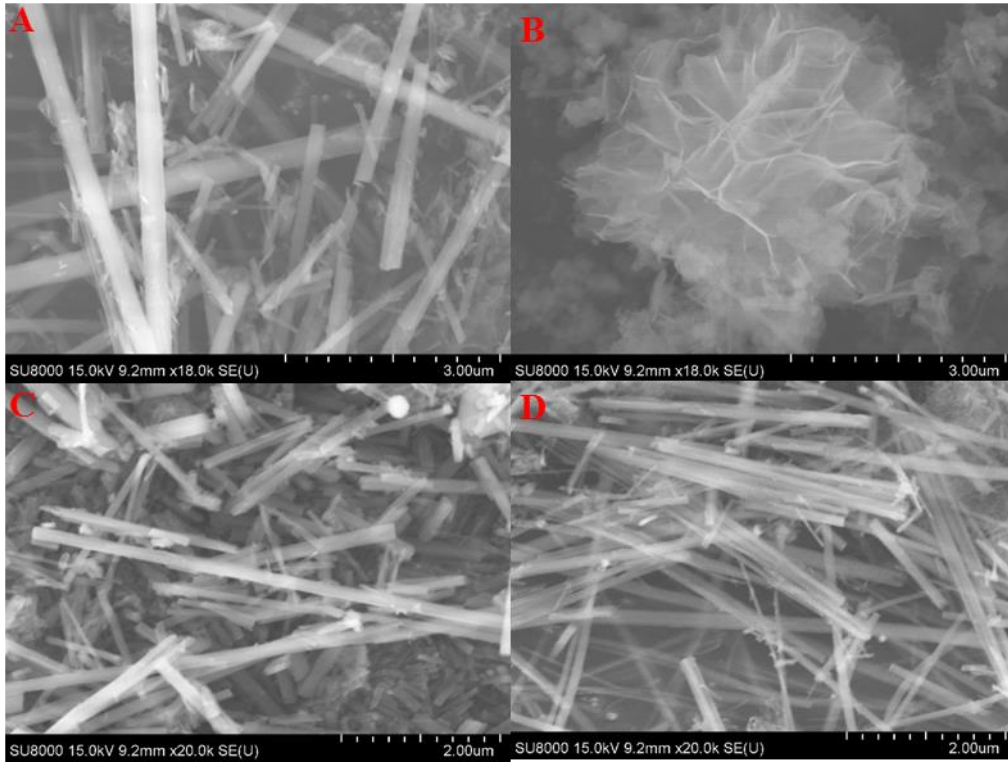


Figure 4.1 SEM images of VSB-5 (A) pH=7 (MR= 1:10:5) (B) pH=9 (MR= 1:10:5) (C) pH=7 (MR= 1:10:15) (D) pH=9 (MR= 1:10:15), MR: molar ratio of $\text{NiCl}_2 \cdot 6\text{H}_2\text{O}:\text{HMT}:\text{NaH}_2\text{PO}_4$.

The electrochemical impedance spectroscopies of SPEs with different VSB-5 addition amounts, i.e., PEO-LiTFSI-x% VSB-5 ($x = 0, 1, 3, 5$, and 10) using the SS/SPE/SS batteries were measured in a frequency range of $10\text{--}10^6$ Hz at a temperature range $30\text{--}100$ °C. As shown in Figure 4.2, a semicircle and a spike were observed in the high- and low-frequency ranges, respectively, for each battery. The semicircle represents the bulk resistance of SPE and the interfacial resistance between the SPE and SS electrode, and the spike is resulted from the ion diffusion impedance in the electrode. As such, the ionic conductivity value (σ) can be calculated from the intercept of the spike using the following equation:

$$\sigma = \frac{d}{R \times S} \quad \text{Eq. (2)}$$

where σ , d , R , and S are the ionic conductivity, the thickness, the volume impedance, and the surface area of the SPE, respectively. From Figure 4.2, one can see that the ionic conductivity increased after VSB-5 was introduced into the PEO-LiTFSI SPE. The calculation results based on eq. (2) indicated that the PEO-LiTFSI-3%VSB-5 had the highest ionic conductivity of $4.83 \times 10^{-5} \text{ S} \cdot \text{cm}^{-1}$ at 30°C , which is approximately three times higher than that ($1.52 \times 10^{-5} \text{ S} \cdot \text{cm}^{-1}$ at 30°C) of the PEO-LiTFSI SPE. With further increase in VSB-5 addition amount, the ionic conductivity of PEO-LiTFSI-x%VSB-5 began to decrease. Herein, the excessive VSB-5 nanorods filling in polymer matrix could lead to the aggregation and free-volume depletion of the nanorods, which would cause a decrease of ionic conductivity [6, 44, 48]. Therefore, the PEO-LiTFSI-3%VSB-5 SPE was selected as the optimized SPE for further study.

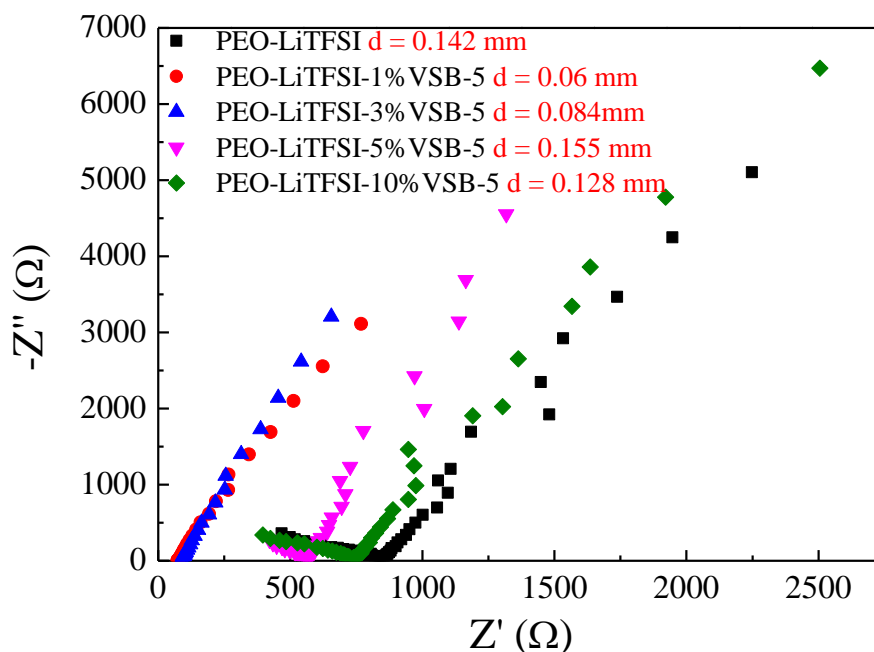


Figure 4.2 EISs of PEO-LiTFSI- $x\%$ VSB-5 ($x = 0, 1, 3, 5$, and 10) at $30\text{ }^{\circ}\text{C}$. d : Thickness.

Figure 4.3A shows XRD patterns of the PEO-LiTFSI- $x\%$ VSB-5 ($x = 0, 1, 3, 5$, and 10) SPEs. The regions of pure PEO appearing between $2\theta = 15.1^{\circ}$ to 30.2° exhibited the amorphous phase of PEO whereas the peaks at $2\theta = 19.6^{\circ}$, 23.8° , 26.7° , and 27.4° corresponded to the crystalline phase of PEO. The simultaneous presences of halo region and crystalline peaks indicate the semi crystalline nature of PEO [49, 50]. Two apparent different diffraction peaks at 11.1° and 14.6° were observed for the PEO-LiTFSI electrolyte [51], which caused local depletion of the lithium ions in the PEO amorphous phase. As VSB-5 was added into PEO-LiTFSI electrolyte, the diffraction peaks of VSB-5 became very weak. Figure 4.3B shows the high-resolution XRD pattern of PEO-LiTFSI-3% VSB-5 SPE. Weak diffraction peaks corresponding to VSB-5 were observed. As shown in Figure 4.3A, the intensity of the PEO peaks was decreased, and the halo

region of PEO-LiTFSI-x% VSB-5 was broadened with the increase of x (x = 1, 3, 5, and 10), indicating the decrease of PEO crystallinity and the increase of PEO amorphous phase, which could enhance the ion conductivity of such SPEs.

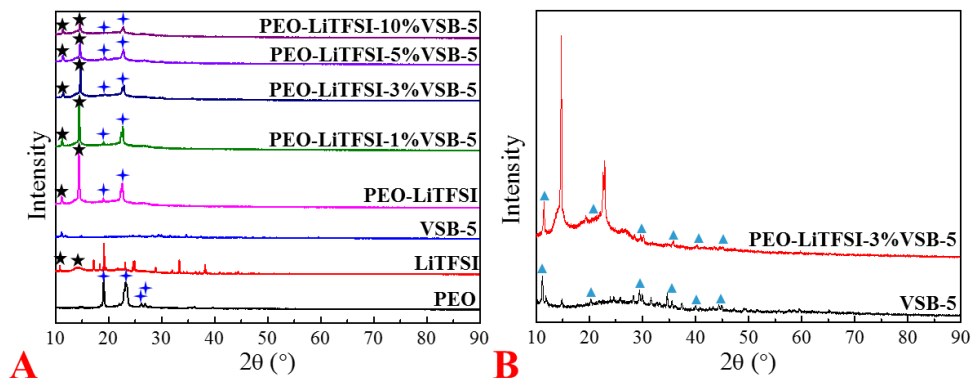


Figure 4.3 XRD (A) of the PEO-LiTFSI-x% VSB-5 (x = 0, 1, 3, 5, and 10) and high-resolution XRD (B) of VSB-5 and PEO-LiTFSI-3% VSB-5.

Figure 4.4A illustrates the interactions between different components including PEO, LiTFSI, and VSB-5. Herein, the VSB-5 nanorods could interact with TFSI⁻ anion in the lithium salt and weaken the interaction between Li⁺ and TFSI⁻ so that Li⁺ movement in the electrolyte becomes more easily. Meanwhile, the VSB-5 nanorods could interact with PEO to alter the polymer arrangement and/or crystallinity. In addition, the nanostructure of VSB-5 could provide rich Li⁺ transport channels. All of these could increase the whole ionic conductivity. Figure 4.4B shows the FTIR spectra of PEO, VSB-5, LiTFSI, and PEO-LiTFSI-x% VSB-5 (x = 0, 1, 3, 5, and 10) in the wavenumber range from 4000 to 400 cm⁻¹. Herein, the peaks at 1203 and 797 cm⁻¹ are assigned to the -CF₃ bonds of LiTFSI [52] and the characteristic peaks at 2887 cm⁻¹, 1467 cm⁻¹, 1343 cm⁻¹, 1244 cm⁻¹, 964 cm⁻¹, and 839 cm⁻¹ belong to PEO. The band observed at the 839 cm⁻¹ is associated with the CH₂ rocking mode and/or the C-O stretching mode; the band located at the 964

cm^{-1} is attributed to the symm-asymp C-O-C stretching mode; and the band observed at the 1244 cm^{-1} , 1343 cm^{-1} and 1467 cm^{-1} corresponds to the asymmetric CH_2 twisting, CH_2 bending/wagging, and C-H bending respectively [53]. Figure 4.4C shows the magnification spectra in the range of $1500\text{--}900\text{ cm}^{-1}$. The peaks centered at 1146 cm^{-1} , 1329 cm^{-1} , and 957 cm^{-1} are attributed to asymmetric $\text{-SO}_2\text{-}$ stretching in the PEO-LiTFSI electrolyte. However, these peaks shifted to 1140 cm^{-1} , 1331 cm^{-1} , and 952 cm^{-1} respectively with the addition of VSB-5, indicating the interaction between VSB-5 nanorod and the $\text{-SO}_2\text{-}$ group in the TFSI⁻ [6]. In addition, one can see that the addition of the VSB-5 also reduced the intensity of peaks related to the PEO. Herein, VSB-5 has active P-OH groups on the channel surface [54], and PEO has C-O groups based on the FTIR analysis result. As such, VSB-5 could be connected with PEO via H-OH hydrogen bonds. The intermolecular hydrogen bonding effect between PEO and VSB-5 enables polymer chains to be more disordered in the SPE and change the polymer arrangement and/or decreased its crystallinity. The intrinsically increased disorder and amorphous content of the polymer chains could also enhance the Li^+ transmission by releasing more Li cations and further improved ionic conductivity [6]. These are in agreement with the XRD results.

Differential scanning calorimetry (DSC) was carried out to analyze the thermal behavior of PEO-LiTFSI-x%VSB-5 ($x = 0, 1, 3, 5$, and 10) electrolytes. As shown in Figure 4.5A, the melting transition of PEO-LiTFSI was near $53.6\text{ }^\circ\text{C}$. With the addition of VSB-5, the melting transition of PEO-LiTFSI-3%VSB-5 electrolyte decreased to nearly $49.2\text{ }^\circ\text{C}$ while the peak area also decreased significantly. Generally, the lower melting point and peak area mean a lower degree of crystallinity [55]. Thus, it confirmed that the addition VSB-5 in the SPE effectively decreased the crystallinity of PEO and

increased PEO segmental mobility, which should be benefit for the improvement of ionic conductivity as stated above. This is also in agreement well with the XRD results.

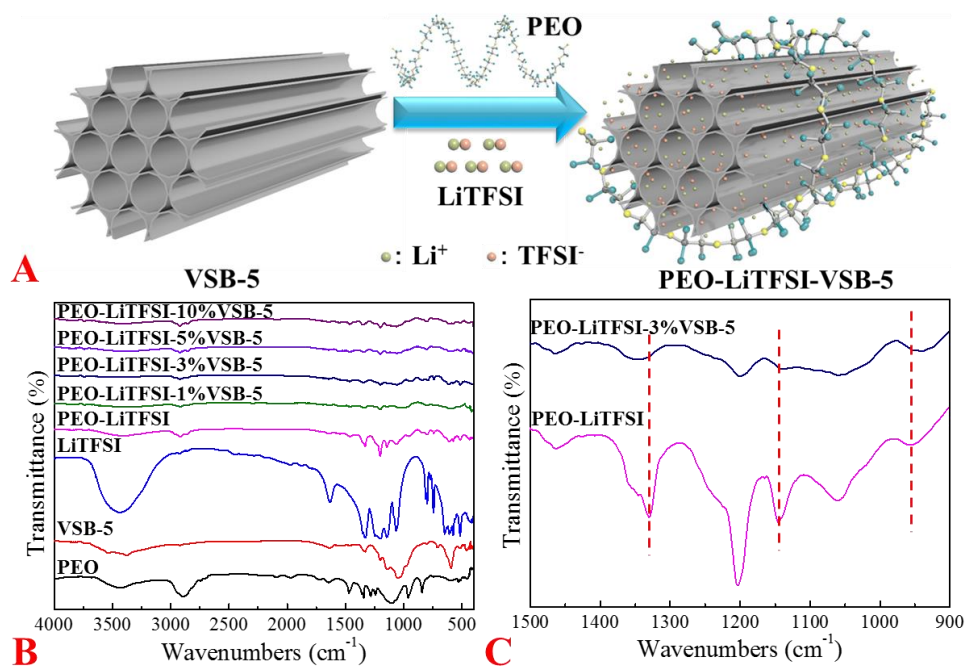


Figure 4.4 Schematic (A) of Li^+ migration in VSB-5 enhanced composite SPEs, FTIR (B) of the PEO-LiTFSI- $x\%$ VSB-5 ($x = 0, 1, 3, 5$, and 10) and the magnification (C) of FTIR in the wavenumber range of $1500\text{--}900\text{ cm}^{-1}$.

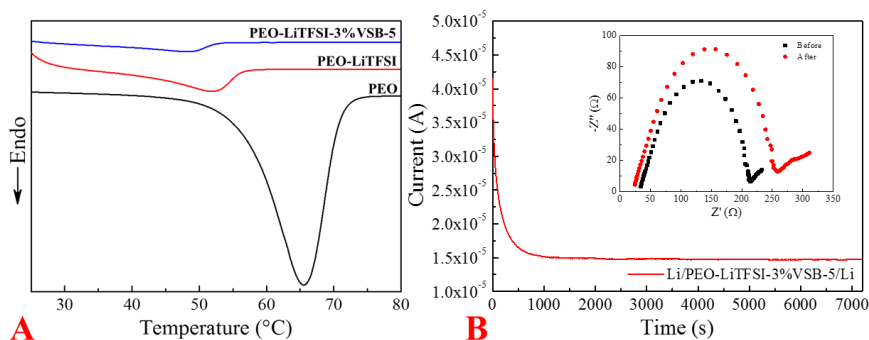


Figure 4.5 DSC (A) of the PEO, PEO-LiTFSI and PEO-LiTFSI-3% VSB-5 and the EIS (B) of the Li/PEO-LiTFSI-3%VSB-5/Li.

and chronoamperometry curves (B) of a Li/SPE/Li cell under a potential step of 10 mV.

To confirm the effect of VSB-5 addition on the migration of Li^+ in PEO-LiTFSI electrolyte, the lithium ion transference number (t_{Li}^+) of PEO-LiTFSI-3%VSB-5 electrolyte was also calculated by Eq. (1) based on the measurement results of chronoamperometry (Figure 4.5B). As a result, the t_{Li}^+ of PEO-LiTFSI-3%VSB-5 electrolyte was 0.13, indicating that the t_{Li}^+ can be effectively improved by the addition of VSB-5.

The electrochemical operation windows of the fabricated SPEs were examined by the LSVs of the SS/SPE/Li batteries. As shown in Figure 4.6A, the electrochemical window of PEO-LiTFSI-3%VSB-5 electrolyte was nearly 4.08 V, which was higher than that of the PEO-LiTFSI electrolyte (4.13 V), suggesting that the addition of VSB-5 effectively protected the PEO matrix from side reactions [56]. Meanwhile, the thermal stability of PEO-LiTFSI-3%VSB-5 electrolyte was also tested by TGA. As shown in Figure 4.7, the obvious weight loss was observed at a temperature range of around 340-390 °C in the case of PEO-LiTFSI-3%VSB-5 electrolyte, which should be mainly attributed to the partly decomposition of PEO and the loss of bound water in the VSB-5, and the continuous weight loss occurred in the temperature range of 360-590 °C should be resulted from the complete decomposition of PEO and LiTFSI [6]. Finally, the residual weights of PEO-LiTFSI-3%VSB-5 and PEO-LiTFSI electrolytes after 660 °C were about 7.0 wt% and 4.8 wt%, respectively.

Besides electrochemical and thermal stability, the interface stability of PEO-LiTFSI-3%VSB-5 electrolyte with the Li foil electrode was also analyzed by galvanostatic cycling test of the Li/SPE/Li batteries with a constant current of 0.1 mA at 60 °C. As

shown in Figure 4.6B, the Li plating and stripping over-potential of the PEO-LiTFSI-3% VSB-5 electrolyte was near 40 mV and maintained stable for 480 h, indicating good compatibility between PEO-LiTFSI-3% VSB-5 electrolyte and Li electrode. In contrast, the battery with the PEO-LiTFSI electrolyte had a higher overpotential of 80 mV at the first 70 h, and suddenly the battery got short-circuited. Thus, the addition of VSB-5 in the PEO-LiTFSI electrolyte resulted in good compatibility with Li metal and exhibited a positive effect on inhibiting the uncontrollable formation and growth of Li dendrite.

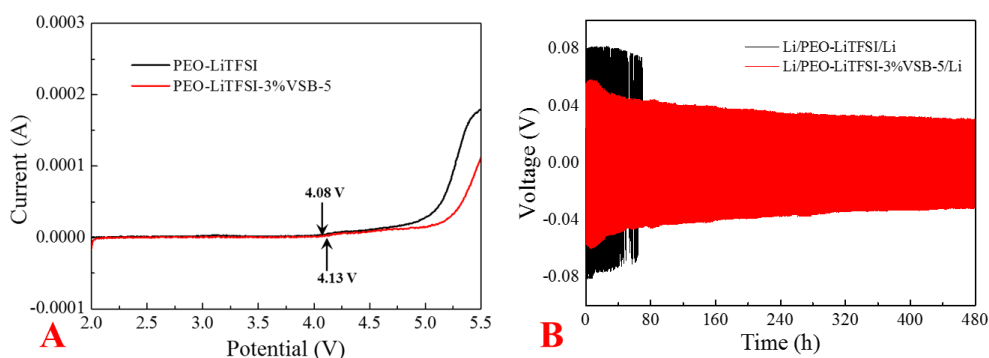


Figure 4.6 LSVs (A) of the PEO-LiTFSI and PEO-LiTFSI-3% VSB-5 SPEs under a scan rate of $1 \text{ mV} \cdot \text{s}^{-1}$ and voltage-time profiles (B) of Li metal plating and stripping in Li/SPE/Li cells at 0.1 mA.

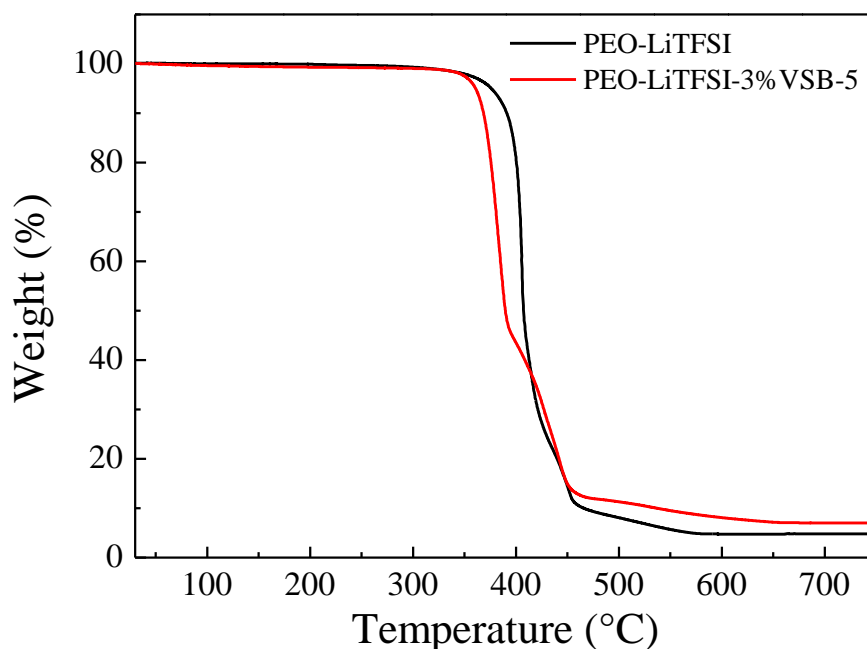


Figure 4.7 TGA curves of the PEO-LiTFSI and PEO-LiTFSI-3%VSB-5 electrolytes.

The microstructure and elemental distribution were also characterized by SEM and EDS (F, S, P and Ni). As shown in Figure 4.8A, smooth surface morphology of PEO-LiTFSI-3% VSB-5 SPE was observed, indicating the satisfactory miscibility between the PEO-LiTFSI and VSB-5. Meanwhile, as shown in Figure 4.8B, the distributions of P and Ni almost overlapped with the signals of F and S, indicating that VSB-5 was homogeneously dispersed in the PEO-LiTFSI-3% VSB-5 electrolyte. As shown in Figure 4.9, PEO and VSB-5 were clearly observed, in which the PEO had a block-like structure and VSB-5 was still in the nanorod-like state without any changes. Moreover, Figure 4.10 shows TEM images of the PEO and PEO-VSB-5. It is obvious that the PEO was composed of nanoparticles (Figure 4.10A and B) and VSB-5 nanorods combined well with PEO in the PEO-VSB-5, also indicating the good compatibility between PEO and VSB-5.

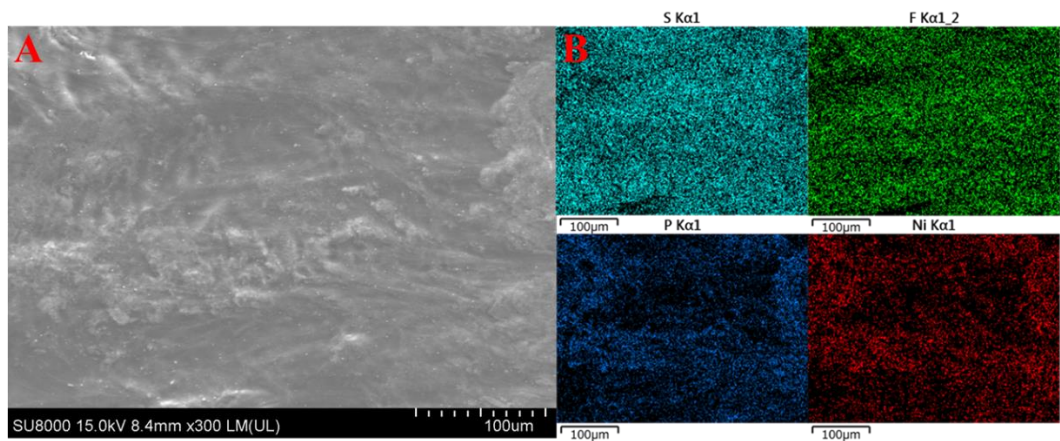


Figure 4.8 SEM (A) and EDS mapping (B) of the PEO-LiTFSI-3%VSB-5 electrolyte.

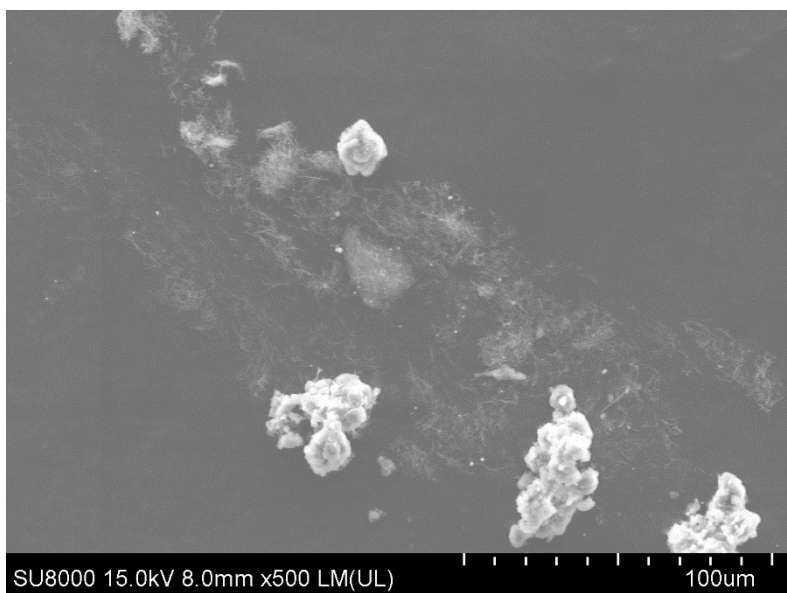


Figure 4.9 SEM image of the PEO-VSB-5.

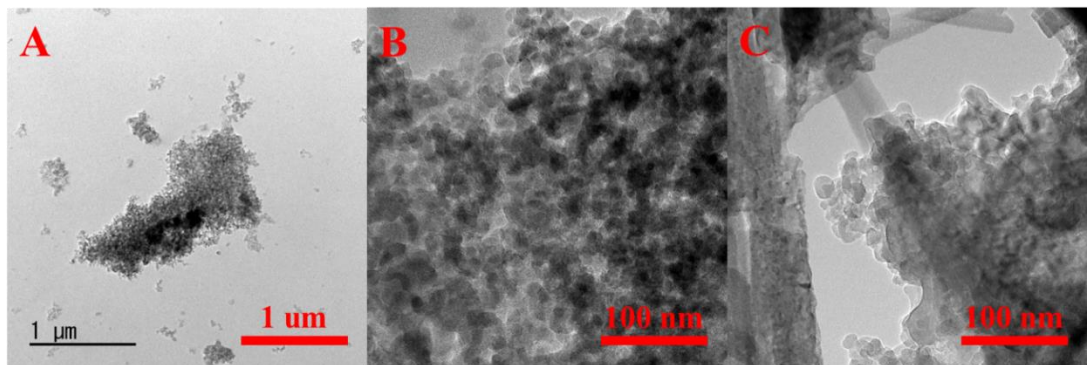


Figure 4.10 TEM images of PEO (A-B) and PEO-VSB-5 (C).

To evaluate the cycle stability, the batteries were tested in the charge/discharge cycling with a cut-off potential range of 2.5 to 4 V (vs Li/Li⁺). The cycling performance of LiFePO₄/SPE/Li at 0.2 C and 60 °C is presented in Figure 4.11A. One can see that the discharge capacity decreased with the increase in the discharge-charge cycle number. The discharge capacity of the LiFePO₄/PEO-LiTFSI/Li battery decreased to 126.6 mAh·g⁻¹ after the 50-cycle test. In contrast, the discharge capacity of the LiFePO₄/PEO-LiTFSI-3%VSB-5/Li battery was still 157.4 mAh·g⁻¹ after the 50-cycle test. In addition, the coulombic efficiency of LiFePO₄/PEO-LiTFSI-3%VSB-5/Li battery was still stable at more than 99% whereas that of LiFePO₄/PEO-LiTFSI/Li battery had fluctuated and decreased after 43 cycles. Figure 4.11B shows the rate performances of the SSBs based on PEO-LiTFSI and PEO-LiTFSI-3%VSB-5 SPEs and Li anode. The LiFePO₄/PEO-LiTFSI-3%VSB-5/Li battery delivered the discharge capacities of 140.4, 139.4, 134.9, 127.8 and 136.4 mAh·g⁻¹ at rates of 0.1, 0.3, 0.5, 1 and 0.1 C, respectively. When the rate was returned to 0.1 C, the discharge capacity maintained as high as 97.2% of the initial value. In contrast, the discharge capacities of LiFePO₄/PEO-LiTFSI/Li battery were 111.8, 124.9, 119.1, 98.2 and 130.1 mAh·g⁻¹ at 0.1, 0.3, 0.5, 1 and 0.1 C, respectively. The PEO-LiTFSI-3%VSB-5 SPEs could improve the capacity of solid battery. Thus, the addition of VSB-5 enhanced the cycle stability as well as capacity maintaining ability due to the improved Li⁺ conductivity, higher stability with lithium, and the lower interface resistance between the electrode and SPE.

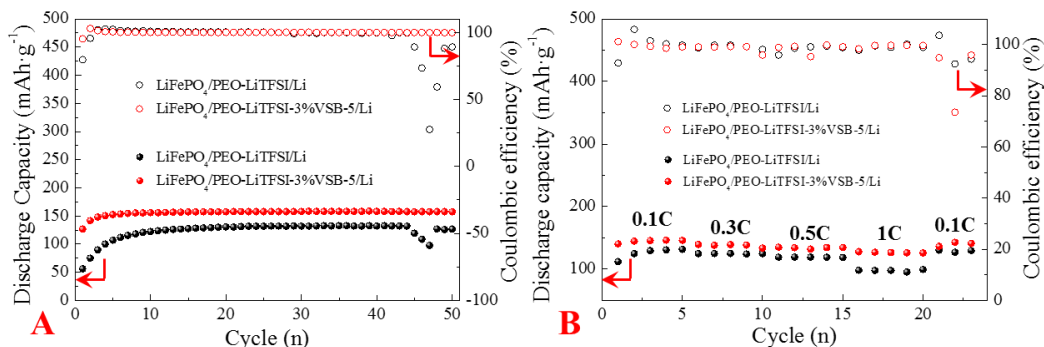


Figure 4.11 (A) Cycling performances of LiFePO₄/PEO-LiTFSI/Li and LiFePO₄/PEO-LiTFSI-3% VSB-5/Li batteries at 0.2 C and 60 °C. (C) Rate performances of LiFePO₄/PEO-LiTFSI/Li and LiFePO₄/PEO-LiTFSI-3% VSB-5/Li batteries at 60 °C.

The interface images between the SPE and the Li electrode were observed by SEM. Figure 4.12A and C show the sandwich structures of the two LiFePO₄/PEO-LiTFSI/Li and LiFePO₄/PEO-LiTFSI-3% VSB-5/Li batteries, in which the thicknesses of the SPEs were in the range of 30-50 μm. However, as shown in Figure 4.12B, after the cycling test at 60 °C, in the case using the PEO-LiTFSI SPE, the Li anode exhibited an uneven surface with massive Li dendrites. In contrast, a relatively flat surface was observed on the Li anode when PEO-LiTFSI-3% VSB-5 SPE was used (Figure 4.12D). It demonstrated that the PEO-LiTFSI-3% VSB-5 SPE should be more favorable to inhibit the growth of Li dendrites. Thus, the addition of VSB-5 nanorods can effectively suppress Li dendrite formation.

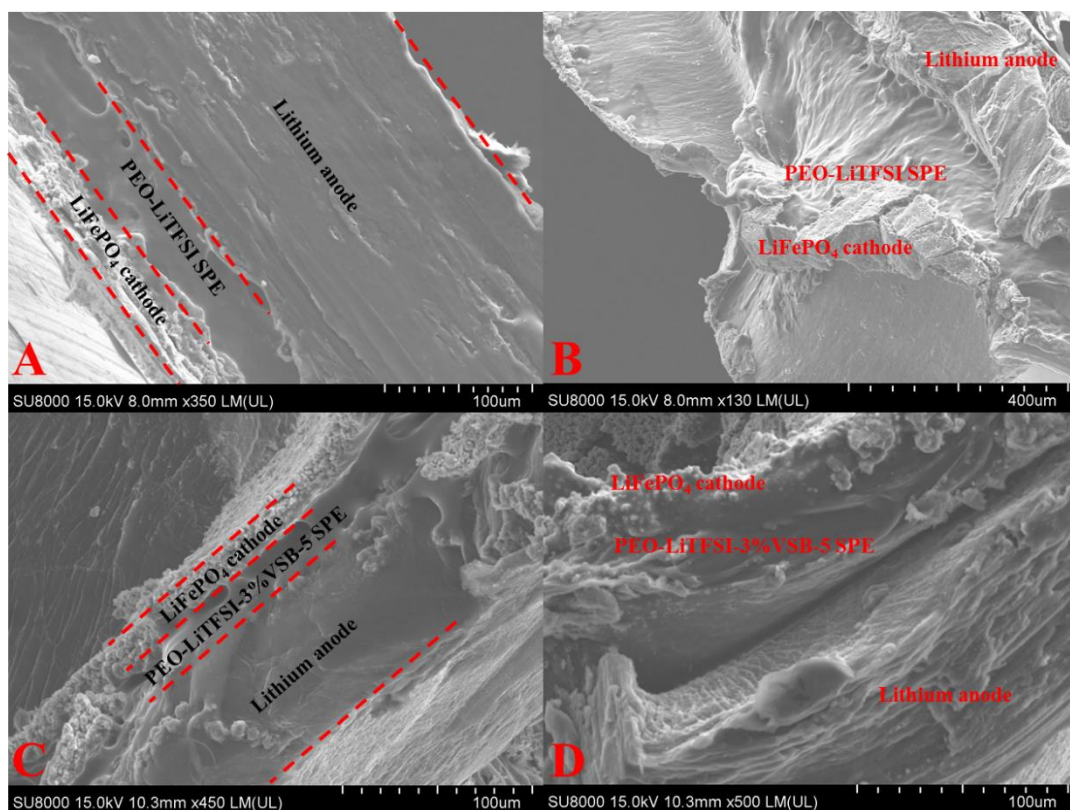


Figure 4.12 Cross-section and interface images of LiFePO₄/PEO-LiTFSI/Li battery (A-B) and LiFePO₄/PEO-LiTFSI-3% VSB-5/Li battery (C-D) after the rate cycling test.

4.4 Conclusions

In summary, VSB-5 nanorods with a thin and uniform size were successfully prepared by the hydrothermal synthesis method and used as the filler in the PEO-LiTFSI SPE for SSBs. The addition of VSB-5 in PEO-LiTFSI SPE effectively improved the thermal stability, lithium stability, ionic conductivity, interfacial stability, and operation electrochemical window. As a result, the ionic conductivity of PEO-LiTFSI-3% VSB-5 reached 4.83×10^{-5} at 30 °C with a widened electrochemical stability window up to 4.13 V vs. Li/Li⁺. It is found that the high ionic conductivity of PEO-LiTFSI-3% VSB-5 was resulted from not only the interaction between the VSB-5 nanorod and -SO₂- in the TFSI,

which could promote the transport ability of Li^+ , but also the interaction between the VSB-5 nanorod and the PEO, which significantly reduced the glass transition temperature and degree of crystallinity of PEO-LiTFSI-3% VSB-5 SPE so that the ionic conductivity was also enhanced. Furthermore, the $\text{LiFePO}_4/\text{PEO-LiTFSI-3\% VSB-5/Li}$ battery exhibited the improved cyclic performance as well as the rate capability compared with the $\text{LiFePO}_4/\text{PEO-LiTFSI/Li}$ battery due to the suppression effect of lithium dendrites and high ionic conductivity of PEO-LiTFSI-3% VSB-5 SPE. It is demonstrated that this new solid polymer composite electrolyte should be a promising electrolyte applied in the solid-state batteries with lithium metal electrode.

References

- [1] J. Lu, Z. Chen, Z. Ma, F. Pan, L.A. Curtiss, K. Amine, The role of nanotechnology in the development of battery materials for electric vehicles, *Nat. Nanotechnol.* 11 (2016) 1031.
- [2] Y. Lu, Z. Tu, L.A. Archer, Stable lithium electrodeposition in liquid and nanoporous SEs, *Nat. Mater.* 13 (2014) 961.
- [3] Y. Tao, G. Zeng, C. Xiao, Y. Liu, Y. Qian, J. Feng, Porosity controlled synthesis of nanoporous silicon by chemical dealloying as anode for high energy lithium-ion batteries, *J. Colloid Interface Sci.* 554 (2019) 674-681.
- [4] B. Scrosati, J. Garche, Lithium batteries: status, prospects and future, *J. Power Sources* 195 (2010) 2419-2430.

- [5] J.B. Goodenough, Y. Kim, Challenges for rechargeable Li batteries, *Chem. Mater.* 22 (2009) 587-603.
- [6] O. Sheng, C. Jin, J. Luo, H. Yuan, H. Huang, Y. Gan, J. Zhang, Y. Xia, C. Liang, W. Zhang, $\text{Mg}_2\text{B}_2\text{O}_5$ nanowire enabled multifunctional solid-state electrolytes with high ionic conductivity, excellent mechanical properties, and flame-retardant performance, *Nano Lett.* 18 (2018) 3104-3112.
- [7] N. Kamaya, K. Homma, Y. Yamakawa, M. Hirayama, R. Kanno, M. Yonemura, T. Kamiyama, Y. Kato, S. Hama, K. Kawamoto, A. Mitsui, A lithium superionic conductor, *Nat. Mater.* 10 (2011) 682-686.
- [8] Y. Wang, W.D. Richards, S.P. Ong, L.J. Miara, J.C. Kim, Y. Mo, G. Ceder, Design principles for solid-state lithium superionic conductors, *Nat. Mater.* 14 (2015) 1026-1031.
- [9] X. Liu, K. Zhao, Z.L. Wang, Y. Yang, Unity convoluted design of solid Li-ion battery and triboelectric nanogenerator for self-powered wearable electronics, *Adv. Energy Mater.* 7 (2017) 1701629.
- [10] W. Zhang, J. Nie, F. Li, Z. Wang, C. Sun, A durable and safe solid-state lithium battery with a hybrid electrolyte membrane, *Nano Energy* 45 (2018) 413-419.
- [11] Y. Zhang, J. Lai, Y. Gong, Y. Hu, J. Liu, C. Sun, Z. Wang, A safe high-performance all-solid-state lithium-vanadium battery with a freestanding V_2O_5 nanowire composite paper cathode, *ACS Appl. Mater. Interfaces* 8 (2016) 34309-34316.
- [12] L. Xu, S. Tang, Y. Cheng, K. Wang, J. Liang, C. Liu, Y. Cao, F. Wei, L. Mai, Interfaces in solid-state lithium batteries, *Joule* 2 (2018) 1991-2015.

- [13] S. Xin, Y. You, S. Wang, H. Gao, Y. Yin, Y. Guo, Solid-state lithium metal batteries promoted by nanotechnology: progress and prospects, *ACS Energy Lett.* 2 (2017) 1385-1394.
- [14] J.C. Bachman, S. Muy, A. Grimaud, H.H. Chang, N. Pour, S.F. Lux, O. Paschos, F. Maglia, S. Lupart, P. Lamp, L. Giordano, Y. Shao-Horn, Inorganic solid-state electrolytes for lithium batteries: mechanisms and properties governing ion conduction, *Chem. Rev.* 116 (2016) 140-162.
- [15] R. Xu, F. Han, X. Ji, X. Fan, J. Tu, C. Wang, Interface engineering of sulfide electrolytes for all-solid-state lithium batteries, *Nano Energy* 53 (2018) 958-966.
- [16] R. Xu, S. Zhang, X. Wang, Y. Xia, X. Xia, J. Wu, C. Gu, J. Tu, Recent developments of all-solid-state lithium secondary batteries with sulfide inorganic electrolytes, *Chem. - Eur. J.* 24 (2018) 6007-6018.
- [17] Z. Wu, Z. Xie, A. Yoshida, X. An, Z. Wang, X. Hao, A. Abudula, G. Guan, Novel SeS_2 doped $\text{Li}_2\text{S-P}_2\text{S}_5$ solid electrolyte with high ionic conductivity for all-solid-state lithium sulfur batteries, *Chem. Eng. J.* 380 (2020) 122419.
- [18] W. Luo, Y. Gong, Y. Zhu, Y. Li, Y. Yao, Y. Zhang, K. Fu, G. Pastel, C.F. Lin, Y. Mo, E.D. Wachsman, L. Hu, Reducing interfacial resistance between garnet-structured solid-state electrolyte and Li-metal anode by a germanium layer, *Adv. Mater.* 29 (2017) 1606042.
- [19] C. Wang, Y. Gong, B. Liu, K. Fu, Y. Yao, E. Hitz, Y. Li, J. Dai, S. Xu, W. Luo, Conformal, nanoscale ZnO surface modification of garnet-based solid-state electrolyte for lithium metal anodes, *Nano Lett.* 17 (2016) 565-571.

- [20] S. Zekoll, C. Marriner-Edwards, A.O. Hekselman, J. Kasemchainan, C. Kuss, D.E. Armstrong, D. Cai, R.J. Wallace, F.H. Richter, J.H. Thijssen, Hybrid electrolytes with 3D bicontinuous ordered ceramic and polymer microchannels for all-solid-state batteries, *Energy Environ. Sci.* 11 (2018) 185-201.
- [21] N. Kamaya, K. Homma, Y. Yamakawa, M. Hirayama, R. Kanno, M. Yonemura, T. Kamiyama, Y. Kato, S. Hama, K. Kawamoto, A lithium superionic conductor, *Nat. Mater.* 10 (2011) 682-686.
- [22] M. Liu, D. Zhou, Y.-B. He, Y. Fu, X. Qin, C. Miao, H. Du, B. Li, Q.-H. Yang, Z. Lin, Novel gel polymer electrolyte for high-performance lithium–sulfur batteries, *Nano Energy* 22 (2016) 278-289.
- [23] W. Zhou, Z. Wang, Y. Pu, Y. Li, S. Xin, X. Li, J. Chen, J.B. Goodenough, Double-layer polymer electrolyte for high-voltage all-solid-state rechargeable batteries, *Adv. Mater.* 31 (2019) 1805574.
- [24] Y. Zhou, Y. Yang, N. Zhou, R. Li, Y. Zhou, W. Yan, Four-armed branching and thermally integrated imidazolium-based polymerized ionic liquid as an all-solid-state polymer electrolyte for lithium metal battery, *Electrochim. Acta* (2019) 134827.
- [25] R. Xu, X. Xia, S. Zhang, D. Xie, X. Wang, J. Tu, Interfacial challenges and progress for inorganic all-solid-state lithium batteries, *Electrochim. Acta* 284 (2018) 177-187.
- [26] S. Kim, S.-J. Park, Interlayer spacing effect of alkylammonium-modified montmorillonite on conducting and mechanical behaviors of polymer composite electrolytes, *J. Colloid Interface Sci.* 332 (2009) 145-150.

- [27] W. Liu, S.W. Lee, D. Lin, F. Shi, S. Wang, A.D. Sendek, Y. Cui, Enhancing ionic conductivity in composite polymer electrolytes with well-aligned ceramic nanowires, *Nat. Energy* 2 (2017) 17035.
- [28] J. Zhang, J. Zhao, L. Yue, Q. Wang, J. Chai, Z. Liu, X. Zhou, H. Li, Y. Guo, G. Cui, Safety-reinforced poly (propylene carbonate)-based all-solid-state polymer electrolyte for ambient-temperature solid polymer lithium batteries, *Adv. Energy Mater.* 5 (2015) 1501082.
- [29] Z. Wu, Z. Xie, A. Yoshida, Z. Wang, X. Hao, A. Abudula, G. Guan, Utmost limits of various solid electrolytes in all-solid-state lithium batteries: A critical review, *Renewable Sustainable Energy Rev.* 109 (2019) 367-385.
- [30] M. Marzantowicz, J. Dygas, F. Krok, Z. Florjańczyk, E. Zygadło-Monikowska, G. Lapienis, Ionic conductivity of electrolytes based on star-branched poly (ethylene oxide) with high concentration of lithium salts, *Solid State Ionics* 192 (2011) 137-142.
- [31] K. Pożyczka, M. Marzantowicz, J. Dygas, F. Krok, Ionic conductivity and lithium transference number of poly (ethylene oxide): LiTFSI system, *Electrochim. Acta* 227 (2017) 127-135.
- [32] Y. Zhao, C. Wu, G. Peng, X. Chen, X. Yao, Y. Bai, F. Wu, S. Chen, X. Xu, A new solid polymer electrolyte incorporating $\text{Li}_{10}\text{GeP}_2\text{S}_{12}$ into a polyethylene oxide matrix for all-solid-state lithium batteries, *J. Power Sources* 301 (2016) 47-53.
- [33] R. Bouchet, S. Maria, R. Meziane, A. Aboulaich, L. Lienafa, J.-P. Bonnet, T.N. Phan, D. Bertin, D. Gigmes, D. Devaux, Single-ion BAB triblock copolymers as highly efficient electrolytes for lithium-metal batteries, *Nat. Mater.* 12 (2013) 452.

- [34] C.E. Sing, J.W. Zwanikken, M.O. De La Cruz, Electrostatic control of block copolymer morphology, *Nat. Mater.* 13 (2014) 694.
- [35] Z. Xie, Z. Wu, X. An, A. Yoshida, Z. Wang, X. Hao, A. Abudula, G. Guan, Bifunctional ionic liquid and conducting ceramic co-assisted solid polymer electrolyte membrane for quasi-solid-state lithium metal batteries, *J. Membr. Sci.* 586 (2019) 122-129.
- [36] S. Huang, Z. Cui, L. Qiao, G. Xu, J. Zhang, K. Tang, X. Liu, Q. Wang, X. Zhou, B. Zhang, An in-situ polymerized solid polymer electrolyte enables excellent interfacial compatibility in lithium batteries, *Electrochim. Acta* 299 (2019) 820-827.
- [37] X. Hao, H. Wenren, X. Wang, X. Xia, J. Tu, A gel polymer electrolyte based on PVDF-HFP modified double polymer matrices via ultraviolet polymerization for lithium-sulfur batteries, *J. Colloid Interface Sci.* 558 (2019) 145-154.
- [38] Y. Zhang, Y. Zhao, D. Gosselink, P. Chen, Synthesis of poly(ethylene-oxide)/nanoclay solid polymer electrolyte for all solid-state lithium/sulfur battery, *Ionics* 21 (2015) 381-385.
- [39] H. Sun, Y. Takeda, N. Imanishi, O. Yamamoto, H.J. Sohn, Ferroelectric materials as a ceramic filler in solid composite polyethylene oxide-based electrolytes, *J. Electrochem. Soc.* 147 (2000) 2462-2467.
- [40] C. Lin, C. Hung, M. Venkateswarlu, B. Hwang, Influence of TiO₂ nano-particles on the transport properties of composite polymer electrolyte for lithium-ion batteries, *J. Power Sources* 146 (2005) 397-401.

- [41] L. Wang, X. Li, W. Yang, Enhancement of electrochemical properties of hot-pressed poly (ethylene oxide)-based nanocomposite polymer electrolyte films for all-solid-state lithium polymer batteries, *Electrochim. Acta* 55 (2010) 1895-1899.
- [42] S. Klongkan, J. Pumchusak, Effects of nano alumina and plasticizers on morphology, ionic conductivity, thermal and mechanical properties of PEO-LiCF₃SO₃ solid polymer electrolyte, *Electrochim. Acta* 161 (2015) 171-176.
- [43] J.-H. Choi, C.-H. Lee, J.-H. Yu, C.-H. Doh, S.-M. Lee, Enhancement of ionic conductivity of composite membranes for all-solid-state lithium rechargeable batteries incorporating tetragonal Li₇La₃Zr₂O₁₂ into a polyethylene oxide matrix, *J. Power Sources* 274 (2015) 458-463.
- [44] W. Liu, D. Lin, J. Sun, G. Zhou, Y. Cui, Improved lithium ionic conductivity in composite polymer electrolytes with oxide-ion conducting nanowires, *ACS nano* 10 (2016) 11407-11413.
- [45] N. Guillou, Q. Gao, P.M. Forster, J.S. Chang, M. Noguès, S.E. Park, G. Férey, A.K. Cheetham, Nickel (II) phosphate VSB-5: a magnetic nanoporous hydrogenation catalyst with 24-ring tunnels, *Angew. Chem., Int. Ed.* 40 (2001) 2831-2834.
- [46] Z. Chen, D. Zhou, T. Gao, W. Shen, X. Dong, S. Naito, L. Qin, Y. Huang, Unusual adsorption and desorption behaviors of NO and CO on nanoporous nickel phosphate VSB-5: In situ FT-IR and TPD study, *Catal. Today* 258 (2015) 199-204.
- [47] S.J. Liu, H.Y. Cheng, F.Y. Zhao, J.Y. Gong, S.H. Yu, Controllable synthesis of VSB-5 microspheres and microrods: growth mechanism and selective hydrogenation catalysis, *Chem. - Eur. J.* 14 (2008) 4074-4081.

- [48] W. Liu, N. Liu, J. Sun, P.-C. Hsu, Y. Li, H.-W. Lee, Y. Cui, Ionic conductivity enhancement of polymer electrolytes with ceramic nanowire fillers, *Nano Lett.* 15 (2015) 2740-2745.
- [49] H. Gupta, L. Balo, V.K. Singh, S.K. Chaurasia, R.K. Singh, Effect of phosphonium based ionic liquid on structural, electrochemical and thermal behaviour of polymer poly (ethylene oxide) containing salt lithium bis (trifluoromethylsulfonyl) imide, *RSC Adv.* 6 (2016) 87878-87887.
- [50] J. Lee, T. Howell, M. Rottmayer, J. Boeckl, H. Huang, Free-standing PEO/LiTFSI/LAGP composite electrolyte membranes for applications to flexible solid-state lithium-based batteries, *J. Electrochem. Soc.* 166 (2019) A416-A422.
- [51] M. Marzantowicz, J. Dygas, F. Krok, J. Nowiński, A. Tomaszewska, Z. Florjańczyk, E. Zygadło-Monikowska, Crystalline phases, morphology and conductivity of PEO: LiTFSI electrolytes in the eutectic region, *J. Power Sources* 159 (2006) 420-430.
- [52] W. Kam, C.-W. Liew, J. Lim, S. Ramesh, Electrical, structural, and thermal studies of antimony trioxide-doped poly (acrylic acid)-based composite polymer electrolytes, *Ionics* 20 (2014) 665-674.
- [53] D.E. Hegazy, G.A. Mahmoud, Radiation synthesis and characterization of polyethylene oxide/chitosan-silver nanocomposite for biomedical applications, *Arab J. Nucl. Sci. Appl.* 47 (2014) 1-14.
- [54] Y. Jiang, Q. Gao, Preparation of $\text{Cu}^{2+/+}$ -VSB-5 and their catalytic properties on hydroxylation of phenol, *Mater. Lett.* 61 (2007) 2212-2216.

- [55] Z. Xie, Z. Wu, X. An, X. Yue, P. Xiaokaiti, A. Yoshida, A. Abudula, G. Guan, A sandwich-type composite polymer electrolyte for all-solid-state lithium metal batteries with high areal capacity and cycling stability, *J. Membr. Sci.* 596 (2020) 117739.
- [56] W. Tang, S. Tang, C. Zhang, Q. Ma, Q. Xiang, Y.W. Yang, J. Luo, Simultaneously enhancing the thermal stability, mechanical modulus, and electrochemical performance of solid polymer electrolytes by incorporating 2D sheets, *Adv. Energy Mater.* 8 (2018) 1800866.54.

Chapter 5 Simultaneously enhancing the thermal stability and electrochemical performance of solid polymer electrolytes by incorporating rod-like $\text{Zn}_2(\text{OH})\text{BO}_3$ particles

5.1 Introduction

Lithium ion batteries have been intensively studied and applied in electric vehicles and power grids [1-7]. Lithium anode has excellent theoretical specific capacity ($3860 \text{ mAh}\cdot\text{g}^{-1}$) due to its low density ($0.59 \text{ g}\cdot\text{cm}^{-3}$) and high electrochemical potential (-3.04 V vs. standard hydrogen electrode) [8]. Unfortunately, the reactions between Li anode and the liquid organic electrolyte at the interfaces may lead to serious safety issues including thermal runaway resulted combustion/explosion of the batteries and the growth of lithium dendrites. To solve this problem, application of solid state electrolyte is regarded as a perfect way, which has been attracting more and more attentions and various SEs have been developed [9-17].

SEs include inorganic SEs, solid polymer electrolytes (SPEs) and solid composite electrolytes [18-23]. SPEs have good mechanical property, excellent flexibility and easy processability, which were reported for the first time by Wright *et al.* [24]. Various polymer matrixes including poly(ethylene oxide) (PEO) [25-31], polyvinyl chloride (PVC) [32, 33], poly(vinylidene fluoride) (PVDF) [16, 34, 35], polyacrylonitrile (PAN) [36] and poly(vinylidene fluoride-co-hexafluoropropylene) (PVDF-HFP) [37-40], have been studied as the SPEs. However, SPEs have not been widely used in the commercial lithium batteries until now due to their low ionic conductivities at room temperature and

poor electrochemical stability. As such, various improved ways have been proposed to tackle these issues. To decrease the crystallization of SPEs and strengthen their mechanical properties plasticizers like glycerol and poly(ethyl methacrylate) were added in them [41, 42]. Moreover, the polymer matrix was also modified by crosslinking, copolymerization and other ways [43-45]. Despite these efforts, the ionic conductivity, mechanical strength and electrochemical stability of SPEs still do not meet the practical application requirements.

Recently, an effective way by dispersing of ceramic particles such as Al_2O_3 , SiO_2 , LiAlO_2 , TiO_2 , and ZnAl_2O_4 in the polymer matrix to improve the performance of SPEs has been widely applied in the studies [46-49]. It is found that the addition of these ceramic particles can hinder the polymer crystallization or form high conductive interface layers between polymer matrix and ceramic particle, which can effectively improve the ionic conductivity, mechanical strength and electrochemical stability. In particular, ceramic fillers with special shapes could enhance the ionic conductivity more greatly. Cui *et al.* found that ceramic nanowire fillers can facilitate the formation of ionic conduction networks in the SPEs for the enhancement of the ionic conductivity [50]. Meanwhile, they reported a solid composite polymer electrolyte with Y_2O_3 -doped ZrO_2 (YSZ) nanowires filler, in which the YSZ nanowire enriched with positive-charged oxygen vacancies on its surface could attract more anions for combining and releasing Li^+ so that the ion conductivity was effectively improved [51].

In this study, a flame-retardant filler, $\text{Zn}_2(\text{OH})\text{BO}_3$, with relatively high dehydration temperature (about 415 °C) [52], was used for the improvement of the performance of SPE electrolyte for the first time. The rod-like $\text{Zn}_2(\text{OH})\text{BO}_3$ particles were synthesized via the hydrothermal method, and then dispersed in the PEO-LiTFSI composite system

to prepare a novel SPE named as PEO-LiTFSI-Zn₂(OH)BO₃. The structure, mechanism of improved property and solid-state lithium battery (SSLBs) performance base on such rod-like Zn₂(OH)BO₃ particles-filled SPEs were systematically investigated. It is found that the obtained SPE had enhanced ionic conductivity at room temperature, wide electrochemical window, good lithium anode stability and excellent thermal stability.

5.2 Experimental Section

5.2.1 Synthesis of rod-like Zn₂(OH)BO₃ particles

Zinc Sulfate Heptahydrate (ZnSO₄·7H₂O), polyethylene glycol-300 (PEG 300) and borax pentahydrate (Na₂B₄O₇·10H₂O) were used as the starting materials. Firstly, 40 mL of 0.25 mol·L⁻¹ ZnSO₄ solution and 1 mL of PEG 300 were mixed completely. Then, after 0.01 mol of Na₂B₄O₇·10H₂O was dissolved in 40 mL of distilled water at 40 °C (i.e., 0.25 mol·L⁻¹ Na₂B₄O₇ solution), it was added into the above ZnSO₄-PEG 300 solution slowly with vigorous stirring until the solution became homogeneous. Finally, the mixture was transferred to a 100 mL Teflon-lined stainless autoclave, which was maintained at 100 °C for 24 h and then naturally cooled down to room temperature. The resulting white precipitates were separated by centrifugation, washed successively with deionized water and anhydrous ethanol for 3 times respectively, and dried in air at 80 °C for 4 h.

5.2.2 Synthesis of solid polymer composite electrolytes

PEO (MW = 6×10⁵), LiTFSI, and as-prepared rod-like Zn₂(OH)BO₃ particles were completely dried before use. Then, calculated amounts of Zn₂(OH)BO₃, PEO, and lithium bis(trifluoromethane)sulfonilimide (LiTFSI) were ground in a mortar to obtain a rough soft-cloth-like material. Herein, the PEO and LiTFSI were mixed with a molar ratio of

8:1 (EO:Li) and the contents of $\text{Zn}_2(\text{OH})\text{BO}_3$ were varied from 0 to 15 wt%. The final material was sealed in the glass bottle, transferred to a vacuum oven and heat treated at 80 °C for 12 h. Finally, the SPE membrane was prepared by a cold pressing process with a pressing time of 12 h under 5 MPa.

5.2.3 Characterizations

Fourier transform infrared (FT-IR) spectroscopy was performed to determine chemical structures in the SPE sample in the wave number ranging from 4000 to 400 cm^{-1} (FT/IR-4200, JASCO, Japan). All samples were identified by X-ray powder diffraction (XRD) (Smartlab 9kW, Rigaku, Japan) with Cu target at a scanning rate of $10^\circ \cdot \text{min}^{-1}$ with 2θ ranging from 10° to 90° . Differential Scanning Calorimetry (DSC) measurement of the SPE was performed by using a thermal analyzer (SII, DSC 6200, Japan) with a heating rate of $10^\circ \text{C} \cdot \text{min}^{-1}$ under Ar atmosphere. Thermogravimetric analysis (TGA) and derivative thermogravimetric analysis (DTG) were carried out using a TA machine (TA-60WS, SHIMADZU, Japan) with a heating rate of $10^\circ \text{C} \cdot \text{min}^{-1}$ under N_2 atmosphere. The morphology and elemental composition were characterized by means of a scanning electron microscopy (SEM) with an energy dispersive X-ray spectroscopy (EDS) (SU8010, Hitachi, Japan).

5.2.4 Electrochemical evaluation of solid polymer composite electrolyte

Ionic conductivity of the SPE was tested by an electrochemical impedance spectroscopy (EIS) (VersaSTAT 4, Princeton Applied Research, USA) in the frequency range from 10 Hz to 1 MHz. Herein, the SPE membrane was sandwiched between two stainless steel (SS) foils to form a SS/SPE/SS cell. The Li^+ transference number (t_{Li}^+) was

determined by DC polarization method combined with the EIS, in which a voltage of 10 mV was applied on the cell and the EIS spectra of the cell before and after the polarization were obtained in a frequency range of 0.01-10⁵ Hz. As such, the t_{Li}^+ can be calculated using the following equation:

$$t_{Li}^+ = \frac{I_s(\Delta V - I_0 R_0)}{I_0(\Delta V - I_s R_s)} \quad \text{Eq. (1)}$$

where ΔV is the applied DC polarization voltage (0.01 V), I_0 and I_s are initial and stable currents during the polarization, R_0 and R_s are the resistances of the SPE before and after the polarization. The electrochemical stability window of the SPE was determined by a linear sweep voltammetry (LSV) performed on a working electrode of stainless steel and a counter electrode of lithium metal foil under the applied voltages between 2.0 V and 5.5 V at a scan rate of 1 mV·S⁻¹. The interfacial stability of SPE was evaluated by lithium stripping/plating cycling way performed with a Li/SPE/Li coin cell at a current of 0.1 mA.

5.2.5 Electrochemical evaluation of solid-state battery

To prepare the cathode, a mixture of LiFePO₄ particles, conductive additive super P, polyvinylidene fluoride (PVDF) binder with a weight ratio of 8:1:1 was stirred for 2 h to get a homogenous slurry by using a proper amount of N-methyl-2-pyrrolidone (NMP) as solvent and then pasted on an Al foil current collector, and dried at 80 °C under vacuum for 12 h. The specific capacity of the cathode was calculated on the base of the LiFePO₄ mass. The solid-state battery was fabricated by using a lithium metal anode, the prepared SPE membrane and a LiFePO₄ cathode. The charging-discharging and cycling properties were evaluated at the applied potentials between 2.5 V and 4.0 V with a LANHE CT2001A charge/discharge system (Wuhan LAND Electronics Co., Ltd.) at 60 °C.

5.3 Results and discussion

Figure 5.1(A-B) shows the SEM images of as-prepared rod-like $\text{Zn}_2(\text{OH})\text{BO}_3$ particles with different magnifications. One can see that the obtained $\text{Zn}_2(\text{OH})\text{BO}_3$ particles had rod-like shape with nanoscale cross diameter of approximately 100-200 nm and the length exceeding 3 μm . As shown in the inset of Figure 5.1C, the $\text{Zn}_2(\text{OH})\text{BO}_3$ contains two independent types of ZnO_4 tetrahedra and BO_3 groups linked through common O vertices [53, 54]. Although the presence of OH groups in $\text{Zn}_2(\text{OH})\text{BO}_3$ was confirmed by infrared spectroscopy, the position for the H atom of the OH group could not be located crystallographically [53]. The H atom may exist freely in the network structure. According to the chemical structures of $\text{Zn}_2(\text{OH})\text{BO}_3$ and PEO, hydrogen bonds could be formed between $\text{Zn}_2(\text{OH})\text{BO}_3$ and PEO, which could enable the polymer chains more disordered in the copolymer, forming a 3D network structure. The formed network structure is expected to provide the possible paths for the transport of lithium ions. Analogously, the uniform rod-like structure could also provide fast and efficient lithium ion transport channels to avoid ineffective interleaving [10, 55]. Therefore, the rod-like $\text{Zn}_2(\text{OH})\text{BO}_3$ particle was selected as additive to improve SPE performance.

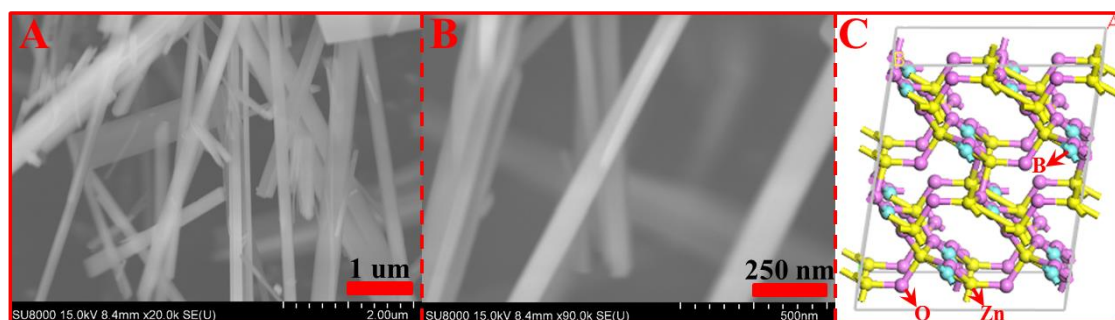


Figure 5.1 (A-B) The SEM images of the as-prepared $\text{Zn}_2(\text{OH})\text{BO}_3$ particles with different magnifications and (C) the crystal structures of $\text{Zn}_2(\text{OH})\text{BO}_3$.

The variation of impedance spectrum of SPE with the increase in the content of

$\text{Zn}_2(\text{OH})\text{BO}_3$ at 30 °C is presented in Figure 5.2A. One can see that the impedance spectrum consisted of a semicircle in the high frequency region and a spike in the lower frequency region, where the semicircle is attributed to the bulk resistance of SPE and the interfacial resistance between the SPE and SS electrode, and the spike represents the ion diffusion impedance in the electrode. Based on the impedance spectrum, the ionic conductivity (σ) can be calculated as following equation:

$$\sigma = \frac{d}{R \times S} \quad \text{Eq. (2)}$$

where d is the thickness of the SPE, R is the bulk resistance, and S is the area of the SPE. As a result, the ionic conductivity increased with the increase in the $\text{Zn}_2(\text{OH})\text{BO}_3$ particles addition amount, and reached a highest value of $2.78 \times 10^{-5} \text{ S} \cdot \text{cm}^{-1}$ at 30 °C when 10 wt% of $\text{Zn}_2(\text{OH})\text{BO}_3$ particles was added in the SPE (called it as PEO-LiTFSI-10% $\text{Zn}_2(\text{OH})\text{BO}_3$), and then decreased with the further increasing of the amount of $\text{Zn}_2(\text{OH})\text{BO}_3$, which could be caused by the phase separation between $\text{Zn}_2(\text{OH})\text{BO}_3$ and PEO, and the aggregation of the excessive $\text{Zn}_2(\text{OH})\text{BO}_3$ particles [51, 56]. Herein, it should be noted that the obtained highest ionic conductivity of PEO-LiTFSI-10% $\text{Zn}_2(\text{OH})\text{BO}_3$ was approximately two times higher than that of pure PEO SPE ($1.58 \times 10^{-5} \text{ S} \cdot \text{cm}^{-1}$ at 30 °C).

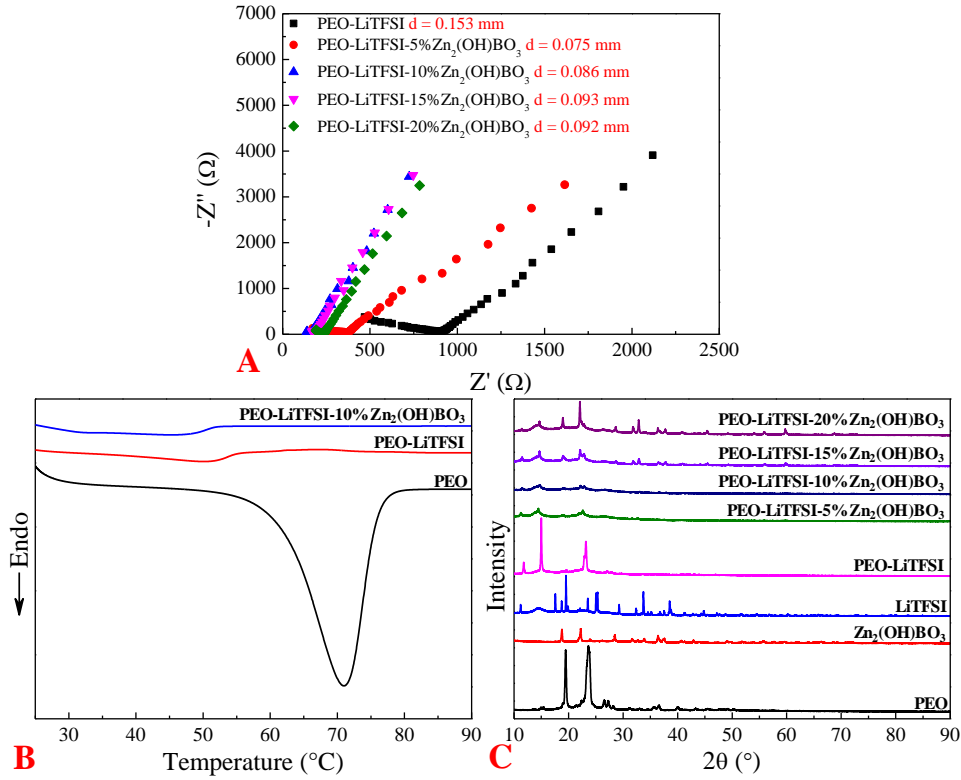


Figure 5.2 EISs (A) of PEO-LiTFSI- $x\%$ $Zn_2(OH)BO_3$ ($x = 0, 5, 10, 15$, and 20) at 30 $^{\circ}C$, DSCs thermograms (B) and XRD patterns (C) of PEO, PEO-LiTFSI and PEO-LiTFSI-10% $Zn_2(OH)BO_3$, d : Thickness.

Figure 5.2B shows DSC thermograms of PEO, PEO-LiTFSI, and PEO-LiTFSI-10% $Zn_2(OH)BO_3$ in a temperature range from 25 to 90 $^{\circ}C$. The melting temperature (T_m), melting enthalpy (ΔH) and degree of crystallinity (χ_c) based on these DSC thermograms are listed in Table 1. From Figure 5.2B and Table 5.1, the melting transition temperature of PEO was near 71.0 $^{\circ}C$, and after the addition of LiTFSI into PEO matrix, the melting temperature was shifted to lower temperature at 50.3 $^{\circ}C$, and furthermore, after 10wt% of $Zn_2(OH)BO_3$ was added, the obtained PEO-LiTFSI-10% $Zn_2(OH)BO_3$ composite electrolyte showed the lowest melting point of 45.2 $^{\circ}C$. Meanwhile, the melting enthalpy (ΔH) corresponding to the melting peak also decreased with the addition of LiTFSI and

further decreased by the further addition of $\text{Zn}_2(\text{OH})\text{BO}_3$. In addition, the degree of crystallinity (χ_c) based on the pure PEO crystallinity (100%) can be calculated by the following equation:

$$\chi_c = \frac{\Delta H}{\Delta H_0} \times 100\% \quad \text{Eq. (3)}$$

where ΔH_0 is the standard melting enthalpy of pure PEO. As such, the degree of crystallinity of PEO-LiTFSI and PEO-LiTFSI-10% $\text{Zn}_2(\text{OH})\text{BO}_3$ were calculated as 12.2% and 10.7%, respectively, which indicated that the addition $\text{Zn}_2(\text{OH})\text{BO}_3$ effectively decreased the crystallinity of PEO and simultaneously increased PEO amorphous region to favor Li^+ ion hopping, and consequently increased the ionic conductivity [57].

In order to explore the crystalline phase in PEO-LiTFSI- $x\%\text{Zn}_2(\text{OH})\text{BO}_3$ ($x = 0, 5, 10, 15$, and 20) SPEs, XRD measurements were also performed and the results are shown in Figure 5.2C. Herein, the peaks at 19.47° and 23.64° are ascribed to the PEO crystalline structure [58]. The peaks of LiTFSI are un conspicuous in the PEO-LiTFSI- $x\%\text{Zn}_2(\text{OH})\text{BO}_3$ ($x = 0, 5, 10, 15$, and 20) SPEs due to the complete dissolution and dispersion of lithium salts [58]. The peak intensities at 14.98° and 23.01° decreased with the addition of 10% of $\text{Zn}_2(\text{OH})\text{BO}_3$, also indicating the lowering of the crystallinity of PEO. These results are well consistent with those of DSC analysis. Moreover, the peaks corresponding to the $\text{Zn}_2(\text{OH})\text{BO}_3$ were obviously observed in the XRD patterns of PEO-LiTFSI- $x\%\text{Zn}_2(\text{OH})\text{BO}_3$ ($x = 15$ and 20) SPE samples but not so obvious for the PEO-LiTFSI-10% $\text{Zn}_2(\text{OH})\text{BO}_3$, indicating that 10% of $\text{Zn}_2(\text{OH})\text{BO}_3$ could be well dispersed in the PEO-LiTFSI system.

Table 5.1 Melting temperature T_m , melting enthalpy ΔH , and degree of crystallinity χ_c of PEO, PEO-LiTFSI and PEO-LiTFSI-10% $\text{Zn}_2(\text{OH})\text{BO}_3$.

Sample	T_m (°C)	ΔH (J·g ⁻¹)	χ_c (%)
PEO	71.0	174.0	100
PEO-LiTFSI	50.3	21.2	12.2
PEO-LiTFSI- 10%Zn ₂ (OH)BO ₃	45.2	18.6	10.7

To investigate the chain conformation of the PEO-LiTFSI containing Zn₂(OH)BO₃ in the SPEs, FT-IR analysis was performed. As shown in Figure 5.3A, the peaks at 2891, 1146 and 842 cm⁻¹ correspond to the symmetrical CH₂-stretching, C–O–C asymmetric stretching and CH₂ wagging modes of PEO, respectively [59, 60]. The peaks at 1356, 1203, 797 and 743 cm⁻¹ are assigned to the SO₃ vibration, CF₃ vibration, C–S vibration, S–N vibration modes of LiTFSI, respectively [61]. When Zn₂(OH)BO₃ was added to the PEO-LiTFSI, the peak of symmetrical CH₂-stretching at 2891 cm⁻¹ became weaker and wider, which indicated the greatly reducing of the crystallinity of PEO caused by the Lewis acid-base interaction between the Zn₂(OH)BO₃ and the oxygen atom of ether group on the PEO. In addition, the OH stretching vibration at 3428 cm⁻¹ and CH₂ bending vibration at 1473 cm⁻¹ also became weaker after the addition of Zn₂(OH)BO₃, which further indicated that Zn₂(OH)BO₃ could increase the amorphous region of PEO as the lithium salt effect. As illustrated in Figure 5.3(B-C) and Figure 5.9, comparing to the PEO-LiTFSI SPE with partial PEO crystallization and nonuniform lithium deposition, the PEO-LiTFSI-Zn₂(OH)BO₃ SPE with more reduced crystallinity enables the improvement of Li⁺ transmission and uniform Li-ion distribution, and in turn, results in the suppression of lithium dendrite.

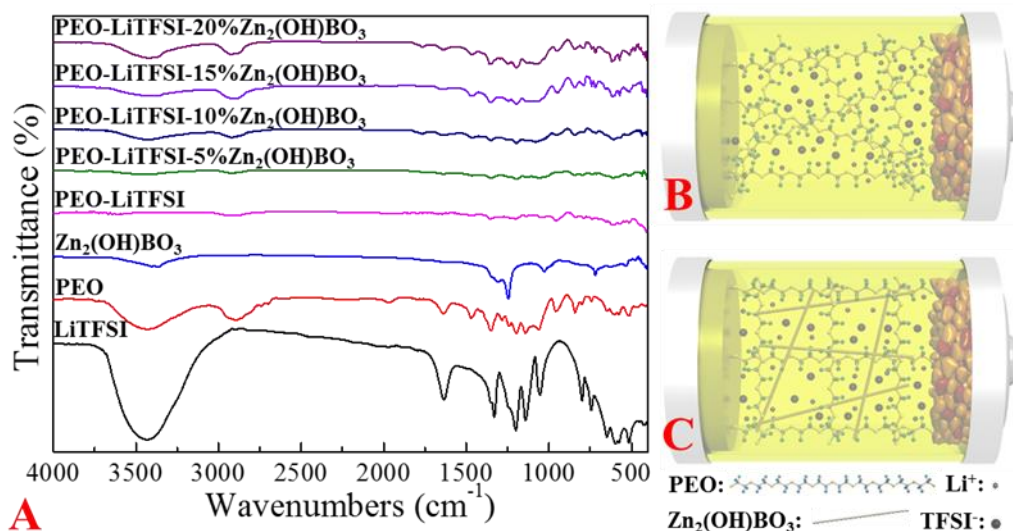


Figure 5.3 (A) FT-IR spectra of PEO, $\text{Zn}_2(\text{OH})\text{BO}_3$, LiTFSI and PEO-LiTFSI- $x\%\text{Zn}_2(\text{OH})\text{BO}_3$ in the range of $400\text{--}4000\text{ cm}^{-1}$. Schematic showing the PEO-LiTFSI (B) and the increased conformational mobility of PEO-LiTFSI- $\text{Zn}_2(\text{OH})\text{BO}_3$ (C).

In addition to the ionic conductivity, the electrochemical window stability and thermal stability are also very important factors for SPEs. The LSV curves of SS|SPE|Li cells measured in the potential range between 2.0 and 5.5 V are shown in Figure 5.4A, which can describe the electrochemical window stability of SPEs. For the PEO-LiTFSI SPE, it is obvious that the current began to flow when the applied potential reached above 4.05 V, indicating the start of the SPE oxidation process. In contrast, the PEO-LiTFSI-10% $\text{Zn}_2(\text{OH})\text{BO}_3$ SPE showed a good oxidative stability up to 4.51 V without an obvious current flow. The enhanced electrochemical window stability can be attributed to the interaction between $\text{Zn}_2(\text{OH})\text{BO}_3$ and PEO with a cross-linked structure in the PEO-LiTFSI-10% $\text{Zn}_2(\text{OH})\text{BO}_3$ SPEs.

The thermal stability of the PEO-LiTFSI and the PEO-LiTFSI-10% $\text{Zn}_2(\text{OH})\text{BO}_3$ SPEs were also carried out by measuring the TGA and the differential thermogravimetric

(DTG) curves. As shown in Figure 5.4B, the initial weight loss and the second weight loss for PEO-LiTFSI and the PEO-LiTFSI-10%Zn₂(OH)BO₃ SPEs occurred in the temperature range of 313-485 °C with two sharp peaks. The initial weight loss should be caused by the decomposition of PEO. It should be noted that the decomposition peaks in the DTG curve for the PEO-LiTFSI-10%Zn₂(OH)BO₃ SPE at 428 °C shifted to the right, i.e., about 9 °C higher, when compared with that of the PEO-LiTFSI SPE. Meanwhile, the second decomposition peak in the DTG curve of the PEO-LiTFSI-10%Zn₂(OH)BO₃ SPE was observed at 458 °C, which is from the decomposition of LiTFSI. It was also higher than that of PEO-LiTFSI SPE (432 °C). In addition, the residual at 700 °C for the PEO-LiTFSI-10%Zn₂(OH)BO₃ SPE was 11.3%, which was also more than that of the PEO-LiTFSI SPE (6.9%) since most of it should be from Zn₂(OH)BO₃. The high thermal stability of the PEO-LiTFSI-10%Zn₂(OH)BO₃ SPE is expected to guarantee the safety of the practical SSLBs.

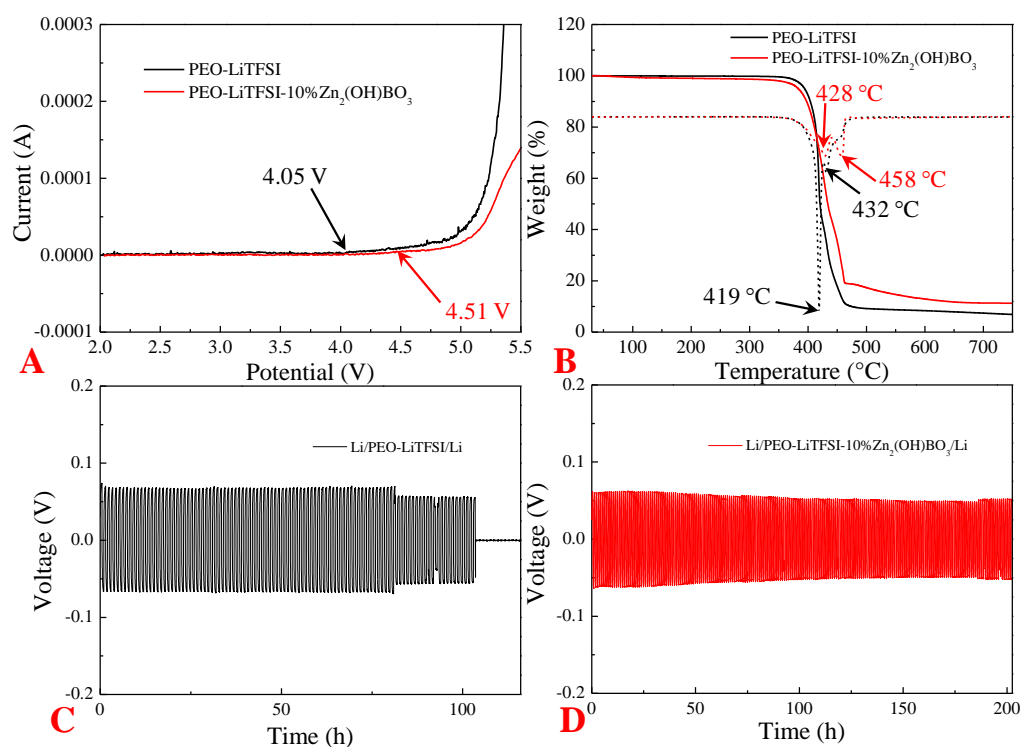


Figure 5.4 (A) LSV curves of PEO-LiTFSI and PEO-LiTFSI-10%Zn₂(OH)BO₃ SPEs at a scanning rate of 1 mV·s⁻¹ and 60 °C, (B) TGA-DTG curves of PEO-LiTFSI and PEO-LiTFSI-10%Zn₂(OH)BO₃ SPEs, lithium deposition/stripping of Li/PEO-LiTFSI/Li (C) and Li/PEO-LiTFSI-10%Zn₂(OH)BO₃/Li (D) symmetrical batteries at a current of 0.1 mA at 60 °C.

Li/SPE interfacial stability was investigated by assembling symmetrical batteries with two Li metal foils as the electrodes. As shown in Figure 5.4(C-D), the Li/PEO-LiTFSI/Li and Li/PEO-LiTFSI-10%Zn₂(OH)BO₃/Li symmetrical batteries were charged/discharged for 1 h during each process with a constant current of 0.1 mA. One can see that after the voltage of Li/PEO-LiTFSI/Li battery stayed at about 0.067 V for 81 h (Figure 5.4C), the voltage decreased to about 0.057 V, and finally, close to 0 V due to the short circuit caused by the growth of lithium dendrite. In comparison, the Li/PEO-LiTFSI-10%Zn₂(OH)BO₃/Li had a much more excellent cycle performance under the same condition. One can see that the voltage of the battery was about 0.06 V at the beginning, and then decreased 0.049 V and hold at this voltage in the cycling test for over 200 h and maintained stable voltage polarization without short circuit (Figure 5.4D). It demonstrated that the PEO-LiTFSI-10%Zn₂(OH)BO₃ SPE had excellent compatibility between the PEO-LiTFSI-10%Zn₂(OH)BO₃ SPE and Li metal with improved the electrochemical performance, in which the growth of Li dendrite should be significantly restrained. In addition, the chronoamperometric curve of a Li/PEO-LiTFSI-10%Zn₂(OH)BO₃/Li battery at 10 mV is shown in Figure 5.5, where the inset is the AC impedance spectra before and after the polarization. Based on this result, the transference number for Li⁺ was calculated as 0.1 by using the Eq. (1).

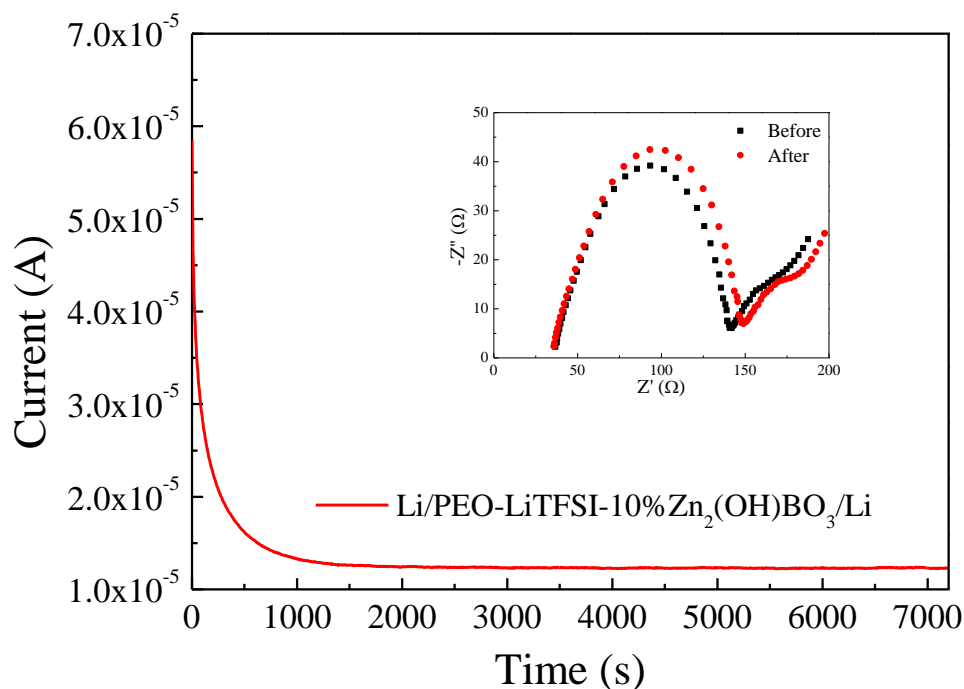


Figure 5.5 Time-dependent response of DC polarization potential obtained on a Li/SPE/Li battery cell at 40 °C. Inset: impedance spectra before and after the polarization.

Figure 5.6 shows SEM images of PEO-LiTFSI-10%Zn₂(OH)BO₃ SPEs. One can see that the surface of PEO-LiTFSI-10%Zn₂(OH)BO₃ SPE was flat with a homogeneous structure after the addition of rod-like Zn₂(OH)BO₃ particles, and the rod-like particles were clearly observed and distributed randomly in SPE membrane. The EDS mappings of the PEO-LiTFSI-10%Zn₂(OH)BO₃ SPE membrane are also shown in Figure 5.6. One can see that the elements of S and F from LiTFSI and Zn and B from Zn₂(OH)BO₃ were homogeneously distributed in the membrane, indicating that the LiTFSI and Zn₂(OH)BO₃ particles were uniformly dispersed in the PEO matrix. Moreover, the SEM and EDS measurements for the LiFePO₄/PEO-LiTFSI-10%Zn₂(OH)BO₃/Li battery were also performed. As shown in Figure 5.7(B-D), the element Fe from the LiFePO₄ cathode and

the element Zn from PEO-LiTFSI-10%Zn₂(OH)BO₃ SPE were observed in the cathode and electrolyte respectively with an obvious interface between LiFePO₄ cathode and PEO-LiTFSI-10%Zn₂(OH)BO₃ SPE.

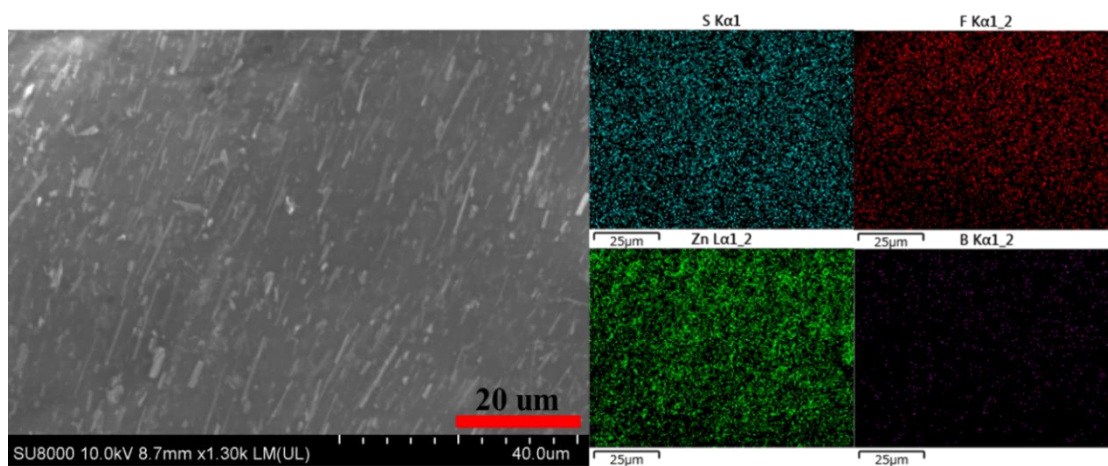


Figure 5.6 SEM image and EDS mappings of the PEO-LiTFSI-10%Zn₂(OH)BO₃.

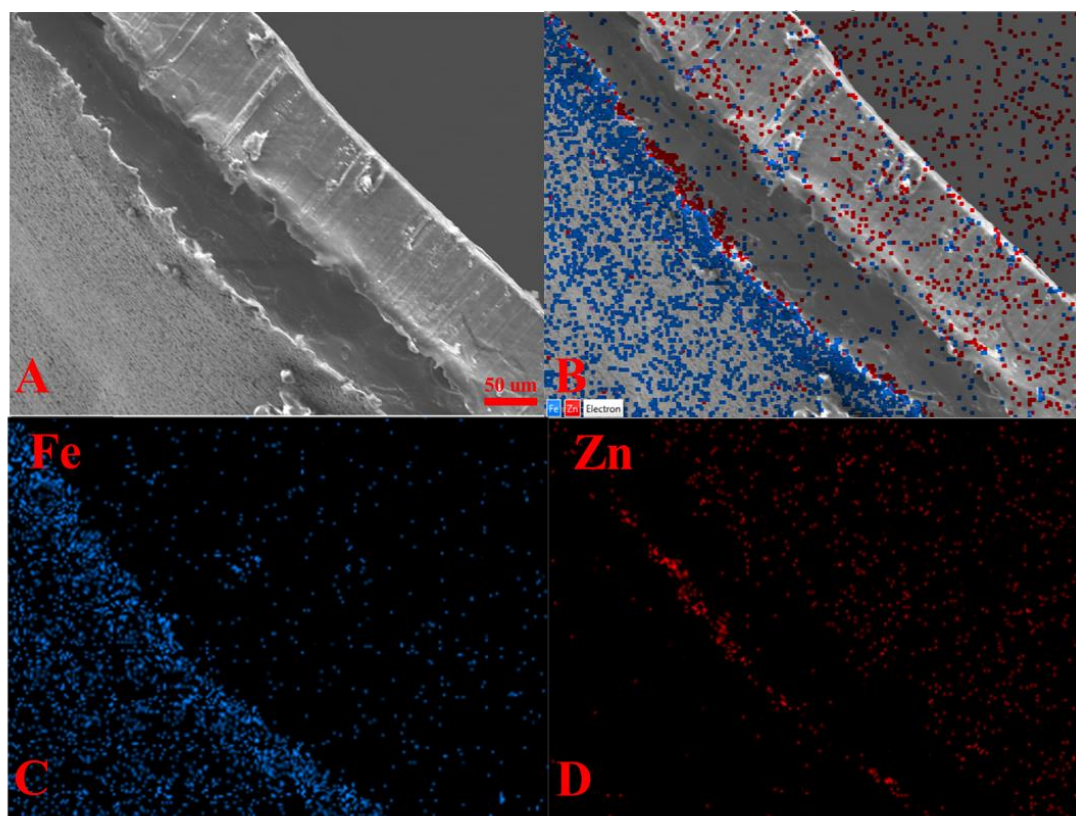


Figure 5.7 SEM images of the LiFePO₄/PEO-LiTFSI-10%Zn₂(OH)BO₃/Li battery. (A)

Cross sectional images. (B-D) Element mapping of the LiFePO₄/PEO-LiTFSI-10%Zn₂(OH)BO₃/Li battery.

The performance of the PEO-LiTFSI-10%Zn₂(OH)BO₃ was further evaluated by assembling SSLBs using the lithium metal anode and the LiFePO₄ cathode. Figure 5.8A shows the EISs of LiFePO₄/PEO-LiTFSI/Li and LiFePO₄/PEO-LiTFSI-10%Zn₂(OH)BO₃/Li batteries at 60 °C. Both EISs consist of a complex-plane semi-circle in the high-frequency region and a straight line in the lower-frequency region. Herein, the semi-circle (*R*) reflects the impedance related to the electrode-SPE interface whereas the straight line stands for the impedance related to the diffusive components, so-called Warburg impedance. By *ZSimpWin* software fitting, the *R* values corresponding to the PEO-LiTFSI and PEO-LiTFSI-10%Zn₂(OH)BO₃ SPEs were 278.4 and 175.6 Ω, respectively. The lower resistance of the LiFePO₄/PEO-LiTFSI-10%Zn₂(OH)BO₃/Li battery should be resulted from the high ionic conductivity of the PEO-LiTFSI-10%Zn₂(OH)BO₃ SPE and its excellent compatibility with the LiFePO₄ electrode. Meanwhile, the cycling performances of the LiFePO₄/PEO-LiTFSI-10%Zn₂(OH)BO₃/Li and LiFePO₄/PEO-LiTFSI/Li batteries are presented in Figure 5.8B. One can see that the discharge capacities of LiFePO₄/PEO-LiTFSI/Li battery at first 10 cycles was higher than that of LiFePO₄/PEO-LiTFSI-10%Zn₂(OH)BO₃/Li battery since during the initial charge and discharge process, solid electrolyte interface (SEI) of the LiFePO₄/PEO-LiTFSI-10%Zn₂(OH)BO₃/Li battery was continuously formed at the interface between the electrode and the electrolyte, causing a partial loss of the initial capacity. However, the SEI formation could effectively improve the charge and discharge stability of the battery, and the LiFePO₄/PEO-LiTFSI-10%Zn₂(OH)BO₃/Li battery had a stable cycling performance with a specific discharge capacity of 147 mAh·g⁻¹ and a coulombic

efficiency higher than 99.7% at 50th cycle. In contrast, the $\text{LiFePO}_4/\text{PEO-LiTFSI/Li}$ battery also had a good cycling performance before 30 cycles, but the coulombic efficiency fluctuated obviously and the discharge capacity gradually decreased after 30 cycles, which could be resulted from the lithium dendrites grown at the interface between the solid electrolyte and the lithium anode since the continuous growth of lithium dendrites and the consumption of lithium ions always cause instable cycling performance of lithium metal based battery, and the $\text{LiFePO}_4/\text{PEO-LiTFSI-10\%Zn}_2(\text{OH})\text{BO}_3/\text{Li}$ battery had a specific discharge capacity of $147.3 \text{ mAh}\cdot\text{g}^{-1}$ and a coulombic efficiency of 98.88% at 70th cycle. The excellent cycling performance of battery using PEO-LiTFSI-10% $\text{Zn}_2(\text{OH})\text{BO}_3$ SPE indicated that there was a better electrochemical interfacial stability between PEO-LiTFSI-10% $\text{Zn}_2(\text{OH})\text{BO}_3$ SPE and the Li metal anode and the lithium dendrite growth was effectively suppressed. Thus, the PEO-LiTFSI-10% $\text{Zn}_2(\text{OH})\text{BO}_3$ could be a promising SPE material for the high-performance SSLBs.

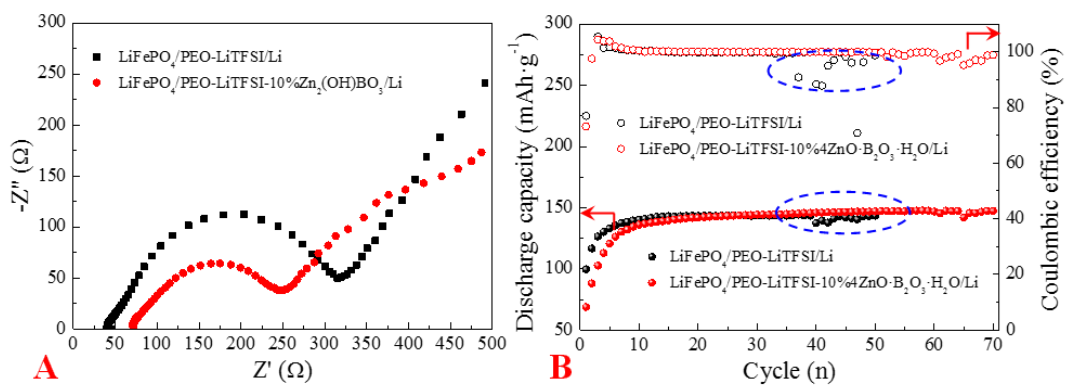


Figure 5.8 (A) EIS of the $\text{LiFePO}_4/\text{PEO-LiTFSI-10\%Zn}_2(\text{OH})\text{BO}_3/\text{Li}$ and $\text{LiFePO}_4/\text{PEO-LiTFSI/Li}$ batteries at 60°C ; (B) Cycling performances of the $\text{LiFePO}_4/\text{PEO-LiTFSI-10\%Zn}_2(\text{OH})\text{BO}_3/\text{Li}$ and $\text{LiFePO}_4/\text{PEO-LiTFSI/Li}$ batteries at 0.2 C .

SEM analyses after the performance test were further carried out to demonstrate the effects of the PEO-LiTFSI-10%Zn₂(OH)BO₃ SPE in the suppression of lithium dendrite growth. From the cross-section images (Figure 5.9(A, C)), the fresh LiFePO₄/PEO-LiTFSI-10%Zn₂(OH)BO₃/Li and LiFePO₄/PEO-LiTFSI/Li batteries had a same sandwich structure with a lithium foil thickness of 80-100 μ m, a SPE membrane thickness of 60-80 μ m, and a LiFePO₄ cathode tightly attached to the SPE membrane surface. After the performance tests, as shown in Figure 5.9B, the surface of the Li anode in the case of PEO-LiTFSI SPE became rough and like “pine cortex” heaves, and the lithium dendrites were clearly observed like “pine cortex” heaves, which may penetrate through PEO-LiTFSI SPE and cause the short circuit. Generally, the growth of lithium dendrites and interfacial reactions during the charging/discharging process could result in the fluctuation of coulombic efficiency. In contrast, the Li/PEO-LiTFSI-10%Zn₂(OH)BO₃ interface showed a smooth and uniform Li surface with no cracks (Figure 5.9D), also indicated the stability of PEO-LiTFSI-10%Zn₂(OH)BO₃ SPE, which finally led to a much higher and more stable coulombic efficiency of SSLBs.

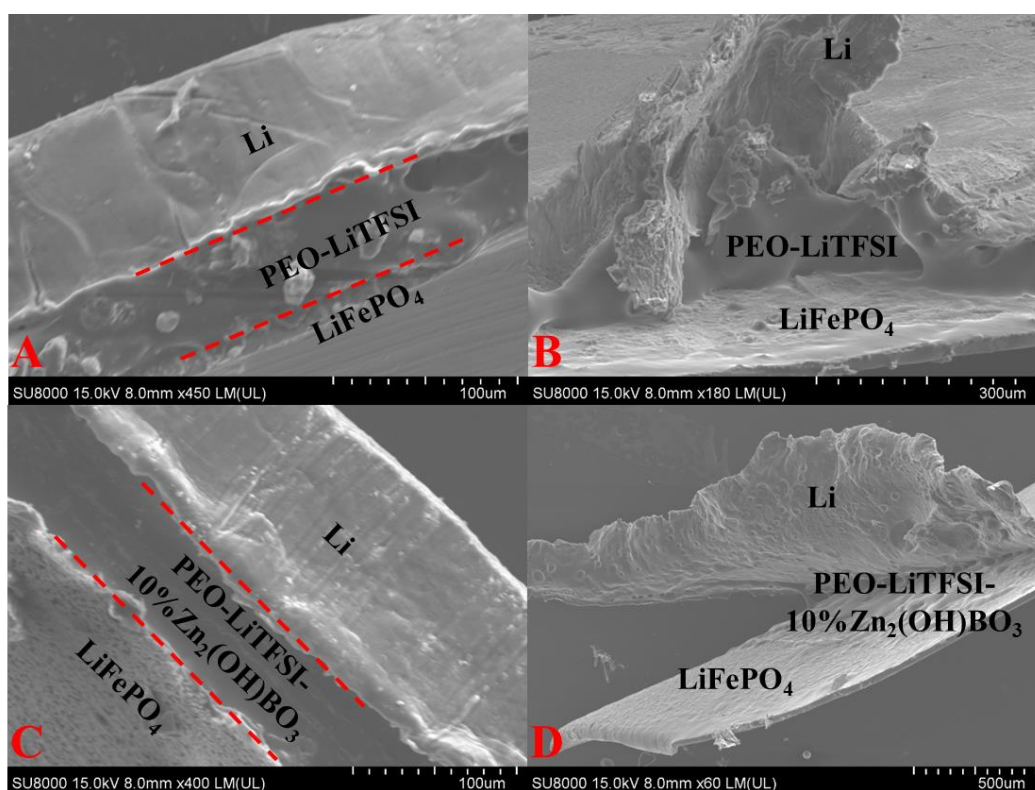


Figure 5.9 SEM images of the cross-sectional views of LiFePO₄/PEO-LiTFSI/Li (A) and LiFePO₄/PEO-LiTFSI-10%Zn₂(OH)BO₃/Li (C) batteries, and the interface views of LiFePO₄/PEO-LiTFSI/Li (B) and LiFePO₄/PEO-LiTFSI-10%Zn₂(OH)BO₃/Li (D) after the cycling performance tests.

5.4 Conclusions

In summary, the rod-like Zn₂(OH)BO₃ particles prepared by the hydrothermal method was successfully applied as a filler to improve PEO-LiTFSI SPE performance. A high conductivity of 2.78×10^{-5} at 30 °C was achieved for the PEO-LiTFSI-10%Zn₂(OH)BO₃ SPE, which can be attributed to the reducing of PEO crystallinity and increasing Li migrating pathway on the interface between Zn₂(OH)BO₃ and PEO. Moreover, the optimum SPE exhibited a wide electrochemical window exceeding 4.51 V

and a high thermal stability. More importantly, such a SPE effectively suppressed the Li dendrite growth. The fabricated $\text{LiFePO}_4/\text{PEO-LiTFSI-10\%Zn}_2(\text{OH})\text{BO}_3/\text{Li}$ SSLB showed excellent cycling stability with a specific discharge capacity of above $147 \text{ mAh}\cdot\text{g}^{-1}$ and a coulombic efficiency higher than 99.7% after 50 cycles, which is noticeably higher than these of the $\text{LiFePO}_4/\text{PEO-LiTFSI/Li}$ SSLB cell. These outstanding performances indicated that the $\text{PEO-LiTFSI-Zn}_2(\text{OH})\text{BO}_3$ SPE could be served as an attractive solid electrolyte for next generation of safe and high electrochemical performance lithium batteries.

References

- [1] D. Larcher, J.-M. Tarascon, Towards greener and more sustainable batteries for electrical energy storage, *Nat. Chem.* 7 (2015) 19.
- [2] N.S. Choi, Z. Chen, S.A. Freunberger, X. Ji, Y.K. Sun, K. Amine, G. Yushin, L.F. Nazar, J. Cho, P.G. Bruce, Challenges facing lithium batteries and electrical double-layer capacitors, *Angew. Chem., Int. Ed.* 51 (2012) 9994-10024.
- [3] E.-S. Lee, A. Huq, H.-Y. Chang, A. Manthiram, High-voltage, high-energy layered-spinel composite cathodes with superior cycle life for lithium-ion batteries, *Chem. Mater.* 24 (2012) 600-612.
- [4] J. Lin, L. Yu, Q. Sun, F. Wang, Y. Cheng, S. Wang, X. Zhang, Multiporous core-shell structured MnO@N-Doped carbon towards high-performance lithium-ion batteries, *Int. J. Hydrogen Energy* 45 (2020) 1837-1845.
- [5] D. Ouyang, J. Weng, M. Chen, J. Wang, Impact of high-temperature environment on the optimal cycle rate of lithium-ion battery, *J. Energy Storage* 28 (2020) 101242.

- [6] A. Chaturvedi, V. Aravindan, P. Hu, R.R. Prabhakar, L.H. Wong, C. Kloc, S. Madhavi, Synthesis of SnS₂ single crystals and its Li-storage performance with LiMn₂O₄ cathode, *Appl. Mater. Today* 5 (2016) 68-72.
- [7] F. Yuan, S. Chi, S. Dong, X. Zou, S. Lv, L. Bao, J. Wang, Ionic liquid crystal with fast ion-conductive tunnels for potential application in solvent-free Li-ion batteries, *Electrochim. Acta* 294 (2019) 249-259.
- [8] Z. Jiang, T. Liu, L. Yan, J. Liu, F. Dong, M. Ling, C. Liang, Z. Lin, Metal-organic framework nanosheets-guided uniform lithium deposition for metallic lithium batteries, *Energy Storage Mater.* 11 (2018) 267-273.
- [9] M. Latroche, D. Blanchard, F. Cuevas, A. El Kharbachi, B.C. Hauback, T.R. Jensen, P.E. de Jongh, S. Kim, N.S. Nazer, P. Ngene, S. Orimo, D.B. Ravnsbæk, V.A. Yartys, Full-cell hydride-based solid-state Li batteries for energy storage, *Int. J. Hydrogen Energy* 44 (2019) 7875-7887.
- [10] O. Sheng, C. Jin, J. Luo, H. Yuan, H. Huang, Y. Gan, J. Zhang, Y. Xia, C. Liang, W. Zhang, Mg₂B₂O₅ nanowire enabled multifunctional solid-state electrolytes with high ionic conductivity, excellent mechanical properties, and flame-retardant performance *Nano Lett.*, 18 (2018) 3104-3112.
- [11] Z. Wu, Z. Xie, A. Yoshida, J. Wang, T. Yu, Z. Wang, X. Hao, A. Abudula, G. Guan, Nickel phosphate nanorod-enhanced polyethylene oxide-based composite polymer electrolytes for solid-state lithium batteries, *J. Colloid Interface Sci.* 565 (2020) 110-118.
- [12] H. Xu, S. Wang, H. Wilson, F. Zhao, A. Manthiram, Y-doped NASICON-type LiZr₂(PO₄)₃ SEs for lithium-metal batteries, *Chem. Mater.* 29 (2017) 7206-7212.

- [13] X. Chi, Y. Liang, F. Hao, Y. Zhang, J. Whiteley, H. Dong, P. Hu, S. Lee, Y. Yao, Tailored organic electrode material compatible with sulfide electrolyte for stable all-solid-state sodium batteries, *Angew. Chem., Int. Ed.* 57 (2018) 2630-2634.
- [14] Z. Wu, Z. Xie, A. Yoshida, X. An, Z. Wang, X. Hao, A. Abudula, G. Guan, Novel SeS_2 doped $\text{Li}_2\text{S-P}_2\text{S}_5$ solid electrolyte with high ionic conductivity for all-solid-state lithium sulfur batteries, *Chem. Eng. J.* 380 (2020) 122419.
- [15] W. Zhou, Z. Wang, Y. Pu, Y. Li, S. Xin, X. Li, J. Chen, J.B. Goodenough, Double-layer polymer electrolyte for high-voltage all-solid-state rechargeable batteries, *Adv. Mater.* 31 (2019) 1805574.
- [16] P. Yao, B. Zhu, H. Zhai, X. Liao, Y. Zhu, W. Xu, Q. Cheng, C. Jayyosi, Z. Li, J. Zhu, PVDF/Palygorskite nanowire composite electrolyte for 4 V rechargeable lithium batteries with high energy density, *Nano Lett.* 18 (2018) 6113-6120.
- [17] G. Liu, D. Xie, X. Wang, X. Yao, S. Chen, R. Xiao, H. Li, X. Xu, High air-stability and superior lithium ion conduction of $\text{Li}_{3+3x}\text{P}_{1-x}\text{Zn}_x\text{S}_{4-x}\text{O}_x$ by aliovalent substitution of ZnO for all-solid-state lithium batteries, *Energy Storage Mater.* 17 (2019) 266-274.
- [18] Z. Wu, Z. Xie, A. Yoshida, Z. Wang, X. Hao, A. Abudula, G. Guan, Utmost limits of various solid electrolytes in all-solid-state lithium batteries: A critical review, *Renewable Sustainable Energy Rev.* 109 (2019) 367-385.
- [19] X. Yao, B. Huang, J. Yin, G. Peng, Z. Huang, C. Gao, D. Liu, X. Xu, All-solid-state lithium batteries with inorganic SEs: Review of fundamental science, *Chin. Phys. B* 25 (2015) 018802.
- [20] A.R. Polu, H.-W. Rhee, Ionic liquid doped PEO-based solid polymer electrolytes for lithium-ion polymer batteries, *Int. J. Hydrogen Energy* 42 (2017) 7212-7219.

- [21] C. Cao, Z.-B. Li, X.-L. Wang, X.-B. Zhao, W.-Q. Han, Recent advances in inorganic SEs for lithium batteries, *Front. Energy Res.* 2 (2014) 25.
- [22] R. Xu, S. Zhang, X. Wang, Y. Xia, X. Xia, J. Wu, C. Gu, J. Tu, Recent developments of all-solid-state lithium secondary batteries with sulfide inorganic electrolytes, *Chem. Eur. J.* 24 (2018) 6007-6018.
- [23] F. Yuan, L. Yang, X. Zou, S. Dong, S. Chi, J. Xie, H. Xing, L. Bian, L. Bao, J. Wang, Flexible all-solid-state electrolytes with ordered fast Li-ion-conductive nano-pathways for rechargeable lithium batteries, *J. Power Sources* 444 (2019) 227305.
- [24] D. Fenton, Complexes of alkali metal ions with poly(ethylene oxide), *Polymer* 14 (1973) 589.
- [25] Z. Xie, Z. Wu, X. An, A. Yoshida, Z. Wang, X. Hao, A. Abudula, G. Guan, Bifunctional ionic liquid and conducting ceramic co-assisted solid polymer electrolyte membrane for quasi-solid-state lithium metal batteries, *J. Membr. Sci.* 586 (2019) 122-129.
- [26] L. Chen, Y. Li, S.-P. Li, L.-Z. Fan, C.-W. Nan, J.B. Goodenough, PEO/garnet composite electrolytes for solid-state lithium batteries: From “ceramic-in-polymer” to “polymer-in-ceramic”, *Nano Energy* 46 (2018) 176-184.
- [27] K. Pożyczka, M. Marzantowicz, J. Dygas, F. Krok, Ionic conductivity and lithium transference number of poly (ethylene oxide): LiTFSI system, *Electrochim. Acta* 227 (2017) 127-135.
- [28] M. Marzantowicz, J. Dygas, F. Krok, Z. Florjańczyk, E. Zygadło-Monikowska, G. Lapienis, Ionic conductivity of electrolytes based on star-branched poly (ethylene oxide) with high concentration of lithium salts, *Solid State Ionics* 192 (2011) 137-142.

- [29] P. Pongsuk, J. Pumchusak, Effects of halloysite nanotubes on ionic conductivity, morphology, crystallinity and mechanical properties of PEO-based solid polymer electrolyte, *Mater. Today: Proc.* 17 (2019) 1956-1963.
- [30] P. Pongsuk, J. Pumchusak, Effects of natural clay on ionic conductivity, crystallinity and thermal properties of PEO-LiCF₃SO₃-natural clay as solid polymer electrolyte nanocomposites, *Key Eng. Mater.* 803 (2019) 98-103.
- [31] J. Zhang, N. Zhao, M. Zhang, Y. Li, P.K. Chu, X. Guo, Z. Di, X. Wang, H. Li, Flexible and ion-conducting membrane electrolytes for solid-state lithium batteries: dispersion of garnet nanoparticles in insulating polyethylene oxide, *Nano Energy* 28 (2016) 447-454.
- [32] C.V.S. Reddy, X. Han, Q.-Y. Zhu, L.-Q. Mai, W. Chen, Conductivity and discharge characteristics of (PVC+NaClO₄) polymer electrolyte systems, *Eur. Polym. J.* 42 (2006) 3114-3120.
- [33] S. Ramesh, A. Arof, Electrical conductivity studies of polyvinyl chloride-based electrolytes with double salt system, *Solid State Ionics* 136 (2000) 1197-1200.
- [34] M. Khalifa, S. Janakiraman, S. Ghosh, A. Venimadhav, S. Anandhan, PVDF/halloysite nanocomposite-based non-wovens as gel polymer electrolyte for high safety lithium ion battery, *Polym. Compos.* 40 (2019) 2320-2334.
- [35] Z. Xie, Z. Wu, X. An, X. Yue, P. Xiaokaiti, A. Yoshida, A. Abudula, G. Guan, A sandwich-type composite polymer electrolyte for all-solid-state lithium metal batteries with high areal capacity and cycling stability, *J. Membr. Sci.* 596 (2020) 117739.

- [36] D. Zhou, Y.B. He, R. Liu, M. Liu, H. Du, B. Li, Q. Cai, Q.H. Yang, F. Kang, In situ synthesis of a hierarchical all-solid-state electrolyte based on nitrile materials for high-performance lithium-ion batteries, *Adv. Energy Mater.* 5 (2015) 1500353.
- [37] Y. Liang, S. Deng, Y. Xia, X. Wang, X. Xia, J. Wu, C. Gu, J. Tu, A superior composite gel polymer electrolyte of $\text{Li}_7\text{La}_3\text{Zr}_2\text{O}_{12}$ -poly (vinylidene fluoride-hexafluoropropylene)(PVDF-HFP) for rechargeable solid-state lithium ion batteries, *Mater. Res. Bull.* 102 (2018) 412-417.
- [38] P. M. Shanthi, P. J. Hanumantha, T. Albuquerque, B. Gattu, P.N. Kumta, Novel composite polymer electrolytes of PVDF-HFP derived by electrospinning with enhanced Li-ion conductivities for rechargeable lithium-sulfur batteries, *ACS Appl. Energy Mater.* 1 (2018) 483-494.
- [39] G. Chen, F. Zhang, Z. Zhou, J. Li, Y. Tang, A flexible dual-ion battery based on PVDF-HFP-modified gel polymer electrolyte with excellent cycling performance and superior rate capability, *Adv. Energy Mater.* 8 (2018) 1801219.
- [40] X. Hao, H. Wenren, X. Wang, X. Xia, J. Tu, A gel polymer electrolyte based on PVDF-HFP modified double polymer matrices via ultraviolet polymerization for lithium-sulfur batteries, *J. Colloid Interface Sci.* 558 (2019) 145-154.
- [41] Y. Yusof, M. Shukur, M. Hamsan, K. Jumbri, M. Kadir, Plasticized solid polymer electrolyte based on natural polymer blend incorporated with lithium perchlorate for electrical double-layer capacitor fabrication, *Ionics* 25 (2019) 5473-5484.
- [42] P.S. Kumar, A. Sakunthala, M. Reddy, M. Prabu, Structural, morphological, electrical and electrochemical study on plasticized PVdF-HFP/PEMA blended polymer electrolyte for lithium polymer battery application, *Solid State Ionics* 319 (2018) 256-265.

- [43] L. Meabe, T.V. Huynh, D. Mantione, L. Porcarelli, C. Li, L.A. O'Dell, H. Sardon, M. Armand, M. Forsyth, D. Mecerreyes, UV-cross-linked poly (ethylene oxide carbonate) as free standing solid polymer electrolyte for lithium batteries, *Electrochim. Acta* 302 (2019) 414-421.
- [44] M. Falco, C. Simari, C. Ferrara, J.R. Nair, G. Meligrana, F. Bella, I. Nicotera, P. Mustarelli, M. Winter, C. Gerbaldi, Understanding the effect of UV-induced crosslinking on the physico-chemical properties of highly performing PEO/LiTFSI-based polymer electrolytes, *Langmuir* 35 (2019) 8210-8219.
- [45] Q. Xia, J. Wu, Q.X. Shi, X. Xiang, X. Li, H. Pei, H. Zeng, X. Xie, Y.S. Ye, UV-curable boron nitride nanosheet/ionic liquid-based crosslinked composite polymer electrolyte in lithium metal batteries, *J. Power Sources* 414 (2019) 283-292.
- [46] F. Croce, L. Persi, F. Ronci, B. Scrosati, Nanocomposite polymer electrolytes and their impact on the lithium battery technology, *Solid State Ionics* 135 (2000) 47-52.
- [47] C. Capiglia, P. Mustarelli, E. Quartarone, C. Tomasi, A. Magistris, Effects of nanoscale SiO₂ on the thermal and transport properties of solvent-free, poly (ethylene oxide)(PEO)-based polymer electrolytes, *Solid State Ionics* 118 (1999) 73-79.
- [48] S. Klongkan, J. Pumchusak, Effects of nano alumina and plasticizers on morphology, ionic conductivity, thermal and mechanical properties of PEO-LiCF₃SO₃ solid polymer electrolyte, *Electrochim. Acta* 161 (2015) 171-176.
- [49] L. Wang, X. Li, W. Yang, Enhancement of electrochemical properties of hot-pressed poly (ethylene oxide)-based nanocomposite polymer electrolyte films for all-solid-state lithium polymer batteries, *Electrochim. Acta* 55 (2010) 1895-1899.

- [50] W. Liu, N. Liu, J. Sun, P.-C. Hsu, Y. Li, H.-W. Lee, Y. Cui, Ionic conductivity enhancement of polymer electrolytes with ceramic nanowire fillers, *Nano Lett.* 15 (2015) 2740-2745.
- [51] W. Liu, D. Lin, J. Sun, G. Zhou, Y. Cui, Improved lithium ionic conductivity in composite polymer electrolytes with oxide-ion conducting nanowires, *ACS Nano* 10 (2016) 11407-11413.
- [52] X. Shi, M. Li, H. Yang, S. Chen, L. Yuan, K. Zhang, J. Sun, PEG-300 assisted hydrothermal synthesis of $4\text{ZnO} \cdot \text{B}_2\text{O}_3 \cdot \text{H}_2\text{O}$ nanorods, *Mater. Res. Bull.* 42 (2007) 1649-1656.
- [53] Z.-T. Yu, J.-J. Xu, Y.-S. Jiang, Z. Shi, Y. Guo, D.-J. Wang, J.-S. Chen, Photoluminescent and photovoltaic properties observed in a zinc borate $\text{Zn}_2(\text{OH})\text{BO}_3$, *J. Mater. Chem.* 13 (2003) 2227-2233.
- [54] P. Liang, Z. Tuoheti, Z.-H. Liu, Controlling the structure and morphology of zinc borate by adjusting the reaction temperature and pH value: formation mechanisms and luminescent properties, *RSC Adv.* 7 (2017) 3695-3703.
- [55] W. Liu, S.W. Lee, D. Lin, F. Shi, S. Wang, A.D. Sendek, Y. Cui, Enhancing ionic conductivity in composite polymer electrolytes with well-aligned ceramic nanowires, *Nat. Energy* 2 (2017) 17035.
- [56] F. Deng, X. Wang, D. He, J. Hu, C. Gong, Y.S. Ye, X. Xie, Z. Xue, Microporous polymer electrolyte based on PVDF/PEO star polymer blends for lithium ion batteries, *J. Membr. Sci.* 491 (2015) 82-89.
- [57] A.R. Polu, H.-W. Rhee, Ionic liquid doped PEO-based solid polymer electrolytes for lithium-ion polymer batteries, *Int. J. Hydrogen Energy* 42 (2017) 7212-7219.

- [58] P. Zhu, C. Yan, M. Dirican, J. Zhu, J. Zang, R.K. Selvan, C.-C. Chung, H. Jia, Y. Li, Y. Kiyak, $\text{Li}_{0.33}\text{La}_{0.557}\text{TiO}_3$ ceramic nanofiber-enhanced polyethylene oxide-based composite polymer electrolytes for all-solid-state lithium batteries, *J. Mater. Chem. A* 6 (2018) 4279-4285.
- [59] A. Nagajothi, R. Kannan, S. Rajashabala, Preparation and characterization of PEO-based composite gel-polymer electrolytes complexed with lithium trifluoro methane sulfonate, *Mater. Sci.-Pol.* 36 (2018) 185-192.
- [60] N. Zhang, J. He, W. Han, Y. Wang, Composite solid electrolyte PEO/SN/ LiAlO_2 for a solid-state lithium battery, *J. Mater. Sci.* 54 (2019) 9603-9612.
- [61] N.N. Sa'adun, R. Subramaniam, R. Kasi, Development and characterization of poly (1-vinylpyrrolidone-co-vinyl acetate) copolymer based polymer electrolytes, *Sci. World J.* 2014 (2014).

Chapter 6 Conclusions and Prospect

6.1 Conclusions

To date, various endeavors have been paid to promote the high ionic conductivity as well as the high cycle stability of the SEs. Although great progress has been achieved, the design and synthesis of SEs with higher ionic conductivity as well as higher stability especially at RT are still full of challenge. To realize high performance of SSLBs, the SEs with intrinsically high ion conductivity, high environmental and electrochemical stability and a wide electrochemical window are still required. The main conclusions are summarized as follows.

Chapter 1: the situations of the SEs were critically reviewed, the main challenges for the development of SEs were given and the utmost limits of those state-of-the-art SEs were analyzed, and then the objectives of this research were stated.

Chapter 2: chemical regents, performance evaluation, and various characterization method were introduced in detail.

Chapter 3: the ionic conductivity of $70\text{Li}_2\text{S}\cdot 30\text{P}_2\text{S}_5$ solid electrolyte can be effectively improved by doping a small amount of SeS_2 by a facile mechanical milling followed with a heat treatment process. The $70\text{Li}_2\text{S}\cdot 29\text{P}_2\text{S}_5\cdot 1\text{SeS}_2$ solid electrolyte exhibits a highest conductivity of $5.28\times 10^{-3}\text{ S}\cdot\text{cm}^{-1}$ at $20\text{ }^\circ\text{C}$ with a lowest activation energy of $24.70\text{ kJ}\cdot\text{mol}^{-1}$ and excellent electrochemical stability among all prepared electrolytes. The crystalline

structures of SeS_2 doping LPS solid electrolyte by XRD analysis-refinement assisting with the first principles calculations based on the DFT. Furthermore, the ASSLSBs assembled based on $70\text{Li}_2\text{S}\cdot 29\text{P}_2\text{S}_5\cdot 1\text{SeS}_2$ electrolyte and sulfur-reduced graphene oxide (S-rGO) composite cathode shows an initial discharge capacity of $658.1 \text{ mAh}\cdot\text{g}^{-1}$ at $0.1 \text{ mA}\cdot\text{cm}^{-2}$, and an excellent cycling stability with a maintained reversible discharge capacity at $558.3 \text{ mAh}\cdot\text{g}^{-1}$ after 100 cycles with a coulombic efficiency of almost 100%, attaining 84.8% of capacity retention compared to the 1st discharge capacity. And analytical results of EIS and the interface observe by SEM reveal that addition of SeS_2 into the $\text{Li}_2\text{S}\text{-P}_2\text{S}_5$ electrolyte substrate can decrease the interfacial resistance between the electrode and solid electrolyte and reduce the production of lithium dendrites. It is expected that $70\text{Li}_2\text{S}\cdot 29\text{P}_2\text{S}_5\cdot 1\text{SeS}_2$ electrolyte can be served as an effective solid electrolyte for the construction of high performance all-solid-state batteries.

Chapter 4: VSB-5 nanorods with a thin and uniform size were successfully prepared by the hydrothermal synthesis method and used as the filler in the PEO-LiTFSI SPE for SSBs. The addition of VSB-5 in PEO-LiTFSI SPE effectively improved the thermal stability, lithium stability, ionic conductivity, interfacial stability, and operation electrochemical window. As a result, the ionic conductivity of PEO-LiTFSI-3% VSB-5 reached 4.83×10^{-5} at $30\text{ }^\circ\text{C}$ with a widened electrochemical stability window up to 4.13 V vs. Li/Li^+ . It is found that the high ionic conductivity of PEO-LiTFSI-3% VSB-5 was resulted from not only the interaction between the VSB-5 nanorod and $-\text{SO}_2-$ in the TFSI $^-$, which could promote the transport ability of Li^+ , but also the interaction between the VSB-5 nanorod and the PEO, which significantly reduced the glass transition temperature and degree of crystallinity of PEO-LiTFSI-3% VSB-5 SPE so that the ionic conductivity was also

enhanced. Furthermore, the $\text{LiFePO}_4/\text{PEO-LiTFSI-3\%VSB-5/Li}$ battery exhibited the improved cyclic performance as well as the rate capability compared with the $\text{LiFePO}_4/\text{PEO-LiTFSI/Li}$ battery due to the suppression effect of lithium dendrites and high ionic conductivity of PEO-LiTFSI-3% VSB-5 SPE. It is demonstrated that this new solid polymer composite electrolyte should be a promising electrolyte applied in the solid-state batteries with lithium metal electrode.

Chapter 5: the rod-like $\text{Zn}_2(\text{OH})\text{BO}_3$ particles prepared by the hydrothermal method was successfully applied as a filler to improve PEO-LiTFSI SPE performance. A high conductivity of 2.78×10^{-5} at 30 °C was achieved for the PEO-LiTFSI-10% $\text{Zn}_2(\text{OH})\text{BO}_3$ SPE, which can be attributed to the reducing of PEO crystallinity and increasing Li migrating pathway on the interface between $\text{Zn}_2(\text{OH})\text{BO}_3$ and PEO. Moreover, the optimum SPE exhibited a wide electrochemical window exceeding 4.51 V and a high thermal stability. More importantly, such a SPE effectively suppressed the Li dendrite growth. The fabricated $\text{LiFePO}_4/\text{PEO-LiTFSI-10\%Zn}_2(\text{OH})\text{BO}_3/\text{Li}$ SSLB showed excellent cycling stability with a specific discharge capacity of above $147 \text{ mAh} \cdot \text{g}^{-1}$ and a coulombic efficiency higher than 99.7% after 50 cycles, which is noticeably higher than these of the $\text{LiFePO}_4/\text{PEO-LiTFSI/Li}$ SSLB cell. These outstanding performances indicated that the PEO-LiTFSI- $\text{Zn}_2(\text{OH})\text{BO}_3$ SPE could be served as an attractive solid electrolyte for next generation of safe and high electrochemical performance lithium batteries.

6.2 Prospect

For the SEs, its ionic conductivity should be close to or over that of liquid electrolyte.

That is, the utmost limit of the solid electrolyte should be in the order of $10^{-2} \text{ S} \cdot \text{cm}^{-1}$. The ionic conductivities of some of the developed sulfide electrolytes have reached high-level. However, the sulfide electrolyte always has bad environmental stability when exposed to air rigorous, complicated preparation condition, low charge-discharge stability, and unfavorable interface contacts with electrodes, making them difficult to be applied practically despite of the high ionic conductivity. In order to solve these problems, it is possible to develop novel solid sulfide electrolyte system with high ionic conductivity and high stability to air by introducing appropriate additives. Meanwhile, the interface interactions between the electrode and solid sulfide electrolyte needs to be optimized. Various methods including the enlargement of contact area, finding more matching electrode materials, and electrode surface modification, have been utilized to obtain an intimate contact to lower the resistance. Such kinds of researches and developments will be continued in the future development of solid sulfide electrolytes.

Moreover, the ionic conductivity of the SPE at the low operation temperature has large restrictions. However, comparing to other SEs, the SPEs have high flexibility, and long stability as the inorganic SEs. Among the PEO and PEO like, non-polyether, and single lithium-ion conducting SPEs, PEO is the most widely used polymer host in SPEs. Especially, it is found that Li^+ ionic conductivity and stability can be promoted by doping suitable materials to reduce the crystallinity of PEO, which should be a main way to improve the ionic conductivity of PEO-based SPEs in the future study. Recently, single lithium-ion conducting solid polymer electrolytes (SLIC-SPEs) including poly(ionic liquid)s (PILs) have widely been developed to overcome the challenges and drawbacks of conventional dual-ion conducting SPEs. However, low ionic conductivity at medium temperature and the inferior interfacial properties of SPEs are still challenge for their

application in SSLBs.

Meanwhile, it is still a great challenge to increase the ionic conductivity of the solid oxide electrolyte. The main way to improve the ionic conductivity is to form Li^+ channels as much as possible in the electrolyte [1, 2], or to broaden the Li^+ ion transport channels in a suitable size [3, 4], or weaken the binding between Li^+ and anions in the crystal structures [5, 6], and so on. As reviewed above, the solid oxide electrolytes include six types: NASICON, perovskite, garnet, amorphous/glass, $\gamma\text{-Li}_3\text{PO}_4$ and other types. These oxide electrolytes are highly stable in air, the safety of the SSLBs could be only realized by using the air-stable solid oxide electrolytes. In the future study, much work should focus on how to solve the following issues: low ionic conductivity at low temperatures, high grain-boundary resistance, and harsh preparation conditions. The main challenges and strategies can be summarized as follows: 1) designing solid oxide electrolytes with special structures to improve the ionic conductivity; 2) simplifying the preparation process to avoid high temperature treatment process for the practical application; 3) finding cheap materials to replace those expensive ones; 4) designing special structure to reduce the interface resistance for the hard texture of oxide electrolyte.

In comparison, although the novel hybrid electrolyte has a lower ionic conductivity than the sulfide electrolyte, it could be reaching the practical application by improving the fabrication method. Especially, by combining the organic electrolyte with the inorganic materials, it is possible to greatly improve the physical stability related to Li dendrite generation, the interface chemical stability, and mechanical property for the processing. Thusly, they have been received more and more attentions recently. In the future study, the main challenges are to increase the low ionic conductivity at RT, avoid the Li dendrite growth and improve the high voltage cathode compatibility in the practical applications.

To commercialize the SPEs and novel hybrid electrolytes, it is necessary to focus on the following research points: 1) developing a simpler and faster preparation method; 2) looking for new polymer electrolytes with special structure and optimizing lithium ion diffusion paths; 3) enhancing ionic conductivity at RT by finding the suitable lithium salt and other additives (including other new types of electrolytes); 4) improving interface stability and reducing interface resistance by modifying the electrolyte/electrode interface or adding interface transition layer to create excellent compatibility on the electrolyte/electrode interface; 5) inhibiting lithium dendrites growth by improving the anode interface or structure and designing emerging methods for combining electrolyte and anode (e.g., develop various material deposition and coating technologies). In a word, it is necessary to find suitable electrolytes with high ionic conductivity and excellent compatibility with electrodes.

All in all, the replacement of liquid electrolytes with SEs is necessary in the future because they not only offer a wide electrochemical stability window, but also make the batteries safer and more durable with a higher energy density and simple battery design. In particular, it is required to develop novel SEs, especially the solid oxide electrolytes, which have similar or higher ionic conductivity as the liquid ones. That is to say, it is necessary to break through the utmost limits of the present various SEs in SSLBs. These utmost limits have prompted researchers to make greater efforts to develop new SEs including improved ionic conductivity, physical, environmental and electrochemical stability, and meanwhile to optimize the electrolyte/electrode interface. Moreover, in order to satisfy practical applications, researchers also need to conduct more researches in optimizing the environmental stability, finding the electrode with high capacity and the solid electrolyte with good compatibility as well as high ionic conductivity. Only in this

way, the obtained SEs can be really applied in our daily life.

References

- [1] N. Kamaya, K. Homma, Y. Yamakawa, M. Hirayama, R. Kanno, M. Yonemura, T. Kamiyama, Y. Kato, S. Hama, K. Kawamoto, A lithium superionic conductor, *Nat. Mater.* 10 (2011) 682-686.
- [2] S. Hori, K. Suzuki, M. Hirayama, Y. Kato, R. Kanno, Lithium superionic conductor $\text{Li}_{9.42}\text{Si}_{1.02}\text{P}_{2.1}\text{S}_{9.96}\text{O}_{2.04}$ with $\text{Li}_{10}\text{GeP}_2\text{S}_{12}$ -Type structure in the Li_2S - P_2S_5 - SiO_2 pseudoternary system: synthesis, electrochemical properties, and structure-composition relationships, *Frontiers in Energy Research* 4 (2016) 38.
- [3] Y. Kato, S. Hori, T. Saito, K. Suzuki, M. Hirayama, A. Mitsui, M. Yonemura, H. Iba, R. Kanno, High-power all-solid-state batteries using sulfide superionic conductors, *Nature Energy* 1 (2016) 1-7.
- [4] J. Kim, Y. Yoon, M. Eom, D. Shin, Characterization of amorphous and crystalline Li_2S - P_2S_5 - P_2Se_5 solid electrolytes for all-solid-state lithium ion batteries, *Solid State Ionics* 225 (2012) 626-630.
- [5] R.P. Rao, M. Seshasayee, Molecular dynamics simulation of ternary glasses Li_2S - P_2S_5 - LiI , *J. Non-Cryst. Solids* 352 (2006) 3310-3314.
- [6] K. Yang, J. Dong, L. Zhang, Y. Li, L. Wang, Dual doping: an effective method to enhance the electrochemical properties of $\text{Li}_{10}\text{GeP}_2\text{S}_{12}$ -based solid electrolytes, *J. Am. Ceram. Soc.* 98 (2015) 3831-3835.

List of publications and presentations

Publications

1. **Z. Wu**, Z. Xie, A. Yoshida, Z. Wang, X. Hao, A. Abudula, G. Guan, Utmost limits of various solid electrolytes in all-solid-state lithium batteries: A critical review, *Renewable Sustainable Energy Rev.* 109 (2019) 367-385.
2. **Z. Wu**, Z. Xie, A. Yoshida, X. An, Z. Wang, X. Hao, A. Abudula, G. Guan, Novel SeS₂ doped Li₂S-P₂S₅ solid electrolyte with high ionic conductivity for all-solid-state lithium sulfur batteries, *Chem. Eng. J.* 380 (2020) 122419.
3. **Z. Wu**, Z. Xie, A. Yoshida, J. Wang, T. Yu, Z. Wang, X. Hao, A. Abudula, G. Guan, Nickel phosphate nanorod-enhanced polyethylene oxide-based composite polymer electrolytes for solid-state lithium batteries, *J. Colloid Interface Sci.* 565 (2020) 110-118.
4. **Z. Wu**, Z. Xie, J. Wang, T. Yu, X. Du, Z. Wang, X. Hao, A. Abudula, G. Guan, Simultaneously Enhancing the Thermal Stability and Electrochemical Performance of Solid Polymer Electrolytes by Incorporating Rod-like Zn₂(OH)BO₃ Particles, *Int. J. Hydrogen Energy* 45 (2020) 19601-19610.
5. **Z. Wu**, Z. Xie, J. Wang, T. Yu, Z. Wang, X. Hao, A. Abudula, G. Guan, Lithium-Salt-Containing Ionic Liquid-Incorporated Li-Al-Layered Double Hydroxide-Based Solid Electrolyte with High-Performance and Safety in Solid-State Lithium Batteries, *ACS Sustainable Chem. Eng.* 8 (2020) 12378-12387.
6. Z. Xie, **Z. Wu**, X. An, A. Yoshida, Z. Wang, X. Hao, A. Abudula, G. Guan, Bifunctional ionic liquid and conducting ceramic co-assisted solid polymer electrolyte

- membrane for quasi-solid-state lithium metal batteries, J. Membr. Sci. 586 (2019) 122-129.
7. Z. Xie, **Z. Wu**, X. An, X. Yue, P. Xiaokaiti, A. Yoshida, A. Abudula, G. Guan, A sandwich-type composite polymer electrolyte for all-solid-state lithium metal batteries with high areal capacity and cycling stability, J. Membr. Sci. 596 (2020) 117739.
8. Z. Xie, **Z. Wu**, X. An, X. Yue, A. Yoshida, X. Du, X. Hao, A. Abudula, G. Guan, 2-Fluoropyridine: a novel electrolyte additive for lithium metal batteries with high areal capacity as well as high cycling stability, Chem. Eng. J. 393 (2020) 124789.
9. Z. Xie, **Z. Wu**, X. An, X. Yue, J. Wang, A. Abudula, G. Guan, Anode-Free Rechargeable Lithium Metal Batteries: Progress and Prospects, Energy Storage Mater. 2020.

International presentations

1. ZHENGKUN XIE, **Zhijun Wu**, Xiyan Yue, Akihiro Yoshida, Abuliti Abudula, Guoqing Guan, Effect of electrolyte additive on the performance of Lithium metal batteries, 18th Asian Pacific Confederation of Chemical Engineering Congress (APCChE 2019), Sapporo, Hokkaido, Japan, September 23-27, 2019.
2. Zhengkun Xie, **Zhijun Wu**, Xiyan Yue, Akihiro Yoshida, Tao Yu, Katsuki Kusakabe, Abuliti Abudula, Guoqing Guan, Functional ionic liquid assisted commercial separator for advanced lithium metal batteries, The 32nd International Symposium on Chemical Engineering (ISChE2019), Chungnam National University, Daejeon, Korea, December 6-8, 2019.

Domestic presentations

1. **Zhijun Wu**, Zhengkun Xie, Akihiro Yoshida, Abuliti Abudula, Guoqing Guan, SeS_2 doped $\text{Li}_2\text{S-P}_2\text{S}_5$ glass-ceramic electrolyte with high ionic conductivity for all-solid-state lithium sulfur batteries, Joint Meeting of the Tohoku Area Chemistry Societies of 2018, Akita University, Sept 15-16, 2018.
2. **Zhijun Wu**, Zhengkun Xie, Akihiro Yoshida, Abuliti Abudula, Guoqing Guan, A novel solid electrolyte of $\text{Li}_{7+x}\text{P}_{3-x}\text{Mo}_x\text{S}_{11-2x}\text{Se}_{2x}$ for all-solid-state lithium-sulfur batteries, The Society of Chemical Engineers, Japan (SCEJ) 84th Annual Meeting, Shibaura Institute of Technology, Mar 13-15, 2019.
3. **Zhijun Wu**, Zhengkun Xie, Xiyan Yue, Jiajia Wang, Kitiphatpiboon Nutthaphak, Tao Yu, Akihiro Yoshida, Abuliti Abudula, Guoqing Guan, Simultaneously enhancing the thermal stability and electrochemical performance of solid polymer electrolytes by incorporating rod-like $\text{Zn}_2(\text{OH})\text{BO}_3$ particles, The Electrochemical Society of Japan, ECSJ Fall Meeting, University of Yamanashi, Sept 5-6, 2019.
4. ZHENGKUN XIE, **Zhijun Wu**, Tao Yu, Akihiro Yoshida, Abuliti Abudula, Guoqing Guan, Ionic liquid incorporated solid polymer electrolyte for all-solid-state lithium rechargeable batteries, Joint Meeting of the Tohoku Area Chemistry Societies of 2018, Akita University, September 15-16, 2018.
5. ZHENGKUN XIE, **Zhijun Wu**, Akihiro Yoshida, Abuliti Abudula, Guoqing Guan, Sandwiched polymer-ceramics electrolyte for high voltage all-solid-state lithium rechargeable batteries, The Society of Chemical Engineers, Japan (SCEJ) 84th Annual Meeting, Shibaura Institute of Technology, March 13-15, 2019.

6. ZHENGKUN XIE, **Zhijun Wu**, Xiyan Yue, Tao Yu, Akihiro Yoshida, Abuliti Abudula, Guoqing Guan, Enabling reliable lithium metal batteries by an organic electrolyte additive, The Electrochemical Society of Japan, ECSJ Fall Meeting, University of Yamanashi, September 5-6, 2019.

List of patents

1. **武志俊**、謝正坤、吉田曉弘、官国清、阿布里提、関和治、“ $\text{Li}_2\text{S}-\text{P}_2\text{S}_5-\text{SeS}_2$ 系ガラスセラミックからなる全固体リチウム硫黄電池用固体電解質、前記固体電解質に適した正極材料及びこれらの製造方法、並びにこれらを含む全固体リチウム硫黄電池”、出願番号：特願 2018-157667、出願日：2018 年 8 月 24 日.
2. **武志俊**、謝正坤、吉田曉弘、官国清、阿布里提、関和治、“全固体二次電池用電解質”、出願番号：特願 2019-029489、出願日：2019 年 2 月 21 日.
3. **武志俊**、官国清、謝正坤、吉田曉弘、関和治、阿布里提、“電解質用添加剤、固体電解質及びリチウムイオン二次電池”、出願番号：特願 2019-150307、出願日：2019 年 8 月 20 日.
4. **武志俊**、官国清、謝正坤、関和治、阿布里提、“リチウムイオン電池用固体電解質及びその製造方法、リチウムイオン電池”、出願番号：特願 2020-080743、出願日：2020 年 4 月 30 日.
5. 謝正坤、**武志俊**、吉田曉弘、官国清、阿布里提、関和治、“リチウムイオン伝導性ポリマー電解質”、出願番号：特願 2018-159952、出願日：2018 年 8 月 29 日.

6. 謝正坤、**武志俊**、吉田曉弘、官国清、阿布里提、関和治、“ポリマーセラミックス複合電解質膜”、出願番号：特願 2019-029487、出願日：2019 年 2 月 21 日.
7. 謝正坤、**武志俊**、吉田曉弘、官国清、阿布里提、関和治、“電池用電解質及びその製造方法並びに二次電池”、出願番号：特願 2019-030552、出願日：2019 年 2 月 22 日.
8. 謝正坤、**武志俊**、吉田曉弘、官国清、阿布里提、関和治、“電解質用添加剤及びその製造方法”、出願番号：特願 2019-030549、出願日：2019 年 2 月 22 日.
9. 謝正坤、**武志俊**、吉田曉弘、官国清、阿布里提、関和治、“電解質用添加剤、リチウムイオン二次電池用電解質及びリチウムイオン二次電池”、出願番号：特願 2019-105399、出願日：2019 年 6 月 5 日.
10. 謝正坤、**武志俊**、吉田曉弘、官国清、阿布里提、関和治、“電解質用添加剤、リチウム二次電池用電解質及びリチウム二次電池”、出願番号：特願 2019-110272、出願日：2019 年 6 月 13 日.
11. 謝正坤、官国清、**武志俊**、吉田曉弘、関和治、阿布里提、“電解質用添加剤、リチウム二次電池用電解質及びリチウム二次電池”、出願番号：特願 2019-155559、出願日：2019 年 8 月 28 日.
12. 謝正坤、官国清、**武志俊**、吉田曉弘、関和治、阿布里提、“セパレータ用浸漬及び / 又は塗布剤、リチウム二次電池用セパレータ及びリチウム二次電池”、出願番号：特願 2019-155561、出願日：2019 年 8 月 28 日.
13. 謝正坤、官国清、岳喜岩、**武志俊**、吉田曉弘、阿布里提、関和治、“生物材料由来のハードカーボン、負極材料、負極、及びアルカリイオン電池”、出願番号：特願 2019-192989、出願日：2019 年 10 月 23 日.

14. 謝正坤、官国清、**武志俊**、岳喜岩、関和治、阿布里提、“二次電池用正極活物質前駆体、二次電池用正極活物質、二次電池用陰極液、二次電池用正極及び二次電池”、出願番号：特願 2020-019666、出願日：2020 年 2 月 7 日.
15. 謝正坤、官国清、**武志俊**、岳喜岩、関和治、阿布里提、“電池用電解液及びリチウム電池”、出願番号：特願 2020-102684、出願日：2020 年 6 月 12 日.

Award

1. **Excellent Student Recognition**, Hirosaki University, Japan, March, 2020.